Cambridge Books Online

Ideal MHD

Jeffrey P. Freidberg

Chapter

11 - Stability: one-dimensional configurations pp. 428-569

11

Stability: one-dimensional configurations

11.1 Introduction

Chapter 11 describes the MHD stability of one-dimensional cylindrical configurations, specifically the general screw pinch. The analysis involves both the Energy Principle and in some cases the normal mode eigenvalue equation. The goal is to learn about the properties of a magnetic geometry that lead to favorable or unfavorable MHD stability. Even in a cylindrical geometry a great deal of insight can be obtained regarding MHD stability, although there are important toroidal effects that are described in the next chapter.

The discussion begins with the special case of the θ-pinch. Here, a trivial application of the Energy Principle shows that the θ-pinch has inherently favorable stability properties. Also described is "continuum damping" which has many similarities to the well-known phenomenon of Landau damping of electrostatic plasma oscillations. This analysis is simplified by the introduction of the "incompressible MHD" approximation. It is shown that even though the continuum lies entirely on the real ω axis, an initial perturbation will be exponentially damped.

The next application is to the Z-pinch. This configuration is shown to have unfavorable stability properties. It is potentially unstable to both the $m = 0$ and $m = 1$ modes. However, MHD stability can be achieved with the addition of a solid, current-carrying wire along the axis of the plasma. The resulting configuration is known as a hard-core pinch and is the basis for the levitated dipole concept. Both the Energy Principle and the normal mode equations are used in the analysis. Also, for comparison the $m = 0$ stability criterion is derived for the double adiabatic model. It is shown that in the region of experimental interest the stability boundaries are quite close to those predicted by ideal MHD.

The analysis continues with the stability of the general screw pinch. The discussion begins with a general simplification of the Energy Principle that takes advantage of the cylindrical symmetry of the equilibrium. Although the screw pinch is a

428

relatively basic configuration one finds that the resulting simplified form of δW still exhibits a rather high level of complexity. The condition to minimize δW requires that the radial component of the plasma displacement ξ_r satisfy a second-order ordinary differential equation and this equation is derived in the text. To complete the formulation of the stability problem boundary conditions are presented corresponding to (1) a perfectly conducting wall on the plasma, (2) a plasma isolated from a perfectly conducting wall by a vacuum region, and (3) a plasma isolated from a resistive wall by a vacuum region. For comparison, the general normal mode eigenvalue equation is derived which is shown to be a quite complicated second-order ordinary differential equation.

Three important stability results are derived from the general form of δW for the screw pinch: (1) Suydam's criterion which is a local test for interchange stability; (2) Newcomb's procedure which is a practical general method for testing stability; and (3) the oscillation theorem which shows that in spite of the complexity of the full normal mode equation, the eigenvalues exhibit Sturmian behavior with respect to the number of nodes in the eigenfunction.

Based on the general stability theory of the screw pinch, two applications are discussed: the "straight tokamak" and the reversed field pinch (RFP). The stability of the straight tokamak is analyzed by substituting the large aspect ratio expansion into δW. There is a huge simplification in the minimizing differential equation. Nevertheless, this highly simplified form sheds considerable light on the basic MHD instability drives that give rise to sawtooth oscillations, current- and density-driven disruptions, and edge localized modes (ELMs). These experimentally observed, and often operationally limiting, phenomena are described and then analyzed by means of the simplified form of δW. Toroidal effects also play an important role in some of the phenomena and are discussed in the next chapter. Still, it is useful in terms of intuition to make an initial attempt at understanding the phenomena using the simplified cylindrical model.

The last topic of interest is the stability of the RFP. The ordering of the fields in an RFP is such that the complete form of δW is required. However, somewhat off-setting this complexity is the fact that toroidal effects are in general small, implying that the one-dimensional cylindrical results provide a relatively complete picture of RFP stability. The analysis shows that RFPs can be stable to high values of β against all internal modes but are potentially very instable to external modes. Thus a conducting wall and feedback are required for stability. The goals of the analysis are to (1) determine which n values are unstable with the wall at infinity and (2) to calculate how close the wall must be to stabilize all external modes. Experimental results are discussed showing how a sophisticated feedback system can dramatically improve MHD stability. In practice once the ideal modes are under control, the RFP is dominated by resistive MHD turbulence. This turbulence

reduces β substantially below the wall stabilized ideal limits. However, the resulting βs are still high enough for energy applications. The important question of resistive MHD turbulence is beyond the scope of the present volume.

As a closing comment it is worth noting that the cylindrical screw pinch in general provides a reasonably accurate description of current driven instabilities in a low β plasma. In tokamaks and stellarators (but not RFPs), an accurate description of pressure-driven instabilities requires the inclusion of toroidal effects.

11.2 The basic stability equations

The analysis in this section is based on several formulations of the stability equations, namely the Energy Principle and the normal mode eigenvalue equations. Also, a simplified form of the normal mode equations, known as "incompressible MHD," is used to discuss certain phenomena. For convenience these models are summarized below.

11.2.1 The Energy Principle

Several forms of the Energy Principle have been discussed in Chapter 8. The analysis in Chapter 11 is based on the intuitive form given by

$$\delta W(\boldsymbol{\xi}^*, \boldsymbol{\xi}) = \delta W_F + \delta W_S + \delta W_V$$

$$\delta W_F(\boldsymbol{\xi}^*, \boldsymbol{\xi}) = \frac{1}{2\mu_0} \int_P \left\{ |\mathbf{Q}_\perp|^2 + B^2 |\nabla \cdot \boldsymbol{\xi}_\perp + 2\boldsymbol{\xi}_\perp \cdot \boldsymbol{\kappa}|^2 + \mu_0 \gamma p |\nabla \cdot \boldsymbol{\xi}|^2 \right.$$

$$\left. - 2\mu_0 (\boldsymbol{\xi}_\perp \cdot \nabla p)(\boldsymbol{\xi}_\perp^* \cdot \boldsymbol{\kappa}) - \mu_0 J_{||} \boldsymbol{\xi}_\perp^* \times \mathbf{b} \cdot \mathbf{Q}_\perp \right\} d\mathbf{r}$$

$$\delta W_S(\boldsymbol{\xi}_\perp^*, \boldsymbol{\xi}_\perp) = \frac{1}{2\mu_0} \int_{S_p} |\mathbf{n} \cdot \boldsymbol{\xi}_\perp|^2 \, \mathbf{n} \cdot \left[\!\left[\nabla \left(\frac{B^2}{2} + \mu_0 p \right) \right]\!\right] dS$$

$$\delta W_V(\boldsymbol{\xi}_\perp^*, \boldsymbol{\xi}_\perp) = \frac{1}{2\mu_0} \int_V |\hat{\mathbf{B}}_1|^2 \, d\mathbf{r} \tag{11.1}$$

11.2.2 The normal mode eigenvalue equations

The general normal mode eigenvalue equations have also been derived in Chapter 8 and can be written as

$$-\omega^2 \rho \boldsymbol{\xi} = \mathbf{F}(\boldsymbol{\xi})$$

$$\mathbf{F}(\boldsymbol{\xi}) = \frac{1}{\mu_0} (\nabla \times \mathbf{B}) \times \mathbf{Q} + \frac{1}{\mu_0} (\nabla \times \mathbf{Q}) \times \mathbf{B} + \nabla(\boldsymbol{\xi} \cdot \nabla p + \gamma p \nabla \cdot \boldsymbol{\xi}) \tag{11.2}$$

$$\mathbf{Q}(\boldsymbol{\xi}_\perp) = \nabla \times (\boldsymbol{\xi}_\perp \times \mathbf{B})$$

11.2.3 Incompressible MHD

The incompressible MHD model is a special limit of the general normal mode equations in which the adiabatic equation of state is replaced by the incompressibility condition $\nabla \cdot \boldsymbol{\xi} = 0$. This is a useful limit when the growth time of the MHD instability of interest is much longer than the adiabatic transit time across one wavelength: that is, $\mathrm{Im}(\omega) \ll k_\parallel V_S$. The sound speed is effectively infinite.

There are two ways to obtain this limit. First, if one starts with the full compressible MHD equations one can take the limit $\gamma \to \infty$ (where γ is the ratio of specific heats). In this limit in order for the perturbed pressure $p_1 = -\boldsymbol{\xi} \cdot \nabla p - \gamma p \nabla \cdot \boldsymbol{\xi}$ to remain finite, then $\nabla \cdot \boldsymbol{\xi} \to 0$. However, to take this limit the full compressible normal equations are first required which then defeats the purpose of obtaining a simpler set of equations from the outset.

The second and simpler way to obtain the incompressible MHD equations is to replace the equation for p_1 with the condition $\nabla \cdot \boldsymbol{\xi} = 0$. The system is not over determined since p_1 is now a new unknown in the problem, a consequence of the fact that the product $\gamma p \nabla \cdot \boldsymbol{\xi}$ is indeterminate in the incompressible limit. The basic problem now has four unknowns $\boldsymbol{\xi}$, p_1, although p_1 can be eliminated from the outset by taking the curl of the momentum equation. The equations for incompressible MHD thus reduce to

$$\nabla \times (\omega^2 \mu_0 \rho \boldsymbol{\xi} + \mathbf{B} \cdot \nabla \mathbf{Q} + \mathbf{Q} \cdot \nabla \mathbf{B}) = 0$$
$$\nabla \cdot \boldsymbol{\xi} = 0 \tag{11.3}$$

This completes the summary of the models used to investigate the MHD stability of cylindrical plasmas.

11.3 Stability of the θ-pinch

The first configuration of interest is the θ-pinch. Several points are discussed. First, a simple application of the Energy Principle shows that the θ-pinch is always MHD stable. Second, a more detailed minimization of δW sheds light and provides intuition about which form of perturbation is the least stable. This is important when one thinks ahead to toroidal configurations. Third, an analysis is presented of the phenomenon known as continuum damping. It is shown here, in analogy with Landau damping of kinetic theory, that MHD perturbations can be exponentially damped by the MHD continua even though the continua lie on the real ω axis. Such damping can occur in cylindrical and toroidal systems, but for mathematical simplicity it is investigated here for the case of a "slab" θ-pinch. Continuum damping is in general not very important for determining MHD stability limits but is nonetheless an interesting MHD phenomenon to understand, with applications to plasma heating and space plasma physics.
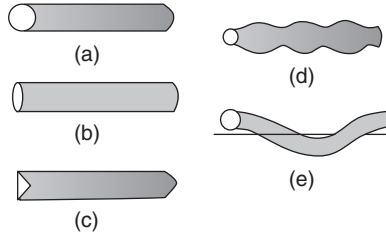
Figure 11.1 Graphical interpretation of the poloidal wave number m and toroidal wave number k : (a) unperturbed column; (b) $m = 2, k = 0$; (c) $m = 3, k = 0$; (d) $m = 0, k \neq 0$; (e) $m = 1, k \neq 0$.

11.3.1 Application of the Energy Principle to the θ-pinch

To begin recall that the basic equilibrium relation for a θ-pinch is given by

$$p + \frac{B^2}{2\mu_0} = \frac{B_0^2}{2\mu_0} \tag{11.4}$$

where $p = p(r)$, $\mathbf{B} = B(r)\mathbf{e}_z$, $\mathbf{J} = J_\theta(r)\mathbf{e}_\theta = -(B'/\mu_0)\mathbf{e}_\theta$, and B_0 is the externally applied magnetic field. Since the equilibrium is symmetric with respect to θ and z the plasma displacement can be Fourier analyzed as follows:

$$\boldsymbol{\xi}(\mathbf{r}) = \boldsymbol{\xi}(r) \exp(im\theta + ikz) \tag{11.5}$$

Here, m and k correspond to the "poloidal" and "toroidal" wave numbers respectively. They are interpreted graphically in Fig. 11.1. Observe that $m = 2$, $k = 0$ produces an elliptic deformation of the cross section. Similarly, $m = 3$, $k = 0$ produces a triangular deformation. In contrast, when $m = 0$, $k \neq 0$, the plasma cross section develops a series of bulges along the column. When both $m \neq 0$, $k \neq 0$ the cross section is helically deformed as illustrated for $m = 1$.

The general stability of a θ-pinch is easily established by the Energy Principle. To see this note that for a θ-pinch, $J_\parallel = 0$ and $\boldsymbol{\kappa} = \mathbf{e}_z \cdot \nabla \mathbf{e}_z = 0$. Then, from Eq. (11.1) one finds that δW_F reduces to

$$\delta W_F\left(\boldsymbol{\xi}^*, \boldsymbol{\xi}\right) = \frac{1}{2\mu_0} \int_P \left[\left|\mathbf{Q}_\perp\right|^2 + B^2\left|\nabla \cdot \boldsymbol{\xi}_\perp\right|^2 + \mu_0\gamma p\left|\nabla \cdot \boldsymbol{\xi}\right|^2 \right] d\mathbf{r} > 0 \tag{11.6}$$

Each term is positive implying that $\delta W_F > 0$. Furthermore, if the pressure profile vanishes smoothly at the edge of the plasma then $\delta W_S = 0$. Also, it is always true that $\delta W_V > 0$. These results can be combined, yielding

$$\delta W = \delta W_F + \delta W_V > 0 \tag{11.7}$$

Since $\delta W > 0$ for arbitrary perturbations, the conclusion is that a straight θ-pinch is MHD stable.

11.3.2 Minimizing δW_F for a θ-pinch

It is easy to understand why a θ-pinch is stable. Both driving sources of MHD instabilities, parallel current and unfavorable field line curvature, are zero for a θ-pinch. All that remains are the stabilizing terms associated with the three basic MHD waves. Additional insight can be gained by actually minimizing δW_F to show which form of perturbation is the least stable. This is the next task.

The first step in the minimization is to note that the general incompressibility condition $\nabla \cdot \boldsymbol{\xi} = 0$ leads to an expression for $\xi_\parallel = \xi_z$ that can be written as

$$\xi_z = \frac{i}{kr} \left[(r\xi)' + im\xi_\theta \right] \tag{11.8}$$

For simplicity of notation the radial component of the displacement has been defined as $\xi_r \equiv \xi$. Therefore, by choosing ξ_z to satisfy this relation (assuming that $k \neq 0$), it follows that the plasma compressibility term in δW_F vanishes.

The remaining terms in δW_F are evaluated by using the relations

$$\mathbf{Q}_\perp = ikB\boldsymbol{\xi}_\perp = ikB(\xi\mathbf{e}_r + \xi_\theta\mathbf{e}_\theta)$$
$$\nabla \cdot \boldsymbol{\xi}_\perp = \frac{1}{r}(r\xi)' + \frac{im}{r}\xi_\theta \tag{11.9}$$

Substituting in δW_F leads to

$$\frac{\delta W_F}{2\pi R_0} = \frac{\pi}{\mu_0} \int_0^a W(r)\, r\, dr$$
$$W = B^2 \left[k^2 \left(|\xi|^2 + |\xi_\theta|^2 \right) + \frac{1}{r^2} \left| (r\xi)' \right|^2 + \frac{m^2}{r^2} |\xi_\theta|^2 + \frac{im}{r} (r\xi^*)' \xi_\theta - \frac{im}{r} (r\xi)' \xi_\theta^* \right] \tag{11.10}$$

where a is the outer radius of the plasma and $2\pi R_0$ is the length of the equivalent torus. Observe that ξ_θ appears only algebraically in W. Consequently, the ξ_θ terms can be combined by completing the squares. A short calculation yields

$$W = B^2 \left\{ \left| k_0\xi_\theta - \frac{im}{k_0 r^2}(r\xi)' \right|^2 + \frac{k^2}{k_0^2 r^2} \left[\left| (r\xi)' \right|^2 + k_0^2 r^2 |\xi|^2 \right] \right\} \tag{11.11}$$

where $k_0^2(r) = k^2 + m^2/r^2$. Now, ξ_θ appears only in the first term, which is positive. Its minimum value is zero, which is obtained by choosing

$$\xi_\theta = \frac{im}{k^2 r^2 + m^2}(r\xi)' \tag{11.12}$$

The value of δW_F thus reduces to

$$\frac{\delta W_F}{2\pi R_0} = \frac{\pi}{\mu_0} \int_0^a \frac{k^2 B^2}{k_0^2 r^2} \left[\left| (r\xi)' \right|^2 + k_0^2 r^2 |\xi|^2 \right] r dr \qquad (11.13)$$

The main conclusion to be drawn from Eq. (11.13) is that the least stable modes in a θ-pinch occur for $k^2 \to 0$ in which case $\delta W_F \to 0$. In other words, a θ-pinch is always stable but approaches marginal stability for long wavelengths. This corresponds to minimizing the stabilizing effects of line bending. Now, when bending a θ-pinch into a large aspect ratio torus, small additional fields must be added to achieve toroidal force balance. The stability of the plasma against long-wavelength modes is then determined primarily by the properties of these small additional fields since the basic θ-pinch configuration is essentially marginally stable.

11.3.3 Continuum damping in a "slab" θ-pinch

The last θ-pinch application concerns continuum damping. As stated this is a phenomenon similar to Landau damping in the kinetic theory of electrostatic waves (Landau, 1946). The basic phenomenon can be described follows. The MHD model in general possesses two continua, one associated with the shear Alfven wave and the other with the sound wave. As their name implies, both exist for a continuous range of frequencies lying on the real axis. Even so, the fact that the frequencies are continuous rather than discrete leads to behavior in which an initial perturbation damps exponentially in time. Alternatively, if an electromagnetic wave with a real frequency is applied, as for heating, it damps exponentially with distance as it deposits energy in the plasma even though the wavelengths defined by the continua are purely real.

Below, a derivation is presented that shows how continuum damping arises when trying to heat a plasma by means of Alfven waves. The analysis assumes that an electromagnetic source is applied at the edge of a plasma with a frequency in the characteristic range of the shear Alfven wave. The resulting boundary value problem is solved allowing one to understand both mathematically and physically how the damping arises. Of specific interest is the calculation of the heating efficiency.

To simplify the mathematics a low β slab model of a θ-pinch is used assuming a density profile that varies linearly with distance. It is shown that under certain conditions an efficiency of 100% can be achieved! It is worth noting that in spite of this, high-efficiency, Alfven wave heating is rarely used in fusion plasmas, but this is associated primarily with practical antenna design problems rather than the physics.
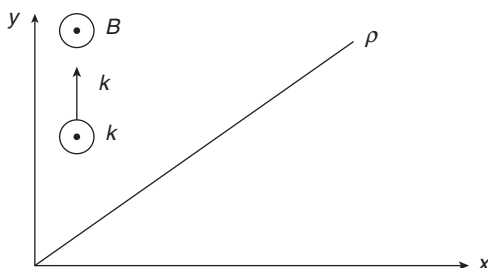
Figure 11.2   Geometry of the "slab" θ-pinch.

The model is deliberately kept as simple as possible to highlight the basic physics. Excellent and far more complete analysis of continuum damping, with applications to fusion and space plasmas, have been given by Tataronis and Grossmann (1973) and Goedbloed and Poedts (2004).

The approach taken here makes use of the incompressible equations of motion given by Eq. (11.3). The incompressibility assumption eliminates the sound wave continuum from the problem so that attention can be focused on the shear Alfven wave. A second-order ordinary differential equation is derived describing the dynamical behavior of the plasma. The assumption of a linearly varying density profile allows one to obtain an analytic solution to this equation from which the desired physical results can be easily extracted. The analysis proceeds as follows.

Derivation of the differential equation

The fields characterizing the equilibrium of a low β slab θ-pinch are given by $\mathbf{B} = B_0\mathbf{e}_z$, $p = 0$, and $\rho(x) = \rho_0'x$, where B_0, ρ_0' are constants. As stated the density is assumed to vary linearly with distance. The fact that ρ becomes very large at large x is unimportant since, as is shown shortly, deep in the plasma the electromagnetic fields decay exponentially deep in the plasma; that is, the results do not depend on the density profile and the linear density assumption makes the analysis simpler mathematically. The geometry of the problem is illustrated in Fig. 11.2.

The task now is to derive the governing differential equation describing the motion of the plasma, which is assumed to be driven by a source at $x = 0$ with a known frequency ω. Since the equilibrium depends only on x through the density, one can Fourier analyze the spatial dependence with respect to y and z,

$$\boldsymbol{\xi}(\mathbf{r}, t) = \boldsymbol{\xi}(x)\exp\left(-i\omega t + ik_\perp y + ik_{\parallel}z\right) \qquad (11.14)$$

where $\boldsymbol{\xi}(x) = \xi(x)\mathbf{e}_x + \xi_y(x)\mathbf{e}_y + \xi_z(x)\mathbf{e}_z$. In the analysis that follows it is assumed that $k_\perp$ and $k_{\parallel}$ are set by the structure of the launching source at $x = 0$; they are known quantities.

The analysis begins with the incompressibility condition $\nabla \cdot \boldsymbol{\xi} = 0$ which yields an algebraic relation between ξ_y and ξ_z that can be written as

$$ik_\perp \xi_y + ik_{||}\xi_z = -\xi' \tag{11.15}$$

A second algebraic relation between ξ_y and ξ_z is obtained from the $\mathbf{e}_x$ component of Eq. (11.3) after using the facts that $\mathbf{Q} \cdot \nabla \mathbf{B} = 0$, $\mathbf{Q} = ik_{||}B_0\boldsymbol{\xi}$, and $\mathbf{B} \cdot \nabla \mathbf{Q} = -k_{||}^2 B^2 \boldsymbol{\xi}$,

$$ik_\perp \xi_z - ik_{||}\xi_y = 0 \tag{11.16}$$

Equations (11.15) and (11.16) can be solved simultaneously yielding

$$\xi_y = \frac{ik_\perp}{k^2}\xi'$$
$$\xi_z = \frac{ik_{||}}{k^2}\xi' \tag{11.17}$$

where $k^2 = k_\perp^2 + k_{||}^2$. From these relations one can easily obtain expressions for the electromagnetic fields in terms of ξ,

$$\mathbf{Q} = ik_{||}B_0\boldsymbol{\xi} = ik_{||}B_0\left(\xi\,\mathbf{e}_x + i\frac{k_\perp}{k^2}\xi'\mathbf{e}_y + i\frac{k_{||}}{k^2}\xi'\mathbf{e}_z\right)$$
$$\mathbf{E}_1 = i\omega\boldsymbol{\xi}_\perp \times \mathbf{B} = i\omega B_0\left(i\frac{k_\perp}{k^2}\xi'\mathbf{e}_x - i\xi\,\mathbf{e}_y\right) \tag{11.18}$$

The final differential equation determining the behavior of ξ is obtained from either the $\mathbf{e}_y$ or $\mathbf{e}_z$ component of Eq. (11.3). It does not matter which is used since one of the equations will always be redundant. A short calculation leads to

$$\frac{d}{dx}\left[\left(\omega^2\mu_0\rho - k_{||}^2 B_0^2\right)\frac{d\xi}{dx}\right] - k^2\left(\omega^2\mu_0\rho - k_{||}^2 B_0^2\right)\xi = 0 \tag{11.19}$$

As it stands, Eq. (11.19) is valid for arbitrary density profiles.

To complete the formulation two boundary conditions are needed. The first requires that $\xi(x \to \infty) = 0$ since there are no sources at $x \to \infty$. The second condition specifies the amplitude of the source at $x = 0$. This amplitude eventually cancels when calculating the efficiency and so can be set to an arbitrary value ξ_0 which is defined shortly. The problem is now completely formulated.

Reference case

As a reference case consider the situation where the plasma density is a constant ρ_0 for $x > 0$ and zero for $x < 0$ (see Fig. 11.3). Assume the applied frequency is not
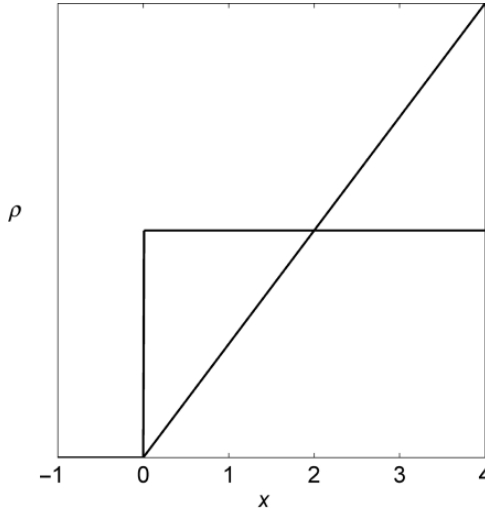
Figure 11.3   Profiles for a step function density profile and a linearly varying density profile.

resonant with the shear Alfven frequency: $\omega^2 \neq k_{||}^2 B_0^2/\mu_0\rho_0$. Under these assumptions Eq. (11.19) reduces to

$$\frac{d^2\xi}{dx^2} - k^2\xi = 0 \tag{11.20}$$

The solution for ξ is given by

$$\xi = \xi_0 e^{-kx} \tag{11.21}$$

The remaining fields have the form

$$\boldsymbol{\xi} = \left(\mathbf{e}_x - i\frac{k_\perp}{k}\mathbf{e}_y - i\frac{k_{||}}{k}\mathbf{e}_z\right)\xi$$

$$\mathbf{Q} = ik_{||}B_0\left(\mathbf{e}_x - i\frac{k_\perp}{k}\mathbf{e}_y - i\frac{k_{||}}{k}\mathbf{e}_z\right)\xi \tag{11.22}$$

$$\mathbf{E}_1 = i\omega B_0\left(-i\frac{k_\perp}{k}\mathbf{e}_x - \mathbf{e}_y\right)\xi$$

Observe that ξ decays exponentially with distance into the plasma as shown in Fig. 11.4. In spite of the exponential decay, the power flow into the plasma, which is given by the real part of the Poynting vector, has the value

$$P_x \equiv \mathrm{Re}(\mathbf{S}\cdot\mathbf{e}_x) = \frac{1}{2}\mathrm{Re}(\mathbf{E}_1 \times \mathbf{Q}\cdot\mathbf{e}_x/\mu_0) = 0 \tag{11.23}$$
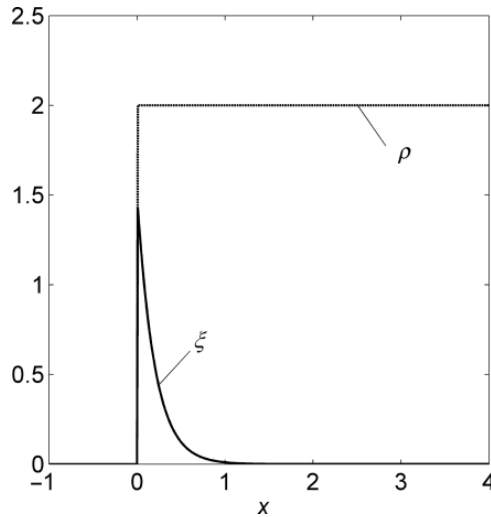
Figure 11.4   Exponential decay of ξ with distance for the step function density profile.

No power flows into the plasma. Electromagnetic energy is stored but not deposited near the surface of the plasma. The reference case therefore corresponds to an evanescent surface wave.

Mathematical solution for a linearly varying density profile

Consider now the more interesting case of a linearly varying density profile whose Alfven frequency is resonant with the applied frequency at some interior point in the plasma (see Fig. 11.3). The governing differential equation given by Eq. (11.19) can be solved by first transforming it to a standard form by introducing a normalized shifted distance for the independent variable. The shift x_0 is determined by the condition that the local Alfven frequency be resonant with the applied frequency: $\omega^2 = \omega_A^2$ where $\omega_A^2 = k_{||}^2 B_0^2 / \mu_0 \rho(x_0)$. For the linearly varying density profile, $\rho = \rho_0' x$, the singular surface is located at $x_0 = k_{||}^2 B_0^2 / \mu_0 \rho_0' \omega^2$. The normalized distance is now defined as $s = kx - s_0$ with $s_0 = kx_0 > 0$. From this definition it follows that in terms of the new coordinate the resonant surface occurs at $s = 0$ and the plasma exists over the range $-s_0 < s < \infty$.

The coordinate transformation is substituted into Eq. (11.19). A short calculation yields

$$\frac{d^2\xi}{ds^2} + \frac{1}{s}\frac{d\xi}{ds} - \xi = 0 \tag{11.24}$$

which is just the equation for the modified Bessel functions $I_0(s)$ and $K_0(s)$. The solution that vanishes as $s \to \infty$ (one of the boundary conditions) is given by

$$\xi(s) = \xi_0 K_0(s) \tag{11.25}$$

Here, ξ_0 represents the arbitrary amplitude of the source and scales out of the problem when calculating the efficiency. The source condition represents the second boundary condition.

Equation (11.25) is the desired solution. What are its implications? To answer this question temporarily put aside the physics and focus on the mathematics. The solution is not as innocent as it looks. The reason is that there is a logarithmic singularity at $s = 0$ that arises from the continuum damping. Specifically, from the properties of Bessel functions it follows that near $s = 0$

$$\xi(s) \approx -\xi_0(\ln s + C) \quad s \to 0 \tag{11.26}$$

where $C = $ constant. Therefore there is a jump in the solution across the singular surface which can be determined by noting that

$$
\begin{aligned}
s = 0_+ \quad & \xi(s) = -\xi_0(\ln s + C) \\
s = 0_- \quad & \xi(s) = -\xi_0(\ln s + C) = -\xi_0\{\ln[-(-s)] + C\} = -\xi_0[\ln(-e^{i\pi}s) + C] \\
& = -\xi_0[\ln(-s) + C + i\pi]
\end{aligned}
\tag{11.27}
$$

The jump is thus given by

$$\llbracket \xi(s) \rrbracket_{0_-}^{0_+} = i\pi\xi_0 \tag{11.28}$$

This jump can easily be taken into account in the full solution by making use of the following property of Bessel functions: $K_0(s) = K_0(-s) - i\pi I_0(-s)$ for $s < 0$. Specifically, the solution on both sides of the singularity can be rewritten in a more convenient form as follows:

$$
\begin{aligned}
0_+ < s < \infty \quad & \xi(s) = \xi_0 K_0(s) \\
-s_0 < s < 0_- \quad & \xi(s) = \xi_0[K_0(-s) - i\pi I_0(-s)]
\end{aligned}
\tag{11.29}
$$

The real and imaginary parts of ξ are illustrated in Fig. 11.5 for the case $s_0 = 2$. To avoid plotting the singular behavior at $s = 0$ in the illustration an artificial dissipation has been introduced into the solution by letting $\omega \to \omega + iv$ with $v = 0.005$. It should be emphasized that this replacement is only for the sake of plotting. The power and energy relations derived below are valid for $v \to 0$.

Physical implications of the solution

There are two physical implications that can be drawn from the solution given by Eq. (11.29). First energy is absorbed by the plasma and second, there is an optimum frequency that maximizes this absorption. The reasoning is as follows.

To demonstrate that power is absorbed by the plasma one can calculate the real part of the local *x*-directed Poynting vector. It is actually more instructive to
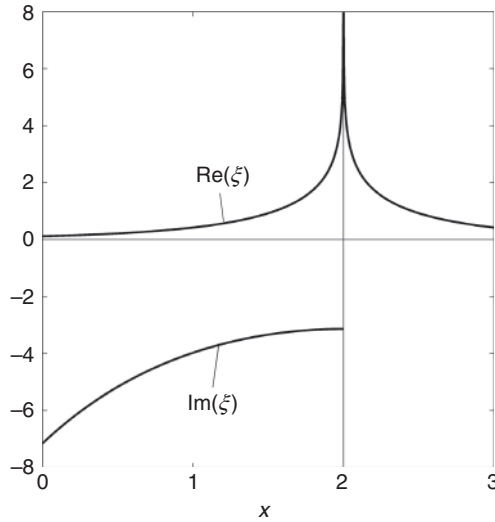
Figure 11.5   Real and imaginary part of ξ for the linearly varying density profile.

calculate the *x*-directed group velocity which is the ratio of the Poynting vector to the stored energy,

$$V_g(s) = \frac{\text{Re}(\mathbf{S} \cdot \mathbf{e}_x)}{W} \tag{11.30}$$

Here,

$$
\begin{aligned}
\text{Re}(\mathbf{S} \cdot \mathbf{e}_x) &= \frac{1}{2}\text{Re}\left(\frac{E_{1y}Q_z^*}{\mu_0}\right) = \frac{1}{2}\text{Re}\left(i\omega\frac{k_\parallel^2 B_0^2}{k^2 \mu_0}\xi\,\xi'^*\right) \\
W &= \frac{1}{2}\left(\frac{\mathbf{Q}\cdot\mathbf{Q}^*}{2\mu_0} + \frac{\rho\,\mathbf{v}\cdot\mathbf{v}^*}{2}\right) = \frac{1}{2}\left(\frac{k_\parallel^2 B_0^2}{2\mu_0} + \frac{\rho\,\omega^2}{2}\right)\left(|\xi|^2 + |\xi'|^2\right)
\end{aligned}
\tag{11.31}
$$

with prime denoting *d/ds*. A straightforward calculation then leads to the following expression for the group velocity

$$
\begin{aligned}
V_g(s) &= -\frac{\omega}{k}\frac{\pi}{s\,(2 + s/s_0)}\frac{1}{K_0^2 + K_1^2 + \pi^2\left(I_0^2 + I_1^2\right)} & -s_0 < s < 0 \\
V_g(s) &= 0 & 0 < s < \infty
\end{aligned}
\tag{11.32}
$$

where use has been made of the Bessel function relations $K_0'(s) = -K_1(s)$, $I_0'(s) = I_1(s)$, and $I_0(s)K_1(s) + I_1(s)K_0(s) = 1/s$. Also the argument of the Bessel functions in the top equation is $-s$.

Equation (11.32) is illustrated in Fig. 11.6 for the case $s_0 = 0.5$. Observe that power flows into the plasma (i.e., the group velocity is positive) from the
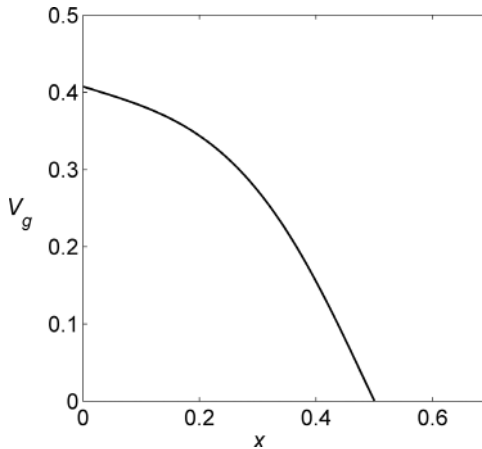
Figure 11.6   Group velocity vs. distance for the case $s_0 = 0.5$.

edge $s = -s_0$ to the singular surface $s = 0$. No power flows into the plasma past the singular surface. Importantly, at the singular surface the group velocity vanishes. This is the classic indicator of a wave resonance. Specifically, the evanescent surface wave resonates with the shear Alfven wave at the resonant surface where $\omega^2 = \omega_A^2$. The group velocity slows down, producing a build-up of energy in the plasma. At the resonant surface the Poynting vector $\text{Re}(\mathbf{S} \cdot \mathbf{e}_x) \propto 1/s$, which explicitly shows this build-up. With even an infinitesimal amount of dissipation the absorbed energy is converted into heat by the plasma.

Consider now the heating efficiency. A useful way to define the efficiency is to examine the power flow from the point of view of the source. A good analog is a simple R-L-C circuit driven by an AC voltage. The source obviously must supply the power dissipated in the resistor. The source also provides reactive power to the inductor and capacitor. However, over one cycle this power averages to zero – half the time the source delivers power and half the time power is returned to the source. Nevertheless, the source must have a high enough volt–amp rating to supply the total power at the time when the reactive power is at its maximum. Supplying the additional power over and above the pure resistive power requires a larger source which translates into additional cost.

The conclusion is that from the point of view of source economics a good definition of efficiency is the ratio of the dissipated power to the total reactive plus dissipated power. This ratio is called the power factor. Also, since the reactive power is always $90°$ out of phase with the dissipated power they must be added together as the square root of the sum of the squares. Clearly, the highest efficiency occurs at the resonant frequency $\omega = (LC)^{-1/2}$ where the reactive impedances cancel. At this frequency the efficiency is unity.
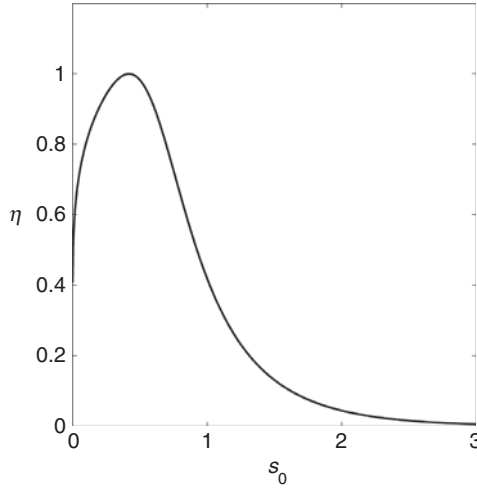
Figure 11.7   Power absorption efficiency vs. resonant frequency location.

In terms of Alfven wave heating this simple circuit picture can be interpreted as follows. The total power absorbed by the plasma P_D is given by the real part of the Poynting vector evaluated at the plasma edge $s = -s_0$ (i.e. $x = 0$): $P_D = \mathrm{Re}[\mathbf{S} \cdot \mathbf{e}_x]_{-s_0}$. Similarly, the peak reactive power supplied to the plasma P_R is given by the imaginary part of the Poynting vector: $P_R = \mathrm{Im}[\mathbf{S} \cdot \mathbf{e}_x]_{-s_0}$. If one takes into account the $90°$ phase shift between absorbed and reactive power, then a good definition of efficiency for Alfven wave heating is

$$\eta(s_0) \equiv \frac{\mathrm{Re}[\mathbf{S} \cdot \mathbf{e}_x]_{-s_0}}{\left|\mathbf{S} \cdot \mathbf{e}_x\right|_{-s_0}} = \frac{\mathrm{Re}[-i\xi\xi'^*]_{-s_0}}{\left|\xi\xi'^*\right|_{-s_0}} \tag{11.33}$$

Substituting for ξ leads to

$$\eta(s_0) = \frac{1}{\left[1 + (s_0/\pi)^2(\pi^2 I_0 I_1 - K_0 K_1)^2\right]^{1/2}} \tag{11.34}$$

where the argument of the Bessel functions is $+s_0$.

The efficiency is plotted in Fig. 11.7. Observe that the efficiency decreases as the resonant surface moves further into the plasma (i.e., as s_0 increases). The reason is that the amplitude of the evanescent surface wave exponentially decays with distance into the plasma so there is less energy available to resonate with the shear Alfven wave. The efficiency is also small when the resonant surface is very close to the edge of the plasma. Here, the surface wave has a large amplitude but

there is scarcely any plasma in which to couple energy. There is an optimum location for the resonant layer corresponding to $s_0 \approx 0.42$ for the linear density profile. At this value the efficiency is unity. The reactive powers have exactly canceled. For a given density profile the critical value of $s_0 \propto 1/\omega^2$ defines the optimum frequency at which to operate.

Conclusion

The analysis just presented shows that the existence of the Alfven wave continuum in the MHD spectrum allows efficient heating. Even though the continuum frequencies lie on the real ω axis power is absorbed and dissipated in the plasma because of resonant coupling between the driven surface wave and the continuum.

11.4 Stability of the Z-pinch

The next configuration of interest is the Z-pinch. Several topics are discussed. First, it is shown that the simple Z-pinch has poor MHD stability properties. Specifically, by means of the Energy Principle it is demonstrated that the Z-pinch is always unstable to the $m = 1$ mode and that there are strict requirements on the pressure profile to avoid instability against the $m = 0$ mode. Second, $m = 0$ stability is re-examined using the double adiabatic theory whose stability boundary is identical to that of kinetic MHD. In the regime of physical interest it is shown that the gap in the stability boundaries between ideal and double adiabatic MHD is not very large.

The last topic discussed involves a modified configuration known as the hard-core Z-pinch. This configuration has a rigid, finite radius, current-carrying conductor along the axis. It is shown that the hard core can stabilize the ideal $m = 1$ mode. Also, if the pressure profile decreases sufficiently gently then the $m = 0$ is stabilized. In other words, a hard-core Z-pinch can achieve complete MHD stability.

The stability of the hard-core Z-pinch provides the motivation for a toroidal version of the concept known as the levitated dipole (LDX Group, 1988). The corresponding magnetic geometry is quite simple, an important technological advantage. However, the hard core must be a superconducting coil fully levitated in the vacuum chamber. This is necessary in order to avoid large contact losses with any support hangers that could be used to hold the coil in place. The need to levitate the coil is a technological disadvantage. A small levitated dipole experiment was jointly built by MIT and Columbia University but has been shut down by the Department of Energy for budgetary reasons.

11.4.1 Energy Principle analysis of m ≠ 0 modes

Evaluation of δW_F

To begin recall that equilibrium pressure balance in a Z-pinch is given by

$$\frac{dp}{dr} + \frac{B_\theta}{\mu_0 r}\frac{d}{dr}(rB_\theta) = 0 \tag{11.35}$$

Since the equilibrium depends only on r, one can again Fourier analyze the perturbations with respect to θ and z : $\boldsymbol{\xi}(\mathbf{r}) = \boldsymbol{\xi}(r)\exp(im\theta + ikz)$.

The stability analysis that follows shows that the most unstable modes are localized within the plasma implying that attention need only be focused on δW_F rather than the full δW. Based on this observation, the first step in the minimization of δW_F is to examine the condition for incompressibility, $\nabla \cdot \boldsymbol{\xi} = 0$. For $m \neq 0$ modes the condition reduces to

$$\xi_{||} \equiv \xi_\theta = \frac{i}{m}\left[(r\xi_r)' + ik\xi_z\right] \tag{11.36}$$

When $m \neq 0$ it is always possible to find a $\xi_{||}$ that makes $\nabla \cdot \boldsymbol{\xi} = 0$. The plasma compressibility contribution thus vanishes when minimizing δW_F. The remaining terms in δW_F are easily evaluated using the following relations:

$$\mathbf{Q}_\perp = \frac{imB_\theta}{r}(\xi \mathbf{e}_z + \xi_z \mathbf{e}_z)$$

$$\boldsymbol{\kappa} = \mathbf{e}_\theta \cdot \nabla \mathbf{e}_\theta = -\frac{\mathbf{e}_r}{r}$$

$$\nabla \cdot \boldsymbol{\xi}_\perp + 2\boldsymbol{\xi}_\perp \cdot \boldsymbol{\kappa} = r(\xi/r)' + ik\xi_z \tag{11.37}$$

$$J_{||} = 0$$

where the simplified notation $\xi = \xi_r$ has been introduced. Note that $\mathbf{n} \cdot \boldsymbol{\kappa} = -1/r < 0$ which corresponds to unfavorable curvature.

These expressions are substituted into δW_F (i.e., Eq. (11.1)). A short calculation that makes use of the equivalent torus relation $d\mathbf{r} = 4\pi^2 R_0 rdr$ yields

$$\frac{\delta W_F}{2\pi R_0} = \pi \int_0^a W(r)rdr$$

$$W(r) = \frac{m^2 B_\theta^2}{\mu_0 r^2}\left(|\xi|^2 + |\xi_z|^2\right) + \frac{B_\theta^2}{\mu_0}\left|r(\xi/r)' + ik\xi_z\right|^2 + \frac{2p'}{r}|\xi|^2 \tag{11.38}$$

Minimization of δW_F

In analogy with the θ-pinch, one sees that ξ_z appears only algebraically. One can then complete the squares resulting in only a single positive term containing ξ_z. This contribution is minimized (i.e., set to zero) by choosing ξ_z as follows:

$$\xi_z = \frac{ikr^3}{m^2 + k^2 r^2} \left(\frac{\xi}{r}\right)' \tag{11.39}$$

Equation (11.39) is substituted into the expression for δW_F leading to

$$\frac{\delta W_F}{2\pi R_0} = \pi \int_0^a \left[\left(\frac{2p'}{r} + \frac{m^2 B_\theta^2}{\mu_0 r^2}\right)|\xi|^2 + \frac{m^2 B_\theta^2}{\mu_0(m^2 + k^2 r^2)}\left|r\left(\frac{\xi}{r}\right)'\right|^2 \right] r\,dr \tag{11.40}$$

Observe that k^2 explicitly appears only in the denominator of a positive term. Consequently for any trial function $\xi(r)$, δW_F is minimized by letting $k^2 \to \infty$. The most unstable perturbations correspond to very short wavelengths. With this choice for k^2, δW_F reduces to

$$\frac{\delta W_F}{2\pi R_0} = \pi \int_0^a \left(\frac{2p'}{r} + \frac{m^2 B_\theta^2}{\mu_0 r^2}\right)|\xi|^2 \, r\,dr \tag{11.41}$$

Equation (11.41) is the desired expression for δW_F.

Stability criterion for m $\neq$ 0 modes

An examination of Eq. (11.41) shows that the necessary and sufficient condition for stability against $m \neq 0$ modes in a Z-pinch can be written as (Kadomtsev, 1966)

$$rp' + \frac{m^2 B_\theta^2}{2\mu_0} > 0 \tag{11.42}$$

If this quantity is positive, then $\delta W_F > 0$ obviously showing sufficiency. If, on the other hand, the quantity is negative over any region of the plasma then a trial function localized within the plasma of the form shown in Fig. 11.8 will always make $\delta W_F < 0$, implying instability. This proves necessity.

Two alternate forms of the stability condition can be obtained by eliminating p' using the pressure balance relation. These forms are given by

$$\frac{r^2}{B_\theta}\left(\frac{B_\theta}{r}\right)' < \frac{1}{2}\left(m^2 - 4\right)$$
$$\frac{1}{B_\theta^2}\left(rB_\theta^2\right)' < m^2 - 1 \tag{11.43}$$

For standard Z-pinch profiles the quantity B_θ/r is a decreasing function of radius: $(B_\theta/r)' < 0$. The first form of Eq. (11.43) thus predicts stability for $m \geq 2$ modes.

Consider now the $m = 1$ mode. At large radii where the current is low, $B_\theta \propto 1/r$ corresponding to a vacuum field. In this region $(rB_\theta^2)' < 0$. The second form of Eq. (11.43) shows that the plasma is stable in this region. However, near the origin
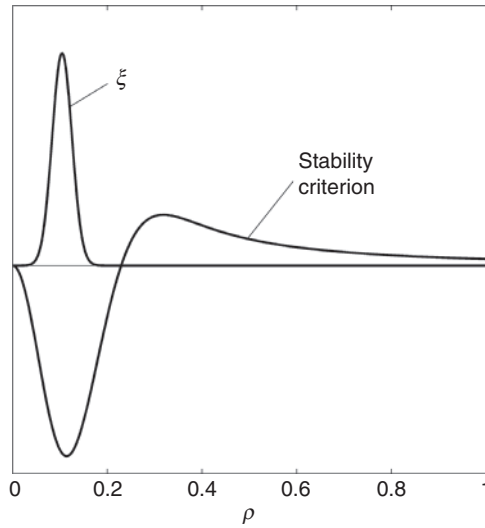
Figure 11.8   Trial function ξ that makes $\delta W_F < 0$ for $m \neq 0$ modes in a pure Z-pinch. Note that $\xi \neq 0$ only in the region where $rp' + m^2 B_\theta^2/2\mu_0 < 0$.
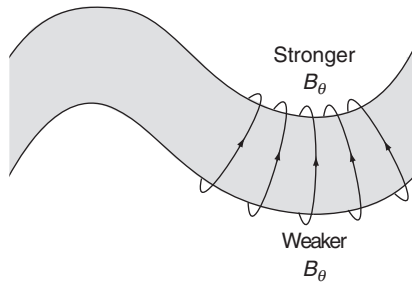

Figure 11.9   Physical mechanism of the $m = 1$ instability in a pure Z-pinch.

$B_\theta \propto r$ and $(rB_\theta^2)' > 0$. The conclusion is that the stability condition is always violated near the core of a standard Z-pinch for the $m = 1$ mode.

The source of the instability can be seen in Fig. 11.9. As the plasma undergoes an $m = 1$ deformation the magnetic lines concentrate in the tighter portion of the column, raising the value of B_θ. The resulting increased magnetic tension produces a force in the direction to further enhance the $m = 1$ deformation; hence instability.

Although the plasma perturbation has the form of a helix the instability does not correspond to a kink mode since $J_\parallel = 0$. The minimizing perturbation is best described as a competition between line bending and unfavorable curvature, with magnetic compression making a negligibly small contribution.

The $m = 1$ mode represents one of the basic instabilities present in all standard Z-pinches. It is an important part of the basis for the earlier statement that Z-pinches have unfavorable MHD stability properties.

11.4.2 Energy Principle analysis of the m = 0 *mode*

Evaluation of δW_F

The remaining mode of interest in a Z-pinch corresponds to $m = 0$. The analysis begins by examining the compressibility contribution to δW_F which is proportional to the square of $\nabla \cdot \boldsymbol{\xi}$. Specifically, for the $m = 0$ mode it follows that

$$\nabla \cdot \boldsymbol{\xi} = \frac{1}{r}(r\xi)' + \frac{im\xi_\theta}{r} + ik\xi_z = \frac{1}{r}(r\xi)' + ik\xi_z = \nabla \cdot \boldsymbol{\xi}_\perp \tag{11.44}$$

Recall now that the only appearance of $\xi_\parallel$ in δW_F occurs in the plasma compressibility term. Since the appearance of $\xi_\parallel \equiv \xi_\theta$ vanishes for $m = 0$ it never appears anywhere else in the calculation. Consequently it is not possible to choose a $\xi_\parallel$ that makes $\nabla \cdot \boldsymbol{\xi} = 0$. One must set $\nabla \cdot \boldsymbol{\xi} = \nabla \cdot \boldsymbol{\xi}_\perp$ and maintain the effects of plasma compressibility when minimizing δW_F.

The evaluation of δW_F is straightforward and again shows that ξ_z appears only algebraically,

$$\frac{\delta W_F}{2\pi R_0} = \pi \int_0^a W(r)rdr$$
$$W(r) = \frac{B_\theta^2}{\mu_0} \left| r(\xi/r)' + ik\xi_z \right|^2 + \gamma p \left| (r\xi)'/r + ik\xi_z \right|^2 + \frac{2p'}{r} \left| \xi \right|^2 \tag{11.45}$$

Minimization of δW_F

The next step is to complete the squares with respect to ξ_z. The result is that ξ_z appears only in a single positive term whose minimum value is set to zero by choosing

$$ik\xi_z = -\frac{B_\theta^2 \left[r(\xi/r)' \right] + \mu_0\gamma p \left[(r\xi)'/r \right]}{B_\theta^2 + \mu_0\gamma p} \tag{11.46}$$

Substituting back into δW_F yields

$$\frac{\delta W_F}{2\pi R_0} = \pi \int_0^a \left[\left(\frac{4\gamma B_\theta^2}{B_\theta^2 + \mu_0\gamma p} \right) p + 2rp' \right] \frac{|\xi|^2}{r^2} rdr \tag{11.47}$$

Stability criterion for the m = 0 *mode*

Following the reasoning associated with the $m \neq 0$ modes (i.e., Eq. (11.41)) one can conclude that the necessary and sufficient condition for stability against the $m = 0$ mode is given by (Kadomstev, 1966)
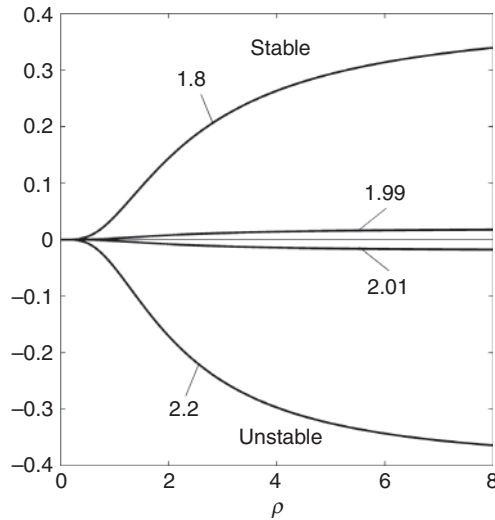
Figure 11.10   Stability criterion given by Eq. (11.48) vs. radius for several values (1.8, 1.99, 2.01, 2.2) of the profile parameter v. The ratio of specific heats has been set to $\gamma = 2$.

$$-\frac{rp'}{p} < \frac{2\gamma B_\theta^2}{B_\theta^2 + \mu_0\gamma p} \tag{11.48}$$

This condition can be satisfied near the origin of a standard Z-pinch although the profiles are a little sensitive to the higher-order on-axis curvature terms. However, it can only be satisfied near the outside of the plasma if the pressure decreases sufficiently gradually. Specifically, at large radii in a well-confined plasma, $p \ll B_\theta^2/\mu_0$ and Eq. (11.48) reduces to

$$-\frac{rp'}{p} < 2\gamma \tag{11.49}$$

For $\gamma = 5/3$ one sees that the pressure must decrease more gradually than $p < C/r^{10/3}$. One important consequence of Eq. (11.49) is that for a Z-pinch to be stable against the $m = 0$ mode it must have a finite, although perhaps small, pressure at the wall. It cannot have $p = 0$ at the wall. These results are summarized in Fig. 11.10 where the stability criterion for the analytically simple case of $\gamma = 2$ is plotted for several pressure and magnetic field profiles given by

$$p(\rho) = \frac{p_0}{(1 + \rho^2)^v}$$

$$B_\theta^2(\rho) = \frac{2p_0}{v - 1}\frac{1}{\rho^2}\left[1 - \frac{(1 + v\rho^2)}{(1 + \rho^2)^v}\right] \tag{11.50}$$
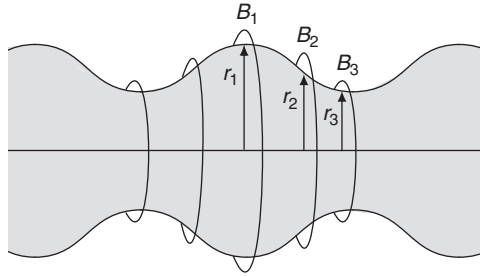
Figure 11.11   Physical mechanism of the $m = 0$ sausage instability in a pure Z-pinch.

where $\rho = r/a$ with a the characteristic scale length of the plasma (but less than the wall radius b). The parameter v determines how gradually the pressure decreases with r at large radii. Observe that for the slowly decreasing profile ($v = 1.8$) the stability criterion is always satisfied. The marginal stability profile corresponds to $v = 2$. For a more rapidly decreasing profile ($v = 2.2$) the stability boundary is violated everywhere.

The $m = 0$ instability is an interchange mode often known as the "sausage instability." The basic force driving the instability is illustrated in Fig. 11.11. When an $m = 0$ sausage perturbation is superimposed on the Z-pinch equilibrium the magnetic field in the throat regions increases since the plasma carries the same current in a smaller cross section. The increased magnetic tension produces a destabilizing force which tends to further constrict the column. However, the plasma pushes back when being compressed, thereby providing a stabilizing force. When the tension force dominates, instability occurs. At marginal stability the two forces are balanced, corresponding to equality of the two terms in Eq. (11.48). The minimizing perturbation for the $m = 0$ instability represents a competition between unfavorable curvature and plasma compression. The line bending is zero.

An alternate physical picture of the sausage instability can be obtained by examining the motion of the plasma from a single particle point of view. This picture shows why the curvature is unfavorable. The physics is illustrated in Fig. 11.12. An $m = 0$ perturbation has been superimposed on the surface of the plasma. The electrons and ions in the bulges (and throats) develop opposing guiding center velocities along z because of the curvature drift. The sign of the drifts, illustrated for a bulge region, corresponds to "unfavorable" negative curvature: $\boldsymbol{\kappa} = -\mathbf{e}_r/r$. Now, because of the sausage perturbation, the opposing drifts set up a charge separation as shown in the figure. This charge separation creates an electric field in the axial direction whose sign also alternates between bulges and
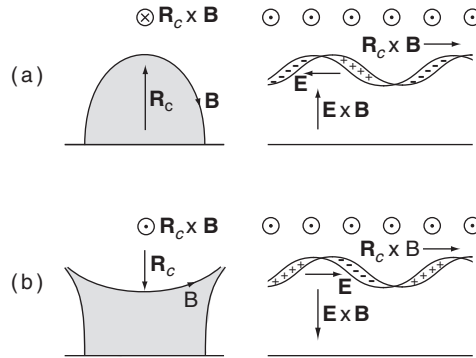
Figure 11.12   Single particle picture of the $m = 0$ interchange mode in a pure Z-pinch. In (a) an interchange perturbation modulates the plasma surface. The opposing curvature drifts set up a charge separation leading to a destabilizing $\mathbf{E} \times \mathbf{B}$ drift. In (b) the curvature direction changes sign leading to stability.

throats. The electric field in turn produces an $\mathbf{E} \times \mathbf{B}$ drift of the plasma. When the curvature is negative, the direction of the $\mathbf{E} \times \mathbf{B}$ velocity is such as to further reinforce the perturbation in both the bulges and throats, leading to instability. When the curvature is positive, as in a cusp geometry, the sign of the drifts reverses and the perturbation is stabilized.

Validity of ideal MHD stability for the m = 0 mode in a Z-pinch

The last point to note is that the $m = 0$ stability criterion depends on γ, the ratio of specific heats. This dependence arises from the ideal MHD adiabatic equation of state, which as previously stated, is highly unreliable for fusion-grade plasmas. What is needed is an analysis based on the more realistic kinetic MHD model. In this connection recall from Chapter 10 that $m = 0$ kinetic MHD stability in a Z-pinch is identical to that of the double adiabatic model. It is therefore of interest to calculate the corresponding form of the stability criterion given by Eq. (11.48) to see the differences in the stability boundaries. This is the next task.

11.4.3 Double adiabatic Energy Principle analysis of the m = 0 mode

Evaluation of δW_{CGL}

The evaluation of δW_{CGL} from the double adiabatic Energy Principle follows from the simplification of Eqs. (10.27) and (10.28). One again focuses on the internal $m = 0$ mode in a Z-pinch. The corresponding form of the Energy Principle can be written as

$$\delta W_{CGL} = \delta W_F + \frac{1}{2} \int \frac{p}{3} \left| \nabla \cdot \boldsymbol{\xi}_\perp + 3\boldsymbol{\xi}_\perp \cdot \boldsymbol{\kappa} \right|^2 d\mathbf{r} \qquad (11.51)$$

where δW_F is given by Eq. (11.45). Substituting the cylindrical Z-pinch equilibrium into the additional term in Eq. (11.51) leads to

$$\frac{\delta W_{CGL}}{2\pi R_0} = \pi \int_0^a W(r) r dr$$

$$W(r) = \frac{B_\theta^2}{\mu_0} \left| r(\xi/r)' + ik\xi_z \right|^2 + \frac{5}{3} p \left| (r\xi)'/r + ik\xi_z \right|^2 \qquad (11.52)$$

$$+ \frac{1}{3} p \left| r^2 \left(\xi/r^2\right)' + ik\xi_z \right|^2 + \frac{2p'}{r} \left|\xi\right|^2$$

Minimization of δW_{CGL}

Observe that as with the previous Z-pinch calculations, the quantity $ik\xi_z$ appears only algebraically. Completing the squares and setting the resulting term to zero yields the following relation for the minimizing ξ_z:

$$ik\xi_z = -\frac{B_\theta^2 \left[r(\xi/r)' \right] + (5\mu_0 p/3) \left[(r\xi)'/r \right] + (\mu_0 p/3) \left[r^2(\xi/r^2)' \right]}{B_\theta^2 + 2\mu_0 p} \qquad (11.53)$$

This relation is now substituted into (11.52). A straightforward calculation leads to the desired expression for δW_{CGL}:

$$\frac{\delta W_{CGL}}{2\pi R_0} = \pi \int_0^a \left[\left(\frac{7B_\theta^2 + 5\mu_0 p}{B_\theta^2 + 2\mu_0 p} \right) p + 2rp' \right] \frac{\left|\xi\right|^2}{r^2} r dr \qquad (11.54)$$

Stability criterion for the m = 0 *mode*

From Eq. (11.54) one can easily obtain the necessary and sufficient condition for double adiabatic stability against the $m = 0$ mode in a Z-pinch. This condition and the corresponding one for ideal MHD (with $\gamma = 5/3$) for comparison are given by

$$-\frac{rp'}{p} < \frac{7B_\theta^2 + 5\mu_0 p}{2B_\theta^2 + 4\mu_0 p} \qquad \text{double adiabatic MHD}$$

$$\qquad\qquad\qquad\qquad\qquad\qquad\qquad\qquad\qquad\qquad (11.55)$$

$$-\frac{rp'}{p} < \frac{10B_\theta^2}{3B_\theta^2 + 5\mu_0 p} \qquad \text{ideal MHD}$$

Note that near the origin double adiabatic MHD is considerably more stable than ideal MHD: $-rp'/p < 5/4$ for double adiabatic MHD while $-rp'/p < 0$ for ideal

MHD. However, this improved stability is not very important since the ideal MHD model is already stable in this region.

The more interesting region is near the outside of the plasma where a sufficiently weak pressure gradient is required for stability. In this region corresponding to $p \to 0$ the two stability criteria reduce to

$$-\frac{rp'}{p} < \frac{7}{2} = 3.50 \qquad \text{double adiabatic MHD}$$

$$-\frac{rp'}{p} < \frac{10}{3} = 3.33 \qquad \text{ideal MHD}$$

(11.56)

There is not a very large difference in the stability boundaries. This analysis thereby provides one example of the small gap between the predictions of ideal MHD and double adiabatic MHD. Consequently, one would not make a very large error using ideal MHD.

Summary of stability in a standard Z-pinch

Based on the analysis just presented, the conclusion is that a standard Z-pinch is always unstable to $m = 1$ perturbations and may likely be unstable to $m = 0$ perturbations. In fact the $m = 0$ mode was often observed experimentally in early, rapidly shock heated Z-pinch experiments leading to a catastrophic termination of the plasma. The theory plus experimental results form the basis for earlier statements attributing very poor ideal MHD stability properties to a standard Z-pinch.

11.4.4 The hard-core Z-pinch

An interesting way to modify the standard Z-pinch that potentially overcomes its poor MHD stability properties is to add a rigid, finite radius, current-carrying conductor along the axis. For obvious reasons the resulting configuration is called a hard-core Z-pinch. A toroidal version of the concept, known as the levitated dipole (LDX Group, 1998), was built several years ago but unfortunately has recently been shut down for budgetary reasons. Even so, it is of help in the development of MHD intuition to demonstrate how the presence of a hard core can stabilize the strong MHD instabilities in a standard Z-pinch. That is the goal of the present subsection.

Hard-core Z-pinch equilibria

The typical equilibrium profiles (specified below) of a hard-core Z-pinch are illustrated in Fig. 11.13. Observe that the pressure vanishes at $r = r_c$, the surface of the hard-core conductor. The pressure rises and then decreases gradually at large
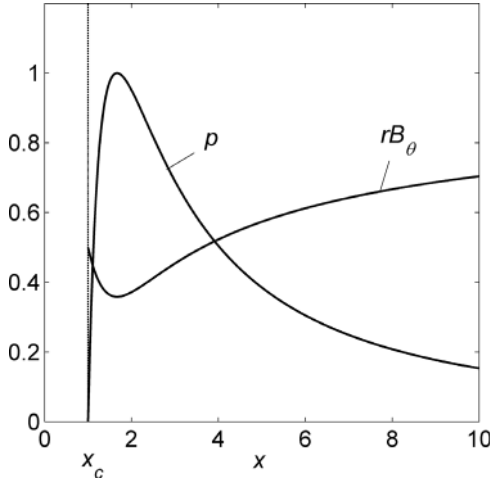
Figure 11.13   Equilibrium profiles for a hard-core Z-pinch. Shown are $p(\rho)/p_{\max}$ and $rB_\theta/(rB_\theta)_\infty$ for $\beta = 0.5$. Also $x = r^2/r_c^2$ and $x_c = 1$ corresponds to the coil radius.

radii to avoid the $m = 0$ instability. A gradually decreasing pressure can be generated experimentally by switching from rapid shock heating to slower RF heating with the profile controlled by the location of the resonant frequency.

The presence of the hard core leads to a B_θ profile that is large at the surface of the conductor and then decreases, approximately proportional to $B_\theta \propto 1/r$, although with a superimposed diamagnetic depression due to the plasma pressure. The $1/r$ dependence near the conductor stabilizes the $m = 1$ mode and is in fact the primary MHD motivation for the hard core.

A simple choice for the pressure profile that satisfies the basic requirements of a hard-core Z-pinch is given by

$$p(r) = K\frac{r^2 - r_c^2}{r^5} \tag{11.57}$$

The constant K is a measure of the peak pressure. The exponent 5 has been chosen to guarantee $m = 0$ ideal MHD stability at large radii. This equation can be rewritten in a simpler form by introducing $x = r^2/r_c^2$,

$$p(x) = K_P\frac{x - 1}{x^{5/2}} \tag{11.58}$$

where K_P is a new constant related to the maximum pressure $p_{\max}$, which occurs at $x = 5/3$, and is given by

$$K_P = \frac{3}{2}\left(\frac{5}{3}\right)^{5/2} p_{\max} \approx 5.38\, p_{\max} \tag{11.59}$$

The magnetic field is easily found by integrating the pressure balance relation and expressing the results in terms of x. The result is

$$xB_\theta^2(x) = K_I - \frac{2\mu_0 K_P}{3}\frac{9x-5}{x^{3/2}} \tag{11.60}$$

Here K_I is a free integration constant. Its value is determined by noting that the magnetic field far from the plasma approaches $B_\theta(r \to \infty) = \mu_0(I_C + I_P)/2\pi r$, where I_C is the hard-core current and I_P is the plasma current. Therefore,

$$K_I = \left[\frac{\mu_0(I_C + I_P)}{2\pi r_c}\right]^2 \tag{11.61}$$

In the analysis that follows it is convenient to introduce normalized variables plus the plasma β. The definitions are as follows:

$$\beta = \frac{16\pi^2}{\mu_0 I^2}\int_{r_c}^\infty pr\,dr = \frac{32}{3}\frac{\pi^2 r_c^2}{\mu_0 I^2}K_P \qquad \text{beta}$$

$$P = \frac{2\mu_0 p(x)}{(\mu_0 I/2\pi r_c)^2} = \frac{3\beta}{4}\frac{x-1}{x^{5/2}} \qquad \text{normalized } p(x) \tag{11.62}$$

$$b_\theta^2 = \frac{xB_\theta^2(x)}{(\mu_0 I/2\pi r_c)^2} = 1 - \frac{\beta}{4}\frac{9x-5}{x^{3/2}} \qquad \text{normalized } B_\theta^2(x)$$

with $I = I_C + I_P$. The last equilibrium relation of interest corresponds to the global pressure balance relation. This relation is easily obtained by noting that $B_\theta(r_c) = \mu_0 I_C/2\pi r_c$ and evaluating $b_\theta^2(\infty) - b_\theta^2(1)$. A simple calculation shows that global pressure balance relates β to the coil and plasma currents by

$$\beta = 1 - \left(\frac{I_C}{I_C + I_P}\right)^2 \tag{11.63}$$

The basic equilibrium relations for the hard-core Z-pinch profiles have now been established. The next goal is to investigate the effectiveness of the hard core in providing high β stabilization of the plasma against MHD instabilities. The analysis that follows shows that there are in fact three limits on β: (1) an equilibrium β limit (which does not exist for the standard Z-pinch); (2) an $m = 1$ stability limit; and (3) an $m = 0$ stability limit. All of these limits occur at high values of β showing that a hard core is a very effective means of stabilizing the standard Z-pinch.

The hard-core Z-pinch equilibrium limit

The hard-core Z-pinch has an equilibrium β limit. This limit can be seen mathematically by examining a plot of b_θ^2 vs. x as shown in Fig. 11.14. Observe that as
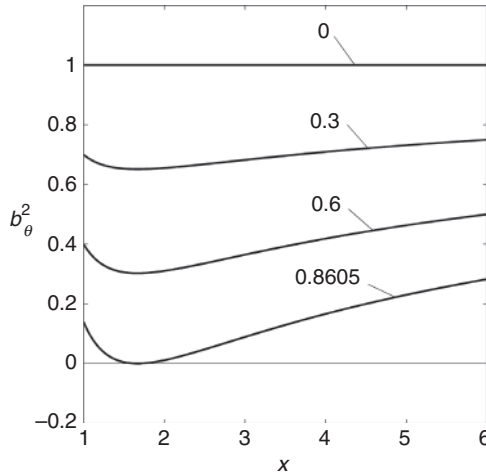
Figure 11.14   Equilibrium β limit in a hard-core Z-pinch as shown in a plot of b_θ^2 vs. x.

β increases the diamagnetic dip due to the plasma pressure becomes increasingly deeper. Eventually a critical value $\beta = \beta_{\mathrm{eq}}$ is reached above which the minimum b_θ^2 becomes negative. Since $b_\theta^2 \geq 0$ for physical solutions the value β_{eq} corresponds to the equilibrium β limit.

The value of β_{eq} is easily found by simultaneously setting $b_\theta^2 = db_\theta^2/dx = 0$. A short calculation yields

$$\beta \leq \beta_{\mathrm{eq}} = \frac{2}{5}\left(\frac{5}{3}\right)^{3/2} \approx 0.861 \tag{11.64}$$

This clearly is only a mild constraint.

Physically, the limit arises because a minimum amount of coil current is required to push the plasma away from the coil surface $r = r_c$; that is, a coil current is needed to produce a hollow pressure profile. The value of the coil current relative to the plasma current at the equilibrium limit is obtained from Eq. (11.63)

$$\frac{I_C}{I_P} \geq \frac{I_{\mathrm{eq}}}{I_P} = \frac{\left(1 - \beta_{\mathrm{eq}}\right)^{1/2}}{1 - \left(1 - \beta_{\mathrm{eq}}\right)^{1/2}} \approx 0.594 \tag{11.65}$$

The conclusion is that for the simple model under consideration, the hard-core coil current must be about 60% (or greater) of the plasma current to avoid the equilibrium β limit.
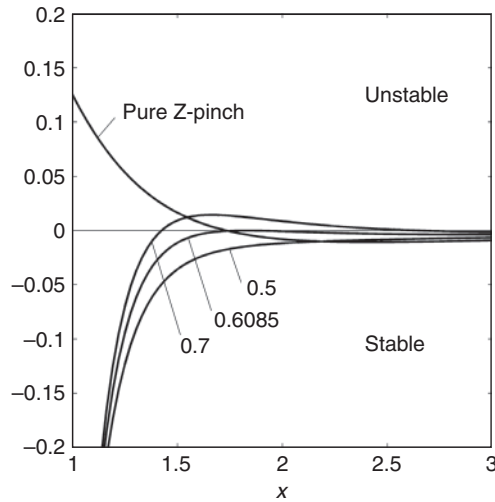
Figure 11.15   Stability criterion given by Eq. (11.66) as a function of radius for the $m = 1$ mode in a pure Z-pinch and a hard-core Z-pinch. The curve labels correspond to different values of β.

The hard-core Z-pinch m = 1 stability limit

The $m = 1$ stability criterion given by Eq. (11.43) applies to the hard-core Z-pinch as well as the standard Z-pinch since the only assumption used in the derivation is cylindrical symmetry with a purely poloidal equilibrium magnetic field. Recall that the stability criterion is a local criterion that must be satisfied at each value of r. In terms of the normalized variables the $m = 1$ stability criterion has the form

$$\frac{d}{dx}\left(\frac{b_\theta^2}{x^{1/2}}\right) < 0 \tag{11.66}$$

For the standard Z-pinch the criterion is always violated near the origin since $B_\theta \propto r \propto x^{1/2}$. The hard core dramatically changes this situation. Near the surface of the coil, $B_\theta \propto 1/r \propto 1/x^{1/2}$ implying stability. In fact in the region between the coil radius r_c and the radius of the maximum pressure r_{max} the pressure gradient is positive and the curvature is negative producing an overall favorable curvature term in δW_F. Instability is only possible for $r > r_{max}$ where the curvature contribution becomes negative. Intuitively, it is clear that it becomes more difficult to satisfy the stability criterion as β gets larger since the slope of b_θ^2 becomes increasingly positive. Refer to Fig. 11.15.

A quantitative prediction for the critical β against the $m = 1$ instability can be obtained by substituting the equilibrium profile given by Eq. (11.62) into Eq. (11.66). A short calculation shows that the local stability criterion can be written as

$$\beta \leq \frac{2x^{3/2}}{9x - 10} \tag{11.67}$$

The function on the right-hand side has a minimum at $x = 10/3 \approx 3.33$ and leads to a β limit given by

$$\beta \leq \beta_{m=1} = \frac{1}{10}\left(\frac{10}{3}\right)^{3/2} \approx 0.609 \qquad (11.68)$$

The $m = 1$ stability limit is considerably lower than the equilibrium β limit but nonetheless is still quite high in terms of its absolute value.

Lastly, the value $\beta_{m=1}$ is substituted into the global equilibrium pressure balance relation (i.e., Eq. (11.63)) to determine the minimum coil current to suppress the $m = 1$ instability. One finds

$$\frac{I_C}{I_P} \geq \frac{I_{m=1}}{I_P} = \frac{(1 - \beta_{m=1})^{1/2}}{1 - (1 - \beta_{m=1})^{1/2}} \approx 1.67 \qquad (11.69)$$

The coil current must be more than one and a half times larger than the plasma current to avoid the instability.

The hard-core Z-pinch m = 0 *stability limit*

A similar stability analysis holds for the $m = 0$ sausage instability. In terms of the normalized quantities the stability criterion given by Eq. (11.48) can be rewritten as

$$-\frac{x}{P}\frac{dP}{dx} \leq \frac{10b_\theta^2}{6b_\theta^2 + 5xP} \qquad (11.70)$$

where γ has been set to 5/3. The equilibrium profiles are now substituted into Eq. (11.70). A straightforward calculation leads to the following condition on β for stability:

$$\beta \leq \frac{8x^{3/2}(x + 5)}{63x^2 - 40x + 25} \qquad (11.71)$$

This function has a minimum at $x \approx 6.95$. At this value the β limit and corresponding minimum coil current have the values

$$\beta \leq \beta_{m=0} \approx 0.628$$
$$\frac{I_C}{I_P} \geq \frac{I_{m=0}}{I_P} = \frac{(1 - \beta_{m=0})^{1/2}}{1 - (1 - \beta_{m=0})^{1/2}} \approx 1.56 \qquad (11.72)$$

For the model profiles under consideration the $m = 0$ β limit is slightly higher but still comparable to the $m = 1$ limit.

Summary of the hard-core Z-pinch

The standard Z-pinch is ideal MHD unstable to the $m = 0$ and $m = 1$ modes. The addition of a current-carrying, hard-core conductor along the axis greatly improves the stability. For the simple model investigated there is an equilibrium β limit which is quite large: $\beta_{eq} = 0.861$. Both the $m = 0$ and $m = 1$ modes set stricter limits on the maximum allowable β but these limits are high: $\beta_{m=0} \approx 0.628$ and $\beta_{m=1} \approx 0.609$. However, a large wall radius is needed in order for the edge pressure to be small. For example, a normalized wall radius $r_w/r_c = 6$ leads to a pressure ratio $p(r_w)/p_{\max} \approx 0.024$.

A toroidal version of the concept, known as the levitated dipole, must have a levitated superconducting coil in order to avoid losses to any support structure. The fact that the coil has to be superconducting also implies that advanced fuels, such as D-D, must be used in any potential fusion applications. The reason is to avoid neutron heating and quenching of the superconducting magnet as would occur with D-T as the fuel.

11.5 General stability properties of the screw pinch

The screw pinch is the cylindrical analog of the axisymmetric torus. It combines θ-pinch and Z-pinch fields with the goal of discovering configurations that have favorable stability properties at sufficiently high β to be of fusion interest. Both field components are necessary. The θ-pinch field basically provides MHD stability while the Z-pinch field provides equilibrium when the cylinder is bent into a torus.

In this section six general properties of screw pinch stability are discussed:

- A general minimized form of δW plus the corresponding differential equation for the minimizing trial function are derived.
- An analytic criterion, known as "Suydam's criterion" (Suydam, 1958), is derived from the minimized δW which determines MHD stability against localized interchanges.
- A simple and elegant procedure based on the differential equation for the minimizing perturbation is presented that demonstrates how to test for MHD stability in a general screw pinch. This is known as Newcomb's procedure (Newcomb, 1960).
- The analysis of δW is further generalized by the derivation of the full eigenmode differential equation for the general screw pinch, as originally obtained by Hain and Lust (1958).
- The full eigenmode equation is then used to derive Goedbloed and Sakanaka's (1974) "oscillation theorem," which shows how growth rates and the number of radial nodes in the eigenfunction are inversely correlated. This is important in understanding the significance of Suydam's criterion.

- Lastly, the effect of replacing a perfectly conducting wall with a resistive wall is investigated. The result is a general stability criterion that shows how the resistive wall growth rate is related to growth rates with and without a perfectly conducting wall.

All the results in this section are valid for an arbitrary screw pinch. In the following sections the results are applied to two toroidal configurations that are reasonably well represented by their cylindrical analogs: the "straight" tokamak and the reversed field pinch (RFP).

11.5.1 Evaluation of δW *for a general screw pinch*

The evaluation of δW for a screw pinch is straightforward but involves a considerable amount of analysis. The final result is a one-dimensional integral involving only the radial component of the plasma displacement. The derivation is carried out for the Extended Energy Principle and thus includes the contribution from the vacuum region. The steps are outlined below.

Setting up the evaluation of δW_F

To begin recall that the one-dimensional equilibrium pressure balance relation for a screw pinch is given by

$$\frac{d}{dr}\left(p + \frac{B_z^2}{2\mu_0}\right) + \frac{B_\theta}{\mu_0 r}\frac{d}{dr}(rB_\theta) = 0 \tag{11.73}$$

The cylindrical symmetry again allows one to Fourier analyze the displacement vector with respect to θ and $z : \boldsymbol{\xi}(\mathbf{r}) = \boldsymbol{\xi}(r)\exp(im\theta + ikz)$. It is the symmetry with respect to two coordinates that ultimately leads to the algebraic elimination of two components of $\boldsymbol{\xi}$ when minimizing δW_F.

In carrying out the analysis it is convenient to decompose the displacement vector as follows:

$$\boldsymbol{\xi} = \boldsymbol{\xi}_\perp + \xi_{||}\mathbf{b} = \xi\,\mathbf{e}_r + \eta\,\mathbf{e}_\eta + \xi_{||}\mathbf{b} \tag{11.74}$$

where

$$\begin{aligned} \eta &= (\xi_\theta B_z - \xi_z B_\theta)/B & \mathbf{e}_\eta &= (B_z\mathbf{e}_\theta - B_\theta\mathbf{e}_z)/B \\ \xi_{||} &= (\xi_\theta B_\theta + \xi_z B_z)/B & \mathbf{b} &= (B_\theta\mathbf{e}_\theta + B_z\mathbf{e}_z)/B \end{aligned} \tag{11.75}$$

Also needed are two quantities that frequently appear in the analysis

$$\begin{aligned} F(r) &\equiv \mathbf{k}\cdot\mathbf{B} = kB_z + mB_\theta/r \\ G(r) &\equiv \mathbf{e}_r\cdot\mathbf{k}\times\mathbf{B} = mB_z/r - kB_\theta \end{aligned} \tag{11.76}$$

These definitions and expressions are substituted into the general form for δW_F given by Eq. (11.1), after which the minimization can proceed.
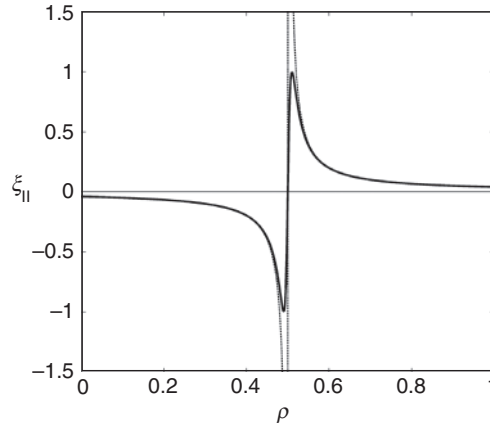
Figure 11.16   Bounded trial function for $\xi_\parallel$ that makes the plasma compressibility contribution to δW_F vanish.

Incompressibility

The first step in the minimization is to examine the incompressibility condition. The question is whether or not a $\xi_\parallel$ can be found that makes $\nabla \cdot \boldsymbol{\xi} = 0$. If so, then this is the $\xi_\parallel$ that minimizes the plasma compressibility term. Setting $\nabla \cdot \boldsymbol{\xi} = 0$ yields an expression for $\xi_\parallel$ given by

$$\xi_\parallel = i\frac{B}{F}\nabla \cdot \boldsymbol{\xi}_\perp \tag{11.77}$$

If the very special case of zero shear (i.e., $(rB_z/B_\theta)' = 0$) is excluded, then the denominator $F(r)$ will in general be non-zero except perhaps at a finite number of discrete radii. When $F(r) \neq 0$ within plasma then a well-behaved $\xi_\parallel$ can always be chosen in accordance with Eq. (11.77), which thereby makes the plasma compressibility term in δW_F vanish.

Even when $F(r) = 0$ at isolated surfaces, the plasma compressibility term can be made negligibly small with a cleverly chosen, well-behaved $\xi_\parallel$. The situation is illustrated in Fig. 11.16 for the case of a single resonant surface at $r = r_s$. The thin curve is a plot of $\xi_\parallel$ as given by Eq. (11.77). Note the singularity at $r = r_s$. The solid curve represents a trial function for $\xi_\parallel$ of the form

$$\xi_\parallel = \frac{iBF}{F^2 + \delta^2}\nabla \cdot \boldsymbol{\xi}_\perp \tag{11.78}$$

where $\delta^2 > 0$ is a small positive constant. This form of $\xi_\parallel$ is bounded and closely approximates the form required to make $\nabla \cdot \boldsymbol{\xi} = 0$ everywhere except near the singular surface. Since $\nabla \cdot \boldsymbol{\xi}$ is not exactly zero everywhere there is a potentially finite contribution to the plasma compressibility contribution from the vicinity of the singular surface whose value will depend upon δ^2.

This contribution can be evaluated by noting that when Eq. (11.78) is substituted into the expression for $\nabla \cdot \boldsymbol{\xi}$ one obtains

$$\nabla \cdot \boldsymbol{\xi} = \frac{\delta^2}{F^2 + \delta^2} \, \nabla \cdot \boldsymbol{\xi}_\perp \tag{11.79}$$

The contribution to δW_F from the plasma compressibility term can now be easily evaluated by expanding the integrand about $r = r_s$: $r = r_s + x$, $F(r) \approx F'(r_s)x$. One finds,

$$\frac{\delta W_C}{2\pi R_0} = \pi \int \gamma p \left| \nabla \cdot \boldsymbol{\xi} \right|^2 r \, dr \approx \pi \left[\gamma p r \left| \nabla \cdot \boldsymbol{\xi}_\perp \right|^2 \right]_{r_s} \int \frac{\delta^4}{\left(F'^2 x^2 + \delta^2 \right)^2} \, dx \tag{11.80}$$

Since the integrand decays rapidly for large $|x|$ the limits of integration can be extended to $-\infty < x < \infty$ with negligible error. Carrying out the integration yields

$$\frac{\delta W_C}{2\pi R_0} = \frac{\pi^2}{2} \left[\frac{\gamma p r \left| \nabla \cdot \boldsymbol{\xi}_\perp \right|^2}{\left| F' \right|} \right]_{r_s} \left| \delta \right| \propto \left| \delta \right| \tag{11.81}$$

Thus, for arbitrarily small but non-zero δ

$$\frac{\delta W_C}{2\pi R_0} \to 0 \tag{11.82}$$

implying that plasma compressibility makes a vanishingly small contribution to δW_F even when isolated singular surfaces exist in the plasma.

Evaluation of $\delta \mathrm{W_F}$

The remaining terms in δW_F are functions only of ξ and η. The evaluation of δW_F is conceptually similar to that of the θ-pinch and Z-pinch except that the algebra is more cumbersome since the equilibrium contains two non-zero field components. The evaluation of δW_F as given by Eq. (11.1) requires the following quantities.

$$\mathbf{Q}_\perp = \nabla \times (\boldsymbol{\xi}_\perp \times \mathbf{B})_\perp = iF\xi \mathbf{e}_r + \left\{ iF\eta + \frac{\xi}{B} \left[B_\theta B_z' - r B_z (B_\theta / r)' \right] \right\} \mathbf{e}_\eta$$

$$\boldsymbol{\kappa} = \mathbf{b} \cdot \nabla \mathbf{b} = -\frac{B_\theta^2}{rB^2} \mathbf{e}_r$$

$$\nabla \cdot \boldsymbol{\xi}_\perp + 2\boldsymbol{\xi}_\perp \cdot \boldsymbol{\kappa} = \frac{1}{r} (r\xi)' - 2\frac{B_\theta^2}{rB^2}\xi + i\frac{G}{B}\eta$$

$$\mu_0 J_{||} = \mu_0 \mathbf{J} \cdot \mathbf{B} = \frac{1}{B} \left[B_z (rB_\theta)'/r - B_\theta B_z' \right] \tag{11.83}$$

where F and G are given by Eq. (11.76). These expressions are substituted into δW_F (after setting $\delta W_C = 0$) leading to

$$\frac{\delta W_F}{2\pi R_0} = \frac{\pi}{\mu_0} \int W(r) \, r dr$$

$$W(r) = F^2 \left| \xi \right|^2 + \left| iF\eta + \frac{\xi}{B} \left[B_\theta B_z' - rB_z(B_\theta/r)' \right] \right|^2 \qquad \text{shear Alfven}$$

$$+ B^2 \left| \frac{1}{r}(r\xi)' - 2\frac{B_\theta^2}{rB^2}\xi + i\frac{G}{B}\eta \right|^2 \qquad \text{comp. Alfven}$$

$$+ 2\frac{\mu_0 p' B_\theta^2}{rB^2} \left| \xi \right|^2 \qquad \text{curvature}$$

$$- \mu_0 J_{||} \left\{ iF\left(\xi\eta^* - \xi^*\eta\right) - \left|\xi\right|^2 \left[\frac{B_\theta B_z'}{B} - \frac{rB_z(B_\theta/r)'}{B} \right] \right\} \qquad \text{kink}$$

$$(11.84)$$

The task now is to simplify this complicated looking expression.

Minimization of δW_F

The minimization of δW_F begins with the observation that η appears only algebraically. After a short calculation the terms in $W(r)$ that explicitly contain η can be grouped together as follows:

$$W_\eta(r) = k_0^2 B^2 \left| \eta \right|^2 + 2\frac{kBB_\theta}{r}\left(i\eta\xi^* - i\eta^*\xi\right) + \frac{GB}{r}\left[i\eta\left(r\xi^*\right)' - i\eta^*(r\xi)' \right]$$

$$= \left| ik_0 B\eta + 2\frac{kB_\theta}{rk_0}\xi + \frac{G}{rk_0}(r\xi)' \right|^2 - \left| 2\frac{kB_\theta}{rk_0}\xi + \frac{G}{rk_0}(r\xi)' \right|^2 \qquad (11.85)$$

where $k_0^2 = k^2 + m^2/r^2$. Since η appears only in a positive term, δW_F is minimized by choosing

$$\eta = \frac{i}{rk_0^2 B} \left[2kB_\theta\xi + G(r\xi)' \right] \qquad (11.86)$$

With this choice for η the remaining terms in $W(r)$ can be written as

$$W(r) = A_1 \xi'^2 + 2A_2 \xi \, \xi' + A_3 \xi^2 \qquad (11.87)$$

Note that, without loss in generality, ξ can be considered to be a real quantity since the A_j are real coefficients. A straightforward calculation shows that the A_j are given by

$$A_1 = \frac{F^2}{k_0^2}$$

$$A_2 = \frac{1}{rk_0^2}\left(k^2 B_z^2 - \frac{m^2 B_\theta^2}{r^2}\right)$$

$$A_3 = F^2 + 2\frac{\mu_0 p' B_\theta^2}{rB^2} + \frac{B^2}{r^2}\left(1 - 2\frac{B_\theta^2}{B^2}\right)^2$$

$$- \frac{1}{r^2 k_0^2}\left(G + 2kB_\theta\right)^2 + 2\frac{B_\theta B_z}{rB}\left[\frac{B_\theta B_z'}{B} - \frac{rB_z}{B}\left(\frac{B_\theta}{r}\right)'\right]$$

(11.88)

The middle term in Eq. (11.87) is now integrated by parts. The expression for δW_F reduces to

$$\frac{\delta W_F}{2\pi^2 R_0/\mu_0} = \int_0^a \left(f\xi'^2 + g\xi^2\right)dr + \left(\frac{FF^\dagger}{k_0^2}\right)_a \xi^2(a)$$

(11.89)

Here $F^\dagger = kB_z - mB_\theta/r$, $f = rA_1$, and $g = rA_3 - (rA_2)'$. After some tedious algebra that makes use of the equilibrium pressure balance relation, the coefficient g can be greatly simplified. The final form of the coefficients f and g are then given by (Newcomb, 1960)

$$f(r) = \frac{rF^2}{k_0^2}$$

$$g(r) = 2\mu_0 \frac{k^2}{k_0^2}p' + \frac{k_0^2 r^2 - 1}{k_0^2 r^2}rF^2 + 2\frac{k^2}{rk_0^4}FF^\dagger$$

(11.90)

Equations (11.89) and (11.90) are the desired form of δW_F, the fluid contribution to δW.

Evaluation of δW$_V$ *and* δW$_S$

To complete the derivation of δW one must evaluate the surface and vacuum contributions. The analysis is simplified by making the realistic practical assumption that no surface currents flow on the plasma–vacuum interface. This implies that $\delta W_S = 0$.

What remains is the vacuum contribution which is evaluated as follows. In the vacuum region the magnetic field can be written as $\hat{\mathbf{B}}_1 = \nabla V_1$ with V_1 satisfying $\nabla^2 V_1 = 0$. The solution for V_1 assuming a perfectly conducting wall boundary condition at $r = b$ (i.e., $(\partial V_1/\partial r)_b = 0$) has the form

$$V_1(r) = A_0\left(K_r - \frac{K_b'}{I_b'}I_r\right)\exp(im\theta + ikz)$$

(11.91)

where $K_\rho = K_m(\zeta_\rho)$, $I_\rho = I_m(\zeta_\rho)$, $\zeta_\rho = |k|\rho$, and $K_m(\zeta_\rho)$, $I_m(\zeta_\rho)$ are modified Bessel functions. Also, prime denotes differentiation with respect to the argument and without loss in generality one can assume that $m \geq 0$ and $-\infty < k < \infty$.

The free coefficient A_0 is related to $\xi(a)$ through the boundary condition at the plasma–vacuum interface: $\hat{B}_{1r}(a) = \mathbf{e}_r \cdot \nabla \times (\boldsymbol{\xi}_\perp \times \hat{\mathbf{B}})_a$. This condition reduces to

$$\left(\frac{\partial V_1}{\partial r}\right)_a = i(F\xi)_a \tag{11.92}$$

which leads to

$$A_0 = \frac{iF_a}{K_a}\left[1 - \left(\frac{K_b'}{I_b'}\right)\left(\frac{I_a}{K_a}\right)\right]\xi_a \tag{11.93}$$

Here, $F_a = F(a)$ and $\xi_a = \xi(a)$.

The last step is to make use of the fact that $\nabla^2 V_1 = 0$ and transform δW_V from a volume to a surface integral. The result is

$$\delta W_V = \frac{1}{2\mu_0}\int_V \left|\hat{\mathbf{B}}_1\right|^2 d\mathbf{r} = \frac{1}{2\mu_0}\int_V \nabla \cdot (V_1^* \nabla V_1)\, d\mathbf{r} = -\frac{1}{2\mu_0}\int_S V_1^*(\mathbf{n} \cdot \nabla V_1)\, dS$$
$$= -\frac{2\pi^2 R_0 a}{\mu_0}\left(V_1^* \frac{\partial V_1}{\partial r}\right)_a \tag{11.94}$$

The negative sign appears because $\mathbf{n} = \mathbf{e}_r$ points radially outward. Substituting Eqs. (11.91) and (11.93) into Eq. (11.94) leads to the desired form of δW_V,

$$\frac{\delta W_V}{2\pi^2 R_0/\mu_0} = \left(\frac{r^2 F^2 \Lambda}{m}\right)_a \xi_a^2 \tag{11.95}$$

where Λ, the enhanced stabilization factor due to the conducting wall, can be written as

$$\begin{aligned}
\Lambda &= -\frac{mK_a}{|ka|K_a'}\left[\frac{1 - (K_b' I_a)/(I_b' K_a)}{1 - (K_b' I_a')/(I_b' K_a')}\right] \\
&\approx \frac{1 + (a/b)^{2m}}{1 - (a/b)^{2m}} \qquad kb \sim ka \ll 1 \\
&\approx \frac{m}{ka}\coth[k(b-a)] \qquad kb \sim ka \gg 1
\end{aligned} \tag{11.96}$$

Summary

In summary, the Energy Principle for a general screw pinch reduces to a one-dimensional quadratic integral involving only the radial component of the plasma displacement ξ. For internal modes ξ must satisfy $\xi(a) = 0$ with $\delta W = \delta W_F$ given by

$$\frac{\delta W_F}{2\pi^2 R_0/\mu_0} = \int_0^a \left(f\xi'^2 + g\xi^2\right) dr$$

$$\frac{d}{dr}\left(f\frac{d\xi}{dr}\right) - g\xi = 0 \qquad (11.97)$$

The exact minimizing ξ satisfies the differential equation on the second line, obtained by a simple calculation that sets the variation of δW_F to zero.

For external modes $\xi(a) \neq 0$. In this case the boundary and vacuum terms must be included and δW has the form

$$\frac{\delta W}{2\pi^2 R_0/\mu_0} = \int_0^a (f\xi'^2 + g\xi^2)\,dr + \left(\frac{FF^\dagger}{k_0^2} + \frac{r^2 F^2 \Lambda}{m}\right)_a \xi^2(a) \qquad (11.98)$$

In these expressions f, g are given by Eq. (11.90) and Λ by Eq. (11.96).

The evaluation of δW is exact in that the minimization with respect to $\xi_\parallel$ and η have been carried out without approximation. Note also that $f(r)$ is positive while $g(r)$ can have either sign. Consequently, both terms are competitive and further simplifications as occurred for the θ-pinch and Z-pinch are not possible for the general screw pinch.

11.5.2 Suydam's criterion

Although a general set of stability criteria for the screw pinch cannot be obtained analytically there is one criterion that can be derived that provides an easy-to-test necessary, but not sufficient, condition against a special class of modes – localized interchanges. This criterion is known as "Suydam's criterion" (Suydam, 1958).

The motivation for examining stability against such modes follows from the observation that if $F(r) = 0$ at some radius $r = r_s$ then each term in $f(r_s)$ and $g(r_s)$ also vanishes at this radius except for the one in $g(r_s)$ proportional to $p'(r_s)$. Since $p'(r_s) < 0$ in general, then $g(r_s) < 0$, which is destabilizing. Consequently, a perturbation localized about $r = r_s$ has a reasonable likelihood of causing a pressure-driven instability. Furthermore, the mode has the structure of an interchange since $k_\parallel = \mathbf{k} \cdot \mathbf{B}/B = F/B$ vanishes at $r = r_s$. A perturbation with $k_\parallel = 0$ tends to minimize the bending of the magnetic lines which is the signature of an interchange mode.

It is important to keep in mind that a perturbation localized about $r = r_s$ does not automatically imply instability when $p'(r_s) < 0$. The reason is that when the

equilibrium magnetic field has shear then away from the resonant surface $F(r) \neq 0$: $F(r) \approx F'(r_s)(r - r_s)$. Even though this term is small, when multiplied by ξ', which is large because of the localization, the product can become finite. Thus, the $f\xi'^2$ term in δW_F produces a stabilizing contribution.

The end result is that Suydam's criterion describes a competition between unfavorable curvature and localized line bending. The derivation of the criterion proceeds as follows.

Simplification of $\delta\mathrm{W_F}$

The expression for δW_F can be greatly simplified by exploiting the assumption that the mode is localized about the singular surface. Right at the outset one must recognize that localized eigenfunctions are a special subclass of the most general eigenfunctions and therefore, whatever stability criterion may be derived, will be a necessary but not sufficient condition. With this proviso the functions f and g are expanded about the singular surface, $F(r_s) = 0$ by letting $r = r_s + x$ and assuming the eigenfunction is non-zero only for very small x. The first non-vanishing contributions to f and g are then given by

$$
\begin{aligned}
f &\approx \left(\frac{rF'^2}{k_0^2} \right)_{r_s} x^2 \\
g &\approx \left(\frac{2\mu_0 k^2 p'}{k_0^2} \right)_{r_s}
\end{aligned}
\tag{11.99}
$$

These expressions lead to a simplified form of δW_F, and its normalized form $\delta\hat{W}_F$, that can be written as

$$
\frac{\delta W_F}{2\pi^2 R_0/\mu_0} = \left(\frac{rF'^2}{k_0^2} \right)_{r_s} \delta\hat{W}_F
$$

$$
\delta\hat{W}_F = \int_{-\Delta}^{\Delta} \left[x^2 \left(\frac{d\xi}{dx} \right)^2 - D_S\xi^2 \right] dx
\tag{11.100}
$$

$$
D_S = \left(\frac{2\mu_0 k^2 p'}{rF'^2} \right)_{r_s}
$$

Here $\Delta \ll a$ is a measure of the localization of the eigenfunction. Also, the parameter D_S can be further simplified by noting that the axial wave number at the resonant surface must be chosen so that

$$k = -\left(\frac{mB_\theta}{rB_z}\right)_{r_s} \tag{11.101}$$

When this is substituted into Eq. (11.100) the result is an expression for D_S that is only a function of the equilibrium fields (and not m),

$$D_S = -\left(\frac{2\mu_0 p' q^2}{rB_z^2 q'^2}\right)_{r_s} \tag{11.102}$$

where $q(r) = rB_z/R_0 B_\theta$ is the safety factor and R_0 is the major radius of the equivalent torus.

Minimization of $\delta\hat{W}_F$

The minimization of δW_F starts off in a straightforward way but subtleties arise shortly thereafter. Even so the resulting difficulties are resolved leading to an easy-to-apply criterion known as "Suydam's criterion." The analysis begins by setting the variation of $\delta\hat{W}_F$ in Eq. (11.100) to zero in order to obtain the equation that determines the minimizing ξ. This equation is given by

$$\frac{d}{dx}\left(x^2 \frac{d\xi}{dx}\right) + D_S\xi = 0 \tag{11.103}$$

which has a simple analytic solution,

$$\xi = c_1 X^{p_1} + c_2 X^{p_2}$$
$$p_{1,2} = -\frac{1}{2} \pm \frac{1}{2}(1 - 4D_S)^{1/2} \tag{11.104}$$
$$X = |x|$$

Now, observe that at least one solution for ξ is always singular. Consequently, one cannot simply use the solution given by Eq. (11.104) as a trial function. The integrals could become infinite depending upon the strength of the singularity. This is the subtlety mentioned above. The resolution is to modify ξ near $x = 0$ so that it becomes a well-behaved, allowable trial function capable of making $\delta\hat{W}_F < 0$. As is shown below, the question of stability or instability depends upon the sign of $1 - 4D_S$.

Consider first the situation where $1 - 4D_S < 0$. In this case the roots $p_{1,2}$ are complex and ξ has the form

$$\xi = \frac{1}{X^{1/2}}[C_1 \sin(k_r \ln X) + C_2 \cos(k_r \ln X)] \qquad X = |x|$$
$$k_r = \frac{1}{2}(4D_S - 1)^{1/2} \tag{11.105}$$
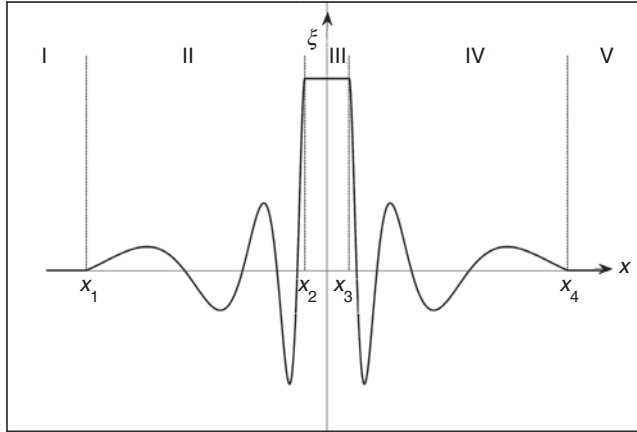
Figure 11.17   Trial function leading to Suydam instability.

The solution as $x \to 0$ oscillates infinitely rapidly with a diverging envelope proportional to $1/X^{1/2}$.

Because of the oscillatory behavior it is always possible to construct a well-behaved ξ that always makes $\delta \hat{W}_F < 0$ (i.e., instability). The modified ξ is illustrated in Fig. 11.17. Observe that $\xi = 0$ in regions I and V so that $\delta \hat{W}_F(I) = \delta \hat{W}_F(V) = 0$. In regions II and IV ξ satisfies the minimizing differential equation with solutions given by Eq. (11.105). The corresponding contributions to $\delta \hat{W}_F$ are obtained by multiplying Eq. (11.103) by ξ and integrating over each region. Since either ξ or ξ' is zero at the endpoints of both regions, one finds

$$
\delta \hat{W}_F(II) = \int_{x_1}^{x_2} \left(x^2 \xi'^2 - D_S \xi^2 \right) dx = (x^2 \xi \xi')\Big|_{x_1}^{x_2} = 0
$$
$$
\delta \hat{W}_F(IV) = \int_{x_3}^{x_4} \left(x^2 \xi'^2 - D_S \xi^2 \right) dx = (x^2 \xi \xi')\Big|_{x_3}^{x_4} = 0
$$
(11.106)

The total contribution to $\delta \hat{W}_F$ arises from region III where $\xi = \xi_0 = $ constant and is given by

$$
\delta \hat{W}_F = \delta \hat{W}_F(III) = \int_{x_2}^{x_3} \left(x^2 \xi'^2 - D_S \xi^2 \right) dx = -D_S \xi_0^2 (x_3 - x_2)
$$
(11.107)

By assumption $D_S > 1/4$. Therefore, $\delta \hat{W}_F < 0$ and the system is unstable.

When $D_S < 1/4$ both roots $p_{1,2}$ are real. In this case it is not possible to construct a trial function that makes $\delta \hat{W}_F < 0$. Since the solutions are non-oscillatory the solutions in regions II and IV intersect points x_2 and x_3 with a finite slope. Therefore, the contributions to $\delta \hat{W}_F(II)$ and $\delta \hat{W}_F(IV)$ are finite and their net contribution is always positive, dominating the unstable $\delta \hat{W}_F(III)$ contribution.
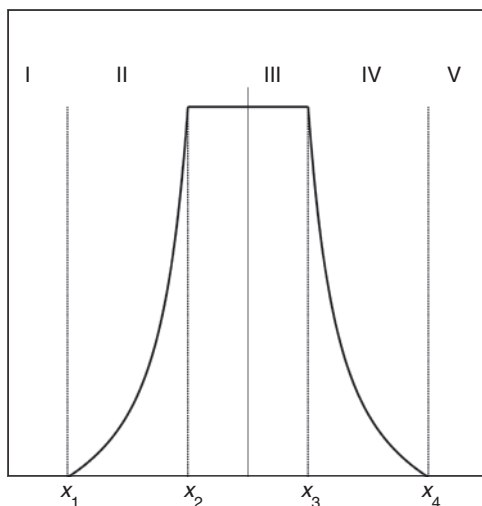
Figure 11.18   Trial function satisfying the Suydam stability criterion.

For instance, for a trial function of the form shown in Fig. 11.18 a straightforward calculation shows that

$$
\delta \hat{W}_F = \xi_0^2 (x_3 - x_2) \left(-D_S + \frac{1}{2} \right)
$$
$$
+ \xi_0^2 (x_3 + x_2) \frac{\alpha}{2} \left[\frac{(x_2/x_1)^\alpha + 1}{(x_2/x_1)^\alpha - 1} + \frac{1 + (x_3/x_4)^\alpha}{1 - (x_3/x_4)^\alpha} \right]
\tag{11.108}
$$

where $\alpha = (1 - 4D_S)^{1/2}$. Since $D_S < 1/4$ by assumption it is clear that $\delta \hat{W}_F > 0$ implying stability against this form of perturbation.

The stability criterion $1 - 4D_S > 0$ is known as Suydam's criterion. If it is violated for any r_s in the interval $0 < r_s < a$ the plasma is unstable. The usual form for Suydam's criterion for stability is written as (Suydam, 1958)

$$
r B_z^2 \left(\frac{q'}{q} \right)^2 + 8 \mu_0 p' > 0
\tag{11.109}
$$

The stability boundary defined by this equation represents a balance between two competing effects. The destabilizing term results from the combination of a negative p' and the negative unfavorable curvature of the B_θ field. The stabilizing term, proportional to q'^2 represents the work done bending the magnetic field lines when interchanging two flux tubes in a system with shear.

A final question to address is whether a mode with such a highly localized structure would actually be important in a real experiment or would instead be

dominated by other physics. The answer is connected with the oscillation theorem which is derived in Section 11.5.5. Briefly, the theorem shows that violation of Suydam's criterion corresponds to the existence of an accumulation point of discrete unstable eigenvalues collecting at $\omega^2 \to 0$. Equally important the oscillation theorem shows that the eigenvalues and eigenfunctions exhibit Sturmian behavior; that is, if a highly oscillatory localized mode with a certain growth rates exists (as occurs when Suydam's criterion is violated), a gross, non-oscillatory mode with zero nodes must also exist, and this mode will have the maximum growth rate for the given m and k. It is the guaranteed existence of such a large-scale mode that makes violation of Suydam's criterion important.

11.5.3 Newcomb's procedure

A general analysis of the screw pinch Energy Principle has been given by Newcomb (1960). This analysis shows how a knowledge of the radial structure of ξ, as determined by the minimizing equation,

$$\frac{d}{dr}\left(f\frac{d\xi}{dr}\right) - g\xi = 0 \tag{11.110}$$

can be used to derive necessary and sufficient conditions for the stability of an arbitrary screw pinch. The end results are not simple analytic criteria, such as Suydam's criterion. Instead, the results provide a simple procedure that can be easily implemented numerically to test stability against all MHD modes. A key feature of the analysis is the use of ideas associated with Sturm's separation theorem, which will be described below.

Overall, there are three steps in Newcomb's procedure, which should be carried out in the following order:

1. Test for Suydam stability.
2. Test for general internal mode stability.
3. Test for external mode stability.

Clearly, if Suydam's criterion is violated the plasma is unstable and no further work is required. Hereafter, it is assume that Suydam's criterion is satisfied and attention is next focused on general internal mode stability. This is the step that involves the most work. Once internal mode stability is established it is then straightforward to test for external mode stability. For a configuration to be MHD stable it must satisfy all three criteria. Steps (2) and (3) are now discussed in detail.

Internal mode stability when $F(r) \neq 0$

To begin consider Eq. (11.110) and assume that m and k are such that $F(r) \neq 0$ for $0 < r < a$. For this case it is shown how Sturm's separation theorem can be used to
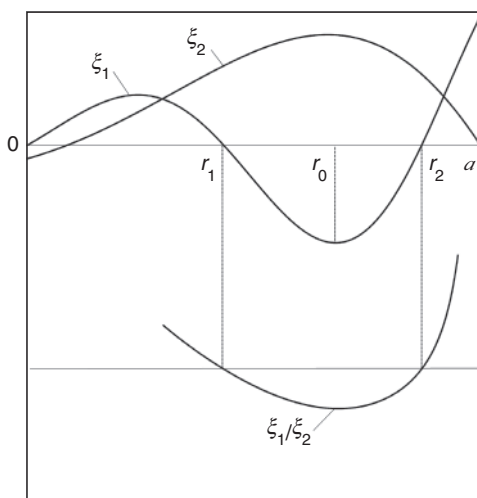
Figure 11.19 Illustration of the separation theorem.

test for internal mode stability. Since $F(r) \neq 0$ then Eq. (11.110) is non-singular (i.e., $f \neq 0$) and has two smooth independent solutions $\xi_1(r)$ and $\xi_2(r)$. Thus, any $\xi(r)$ can be written as

$$\xi(r) = c_1 \xi_1(r) + c_2 \xi_2(r) \tag{11.111}$$

Without loss of generality, $\xi_1(r)$ can be chosen to be regular at $r = 0$ but in general, $\xi_1(a) \neq 0$. Similarly, $\xi_2(r)$ can be chosen so that $\xi_2(a) = 0$ but in general is not regular at $r = 0$.

The first part of the analysis shows that when $\xi_1(r)$ has a zero in the interval (0, a), one can always construct a trial function that makes $\delta W_F < 0$, implying instability. If no zero exists then $\delta W_F > 0$ and the plasma is stable to internal modes for the given m and k. The proof of these statements is based on Sturm's separation theorem, which shows that the zeros of any two independent solutions of Eq. (11.110) (e.g., $\xi_1(r)$ and $\xi_2(r)$) must alternate in radial location.

Sturm's theorem is easily demonstrated by assuming the opposite; that is, assume that $\xi_1(r)$ has two consecutive zeros located at r_1 and r_2 while $\xi_2(r) \neq 0$ in the interval (r_1, r_2) (see Fig. 11.19). Clearly $\xi_1'(r) = 0$ at some intermediate radius r_0 with $r_1 < r_0 < r_2$. Therefore, for $r_1 < r < r_2$, the well-behaved function $Y(r) = \xi_1(r) / \xi_2(r)$ also has zeros at r_1 and r_2 and a zero derivative at some modified internal point. This is also illustrated in Fig. 11.19.

One now computes the derivative $Y'(r)$,

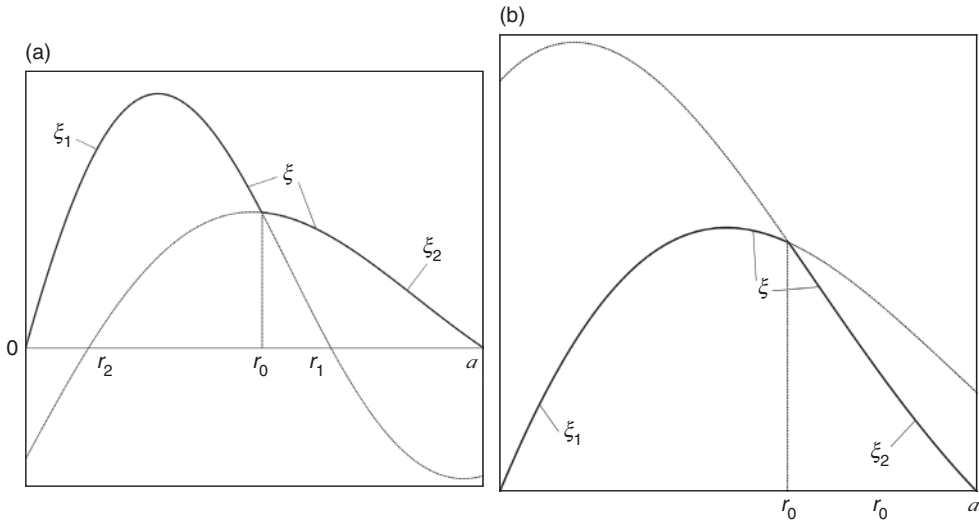$$Y' = \frac{\xi_2 \xi_1' - \xi_1 \xi_2'}{\xi_2^2} \tag{11.112}$$

Figure 11.20   Trial function showing (a) instability and (b) stability by means of Newcomb's analysis for the case where $F(r) \neq 0$ for $0 < r < a$.

Since Y' must be zero somewhere in $r_1 < r < r_2$, this can only occur if the Wronskian $\xi_2 \xi_1' - \xi_1 \xi_2' = 0$ in this same interval. However, if this were true then the assumption that $\xi_1(r)$ and $\xi_2(r)$ are independent is contradicted. Specifically, if one solves Eq. (11.111) for arbitrary initial conditions at $r = 0$, the resulting $\xi_{arb}(r)$ and ξ_{arb}' can always be written as a linear superposition of ξ_1 and ξ_2 assuming they are independent,

$$\xi_{arb}(r) = c_1 \xi_1(r) + c_2 \xi_2(r)$$
$$\xi_{arb}'(r) = c_1 \xi_1'(r) + c_2 \xi_2'(r) \tag{11.113}$$

The condition that finite c_1, c_2 exist for arbitrary initial conditions on $\xi_{arb}(r)$ requires that the determinant $\xi_2 \xi_1' - \xi_1 \xi_2'$ not vanish anywhere, which contradicts the requirement that Y' vanish somewhere in the interval $r_1 < r < r_2$. The conclusion is that $\xi_2(r)$ must have a zero in this interval. In other words the zeros of $\xi_1(r)$ and $\xi_2(r)$ must alternate. This is Sturm's separation theorem.

Using this theorem, one next constructs a trial function $\xi(r)$ using $\xi_1(r)$ and $\xi_2(r)$ in different parts of the interval $(0, a)$ as shown in Fig. 11.20a. Note that $\xi(r)$ shown as the dark curve is a well-behaved allowable trial function. To show instability, assume that $\xi_1(r)$ has a single zero at $r = r_1$. (The results can be easily generalized to include multiple zeros.) Sturm's separation theorem guarantees that a radius r_2 lying in the range $0 < r_2 < r_1$ must exist for which $\xi_2(r_2) = 0$. Likewise, in the interval $r_2 < r < a$, $\xi_2(r)$ cannot have a second zero. The trial function is constructed so that $\xi(r) = \xi_1(r)$ for $0 < r < r_0$ where r_0 is the intersection point.
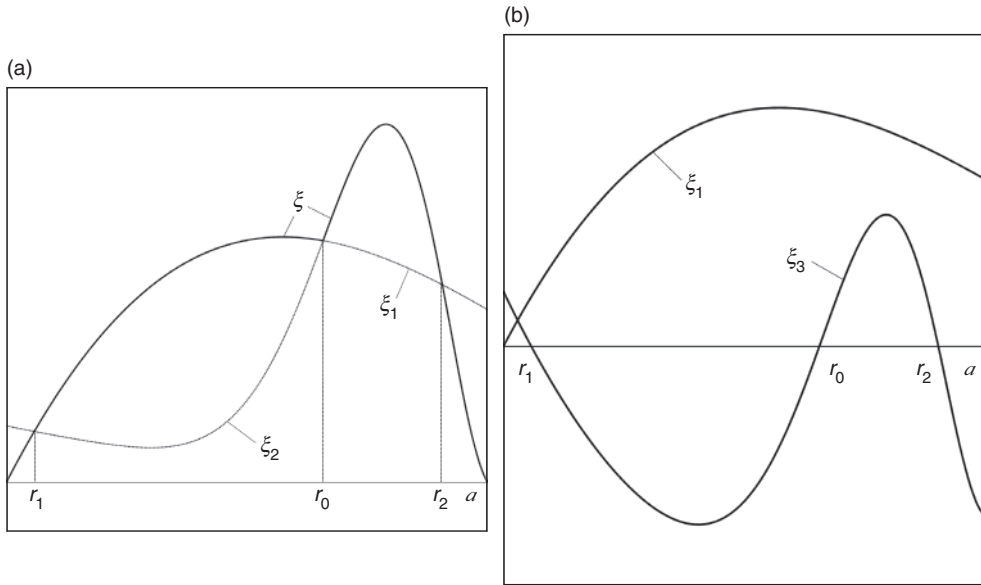
Figure 11.21   Graphical demonstration that an apparently unstable trial function as shown in (a) actually violates the separation theorem as shown in (b).

Similarly $\xi(r) = \xi_2(r)$ for $r_0 < r < a$. The value of $\delta\hat{W}_F$ is obtained by multiplying Eq. (11.110) by $\xi(r)$ and integrating over the separate regions. The result is

$$\delta\hat{W}_F = f\xi_1\xi_1'\Big|_0^{r_0} + f\xi_2\xi_2'\Big|_{r_0}^a = f(r_0)\xi(r_0)\big[\xi_1'(r_0) - \xi_2'(r_0)\big] \qquad (11.114)$$

Because of the separation theorem the topology of the eigenfunction must be such that $\xi_1'(r_0) < \xi_2'(r_0)$ implying that $\delta\hat{W}_F < 0$; the system is unstable.

Consider next the situation for stability. In this case assume that $\xi_1(r)$ has no zeros in the interval $(0, a)$. The only type of trial function that can be constructed that is consistent with the separation theorem and the boundary conditions is shown in Fig. 11.20b. In this case Eq. (11.114) still applies but the topology requires that $\xi_1'(r_0) > \xi_2'(r_0)$; the system is stable.

Note that it is not possible to construct a trial function as shown in Fig. 11.21a where neither $\xi_1(r)$ nor $\xi_2(r)$ has a zero, but one function, $\xi_2(r)$ for instance, undulates such that $\xi_1'(r_0) < \xi_2'(r_0)$ implying instability. If neither function has a zero the topology requires that two additional intersections must exist at r_1 and r_2. Consequently, if one replaces $\xi_1(r)$ and $\xi_2(r)$ with an equivalent set of independent functions $\xi_1(r)$ and $\xi_3(r) = \xi_2(r) - \xi_1(r)$ then in the region $r_1 < r < r_2$, $\xi_1(r)$ and $\xi_3(r)$ have the form illustrated in Fig. 11.21b. Clearly the separation theorem is violated and the situation shown in Fig. 11.21a cannot exist.

The first part of Newcomb's analysis can thus be summarized as follows. For values of m and k such that $F(r) \neq 0$ in the interval $(0, a)$ the screw pinch is stable

against internal modes if and only if the non-trivial solution to the minimizing equation (i.e., Eq. (11.111)) that is regular at $r = 0$ does not have a zero crossing in $0 < r < a$.

Internal mode stability when $F(r_s) = 0$

The stability procedure is slightly more complicated when $F(r)$ has a single or multiple isolated zeros in $0 < r < a$. In this case the minimizing equation is singular at each radius r_s where $F(r_s) = 0$. A prescription is thus needed to determine how to calculate $\xi(r)$ in the vicinity of each singular surface. The prescription is as follows.

Recall from Eq. (11.104) that in the vicinity of any r_s the behavior of ξ is given by $\xi = c_1 X^{p_1} + c_2 X^{p_2}$, where $X = |x|$ and $p_{1,2} = -(1/2) \pm (1/2)(1 - 4D_S)^{1/2}$. Now, the assumption that Suydam's criterion has been satisfied implies that $1 - 4D_S > 0$. Both roots $p_{1,2}$ are real with $p_1 > -1/2$ and $p_2 < -1/2$. The root p_1 corresponds to a "weak" singularity while p_2 corresponds to a "strong" singularity.

The proper behavior of ξ is then determined by the physical condition that the potential energy remain bounded in the vicinity of r_s. For either root one finds

$$
\int \left(x^2 \xi'^2 - D_S \xi^2 \right) dx = p x^{2p+1} \Big|_{x \to 0}
$$
$$
= 0 \qquad\qquad p_1 > -1/2 \qquad (11.115)
$$
$$
= \infty \qquad\qquad p_2 < -1/2
$$

The conclusion is that the root p_1 is allowable while p_2 leads to a divergent energy. Therefore, in the vicinity of a singular surface the trial function ξ must be chosen to contain only the small solution (i.e., the root p_1). In effect the singularity acts like a regularity condition at the origin in that it singles out one of the two independent solutions as admissible.

Because of this the interval $(0, a)$ must be broken into sub-intervals whose boundaries correspond to the successive zeros of $F(r)$. The first and last sub-intervals are bounded by $r = 0$ and $r = a$ respectively. Each sub-interval must be tested for stability separately. The previous analysis for $F(r) \neq 0$ for $0 < r < a$ can be directly applied to each sub-interval. A plot of the trial function $x^{1/2}\xi$ for the second sub-interval of a one singularity profile is illustrated in Fig. 11.22. The resulting value of $\delta \hat{W}_F$ is given by

$$
\delta \hat{W}_F = f \xi_1 \xi_1' \Big|_{r_s}^{r_0} + f \xi_2 \xi_2' \Big|_{r_0}^{a} = f(r_0)\xi(r_0)\left[\xi_1'(r_0) - \xi_2'(r_0)\right] \qquad (11.116)
$$

Note that the requirement that $\xi_1(r)$ contain only the small solution guarantees that the contribution at $r = r_s$ vanishes. As before, if $\xi_1(r)$ has a zero in the sub-interval then $\delta \hat{W}_F < 0$. If not, $\delta \hat{W}_F > 0$.
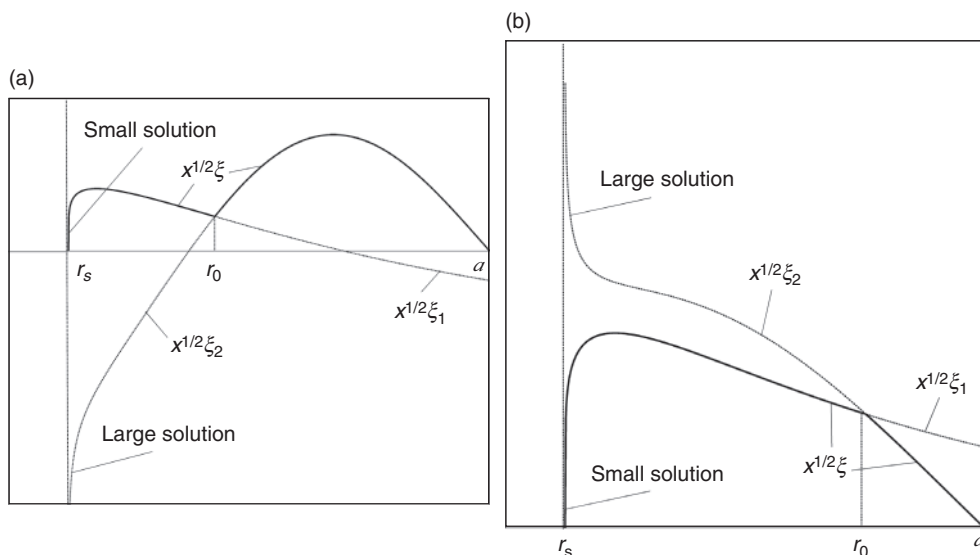
Figure 11.22   Unstable trial function $x^{1/2}\xi$ for a plasma with one singular surface in $0 < r < a$: (a) instability, (b) stability. Note that the trial function contains only the small solution at the resonant surface.

The second part of Newcomb's analysis can thus be summarized as follows for profiles with one singular surface. For values of m and k such that $F(r_s) = 0$ for $0 < r_s < a$ the screw pinch is stable against internal modes if and only if (1) Suydam's criterion is satisfied, (2) the solution to the minimizing equation that is regular at the origin has no zero crossing for $0 < r < r_s$, and (3) the solution containing only the weak singularity solution at $r = r_s$ has no zero crossing for $r_s < r < a$. The criteria are easily generalized to more than one singular surface.

External mode stability

The last step in Newcomb's procedure is to test for external mode stability. To do this assume that the given m and k have been shown to be stable to Suydam's criterion and all internal modes. One then integrates the minimizing equation either from $0 < r < a$ for no singular surfaces or over the last sub-interval from $r_s < r < a$ when one or multiple singular surfaces exist. In either case the fluid contribution to the potential energy reduces to

$$\delta\hat{W}_F = f(a)\xi(a)\xi'(a) \tag{11.117}$$

Note that internal mode stability implies that there will be no zero crossings over the region of integration. Equally important it is not necessary to introduce a separate $\xi_1(r)$ and $\xi_2(r)$ since for an external mode $\xi(a) \neq 0$; in other words, one

just sets $\zeta(r) = \xi_1(r)$, integrates over the region of interest, and evaluates the boundary term given by Eq. (11.117). This is a simple numerical procedure.

Assuming that $\delta \hat{W}_F$ is known then the complete external mode potential energy is obtained directly from Eq. (11.98), which can be rewritten as

$$\delta \hat{W} = \left(\frac{F^2}{k_0^2} \frac{r\xi'}{\xi} + \frac{FF^{\dagger}}{k_0^2} + \frac{r^2 F^2 \Lambda}{m} \right)_a \xi^2(a) \tag{11.118}$$

External mode stability requires that $\delta \hat{W} > 0$.

Minimizing the search over m *and* k

A final practical point is related to the fact that a complete stability analysis requires testing all $m \geq 0$ and $-\infty < k < \infty$. Although straightforward in principle this could involve a large amount of work. The actual amount of work can, however, be dramatically reduced by exploiting the m and k dependence of $f(r)$ and $g(r)$.

Consider first internal modes for $m \neq 0$ and treat m and $\overline{k} = k/m$ as the independent wave numbers. From Eq. (11.90) it follows that $f(r)$ is independent of m and $g(r)$ contains only one term with explicit m dependence,

$$g(m, \overline{k}, r) = \overline{g}(\overline{k}, r) + m^2 r (\overline{k} B_z + B_\theta / r)^2 \tag{11.119}$$

Since the m dependent term is always stabilizing the most unstable mode corresponds to $m = 1$. Similarly, for $m = 0$, $f(r)$ is independent of k and $g(r)$ contains only one positive term with explicit k dependence,

$$g(m = 0, k, r) = \overline{g}(r) + r k^2 B_z^2 \tag{11.120}$$

In this case the most unstable mode corresponds to $k^2 \to 0$.

Consequently, when testing for internal mode stability it is necessary and sufficient to examine only $m = 1$, $-\infty < k < \infty$ and $m = 0$, $k^2 \to 0$, a significant reduction in the overall parameter space. With respect to external mode stability it can be easily shown that the same conclusions hold with the wall at infinity ($b \to \infty$). However, when the wall moves sufficiently close to the plasma the situation changes since wall stabilization is more effective for long wavelengths (i.e., small m and /or small k). In this case a more complete search is required.

Summary

Under the assumption that Suydam's criterion is satisfied, Newcomb's analysis, shows how to determine the internal and external stability of a given screw pinch profile by examining the radial structure of $\xi(r)$ as determined by the solution of the

minimizing equation. The required information can be easily obtained numerically. When the internal and external stability criteria are satisfied for the most unstable *m* and *k* values, one can then conclude that the screw pinch is MHD stable.

11.5.4 The normal mode eigenvalue equation

All the general analysis thus far presented has been based on the Energy Principle. In this subsection attention is focused on the normal mode formulation of MHD stability. The goal is to derive the normal mode eigenvalue equation and boundary conditions for the general screw pinch.

The motivations for this calculation are as follows. First, it is of interest to demonstrate the procedure for deriving eigenvalue equations starting from the normal mode equations. Second, the actual equation itself can be quite useful. Specifically, while it is difficult to obtain analytic intuition from the equation because of its complexity, it is relatively straightforward to solve the equation numerically. Lastly, there is one important analytic result that can be deduced from the equation, and that is the oscillation theorem of Goedbloed and Sakanaka (1974). This theorem, which is derived in the next subsection, proves that the eigenvalues exhibit Sturmian behavior. It thus demonstrates that the most unstable MHD mode for a given *m* and *k* is always the one whose eigenfunction has no radial nodes. The theorem also proves that the existence of highly localized, highly oscillatory modes such as arise from violation of Suydam's criterion, imply the existence of a faster growing macroscopic mode with no nodes, a much more serious instability.

The derivation of the normal mode eigenvalue equation is straightforward but does require extensive algebra. The final form of the equation is a second-order ordinary differential equation in which the eigenvalue ω^2 appears in a quite complicated way (Hain and Lust, 1958).

Formulation of the problem

The equilibrium quantities needed for the formulation are the magnetic field $\mathbf{B} = B_\theta(r)\mathbf{e}_\theta + B_z(r)\mathbf{e}_z$, the pressure $p(r)$, and the density $\rho(r)$. The desired eigenmode equation is obtained from the reduction of the generalized normal mode equations derived in Chapter 8, given by

$$-\omega^2 \rho \boldsymbol{\xi} = \frac{1}{\mu_0}(\nabla \times \mathbf{Q}) \times \mathbf{B} + \frac{1}{\mu_0}(\nabla \times \mathbf{B}) \times \mathbf{Q} - \nabla p_1$$
$$= \frac{1}{\mu_0}(\mathbf{B} \cdot \nabla \mathbf{Q} + \mathbf{Q} \cdot \nabla \mathbf{B}) - \nabla\left(p_1 + \frac{1}{\mu_0}\mathbf{B} \cdot \mathbf{Q}\right) \tag{11.121}$$

where

$$\mathbf{Q} = \nabla \times (\boldsymbol{\xi}_\perp \times \mathbf{B})$$
$$p_1 = -\boldsymbol{\xi}_\perp \cdot \nabla p - \gamma p \nabla \cdot \boldsymbol{\xi} \tag{11.122}$$

For cylindrically symmetric systems it is again convenient to decompose the vector components as follows:

$$\boldsymbol{\xi} = \xi \mathbf{e}_r + \eta \, \mathbf{e}_\eta + \xi_{||} \mathbf{b}$$
$$\mathbf{Q} = Q_r \mathbf{e}_r + Q_\eta \mathbf{e}_\eta + Q_{||} \mathbf{b}$$
$$\mathbf{e}_\eta = (B_z \mathbf{e}_\theta - B_\theta \mathbf{e}_z)/B \tag{11.123}$$
$$\mathbf{b} = (B_\theta \mathbf{e}_\theta + B_z \mathbf{e}_z)/B$$

with

$$\eta = (\xi_\theta B_z - \xi_z B_\theta)/B \qquad \xi_{||} = (\xi_\theta B_\theta + \xi_z B_z)/B$$
$$Q_\eta = (Q_\theta B_z - Q_z B_\theta)/B \qquad Q_{||} = (Q_\theta B_\theta + Q_z B_z)/B \tag{11.124}$$

As before, all quantities are Fourier analyzed with respect to θ and z. For example $\xi(r,\theta,z) = \xi(r) \exp(im\theta + ikz)$. Also appearing in the analysis are the two functions

$$F(r) = \mathbf{k} \cdot \mathbf{B} = kB_z + mB_\theta/r$$
$$G(r) = \mathbf{e}_r \cdot \mathbf{k} \times \mathbf{B} = mB_z/r - kB_\theta \tag{11.125}$$

Eliminating Q and p₁ in terms of ξ

The expansion of Eq. (11.122) leads to expressions for $\mathbf{Q}$ and p_1 in terms of the components of $\boldsymbol{\xi}$. A short calculation yields

$$Q_r = iF\xi$$
$$Q_\eta = iF\eta + \frac{1}{B}\left[B_\theta B_z' - rB_z(B_\theta/r)'\right]\xi$$
$$Q_{||} = -iG\eta - \frac{B}{r}(r\xi)' + \frac{1}{B}\left(\mu_0 p' + 2B_\theta^2/r\right)\xi \tag{11.126}$$
$$p_1 = -p'\xi - \gamma p\left[\frac{(r\xi)'}{r} + i\frac{G}{B}\eta + i\frac{F}{B}\xi_{||}\right]$$

These expressions are now to be substituted into Eq. (11.121) leading to a set of three equations and three unknowns (i.e., the three components of $\boldsymbol{\xi}$).

Eliminating η and ξ_{||} in terms of ξ

A convenient way to carry out the substitution is to separate Eq. (11.121) into its $(\mathbf{e}_r, \mathbf{e}_\eta, \mathbf{b})$ components. One first forms the dot product of Eq. (11.121) with $\mathbf{b}$. A short calculation leads to

$$\left(\frac{\gamma p}{B^2}F^2 - \omega^2\rho\right)\xi_{\parallel} + \left(\frac{\gamma pFG}{B^2}\right)\eta = \left(\frac{i\gamma pF}{rB}\right)(r\xi)' \qquad (11.127)$$

Next, form the dot product of Eq. (11.121) with $\mathbf{e}_{\eta}$. Another short calculation yields

$$\left(\frac{\gamma pFG}{B^2}\right)\xi_{\parallel} + \left(\frac{k_0^2 B^2}{\mu_0} + \frac{\gamma p}{B^2}G^2 - \omega^2\rho\right)\eta = \left[\frac{iG}{rB}\left(\gamma p + \frac{B^2}{\mu_0}\right)\right](r\xi)' + \left(\frac{2ikBB_{\theta}}{\mu_0 r}\right)\xi \qquad (11.128)$$

Equations (11.127) and (11.128) should be viewed as two simultaneous algebraic equations for $\xi_{\parallel}$ and η. The algebraic behavior is a consequence of the cylindrical symmetry of the equilibrium. After solving these equations one obtains

$$\xi_{\parallel} = -\left(\frac{i\gamma pF}{r\rho BD}\right)\left[(\omega^2 - \omega_a^2)(r\xi)' + \left(\frac{2kGB_{\theta}}{\mu_0\rho}\right)\xi\right]$$

$$\eta = -\left(\frac{i}{r\rho BD}\right)\left[G\left(\gamma p + \frac{B^2}{\mu_0}\right)(\omega^2 - \omega_h^2)(r\xi)' + \left(\frac{2kB^2 B_{\theta}}{\mu_0}\right)(\omega^2 - \omega_g^2)\xi\right] \qquad (11.129)$$

Here,

$$\omega_a^2 = F^2/\mu_0\rho$$
$$\omega_h^2 = \left[V_S^2/(V_S^2 + V_A^2)\right]\omega_a^2$$
$$\omega_g^2 = (V_S^2/V_A^2)\omega_a^2$$
$$D = (\omega^2 - \omega_f^2)(\omega^2 - \omega_s^2)$$
$$\omega_{f,s}^2 = (1/2)\left[k_0^2(V_S^2 + V_A^2)\right]\left[1 \pm \left(1 - \alpha^2\right)^{1/2}\right]$$
$$\alpha^2 = 4V_S^2\omega_a^2/\left[k_0^2\left(V_S^2 + V_A^2\right)^2\right] \qquad (11.130)$$

and $V_S^2 = \gamma p/\rho$, $V_A^2 = B^2/\mu_0\rho$, $k_0^2 = k^2 + m^2/r^2$.

The final equation

The last step in the calculation is to substitute the expressions for $\xi_{\parallel}$ and η into the $\mathbf{e}_r$ component of the normal mode equation which can be written as

$$\rho(\omega^2 - \omega_a^2)\xi = \frac{2B_{\theta}}{\mu_0 rB}\left(B_z Q_{\eta} + B_{\theta}Q_{\parallel}\right) + \frac{d}{dr}\left(p_1 + \frac{1}{\mu_0}BQ_{\parallel}\right) \qquad (11.131)$$

After a straightforward but lengthy calculation the separate terms appearing in Eq. (11.131) can be evaluated:

$$p_1 + \frac{1}{\mu_0} BQ_\parallel = -\frac{\rho\left(V_S^2 + V_A^2\right)}{r}\frac{\left(\omega^2 - \omega_a^2\right)\left(\omega^2 - \omega_h^2\right)}{\left(\omega^2 - \omega_f^2\right)\left(\omega^2 - \omega_s^2\right)}(r\xi)'$$

$$+ \frac{2}{\mu_0 r^2}\left[B_\theta^2 - kGB_\theta \frac{\left(V_S^2 + V_A^2\right)\left(\omega^2 - \omega_h^2\right)}{\left(\omega^2 - \omega_f^2\right)\left(\omega^2 - \omega_s^2\right)}\right](r\xi)$$

$$\frac{2B_\theta}{\mu_0 rB}\left(B_z Q_\eta + B_\theta Q_\parallel\right) = -\frac{2}{\mu_0 r^2}\left[B_\theta^2 - kGB_\theta \frac{\left(V_S^2 + V_A^2\right)\left(\omega^2 - \omega_h^2\right)}{\left(\omega^2 - \omega_f^2\right)\left(\omega^2 - \omega_s^2\right)}\right](r\xi)'$$

$$-\frac{1}{\mu_0 r^3}\left[r^3\left(B_\theta^2/r^2\right)' - 4k^2 B_\theta^2 V_A^2 \frac{\left(\omega^2 - \omega_g^2\right)}{\left(\omega^2 - \omega_f^2\right)\left(\omega^2 - \omega_s^2\right)}\right](r\xi)$$

$$\tag{11.132}$$

These complicated expressions are substituted into Eq. (11.131). A straightforward calculation leads to

$$\frac{d}{dr}\left(A\frac{dU}{dr}\right) - CU = 0 \tag{11.133}$$

where $U = r\xi$ and

$$A(r) = \frac{\rho\left(V_S^2 + V_A^2\right)}{r}\frac{\left(\omega^2 - \omega_a^2\right)\left(\omega^2 - \omega_h^2\right)}{\left(\omega^2 - \omega_f^2\right)\left(\omega^2 - \omega_s^2\right)}$$

$$C(r) = -\frac{\rho}{r}\left(\omega^2 - \omega_a^2\right) + \frac{4k^2 B_\theta^2 V_A^2}{\mu_0 r^3}\frac{\left(\omega^2 - \omega_g^2\right)}{\left(\omega^2 - \omega_f^2\right)\left(\omega^2 - \omega_s^2\right)} \tag{11.134}$$

$$+ \frac{d}{dr}\left[\frac{B_\theta^2}{\mu_0 r^2} - \frac{2kGB_\theta}{\mu_0 r^2}\frac{\left(V_S^2 + V_A^2\right)\left(\omega^2 - \omega_h^2\right)}{\left(\omega^2 - \omega_f^2\right)\left(\omega^2 - \omega_s^2\right)}\right]$$

This is the desired form of the eigenvalue equation for a general screw pinch (Hain and Lust, 1958). It is a second-order ordinary differential equation with quite complicated coefficients $A(r)$, $C(r)$. Observe that the eigenvalue ω^2 appears in many terms, also in complicated ways.

Boundary conditions

To complete the formulation of the problem boundary conditions are needed. The first boundary condition, valid for both internal and external modes, requires regularity at the origin. A short calculation shows that near $r = 0$ the solutions behave like $U \propto r^{\pm m}$. Therefore, one practical way to implement regularity

numerically when determining the eigenvalues, for instance by a shooting procedure, is to start integrating the equation a short distance $\delta \ll a$ from the origin, setting $U(\delta) = \delta^m$ and $U'(\delta) = m\delta^{m-1}$. This automatically selects the regular branch of the general solution.

A second boundary condition is needed at the plasma surface $r = a$. For internal modes this is a simple condition. Since the boundary does not move for an internal mode this corresponds to requiring

$$U(a) = 0 \tag{11.135}$$

For external modes the boundary condition is more difficult. For this case the two jump conditions across the interface must be simultaneously satisfied, which translates into a single boundary condition determined as follows. Assume for simplicity that the current density at the plasma edge satisfies the realistic condition $\mathbf{J}(a) = 0$. The $\nabla \cdot \mathbf{B} = 0$ and pressure balance jump conditions can then be written as

$$\begin{aligned} [\![\mathbf{e}_r \cdot \mathbf{B}_1]\!]_a &= 0 \\ [\![\mathbf{B} \cdot \mathbf{B}_1]\!]_a &= 0 \end{aligned} \tag{11.136}$$

Consider now the fields on the vacuum side of the boundary. From the analysis presented in connection with Eq. (11.91) one easily can show that

$$\begin{aligned} \mathbf{e}_r \cdot \hat{\mathbf{B}}_1 \Big|_a &= A_0 |k| K'_a \big(1 - K'_b I'_a / I'_b K'_a \big) \\ \hat{\mathbf{B}} \cdot \hat{\mathbf{B}}_1 \Big|_a &= i A_0 F(a) K_a \big(1 - K'_b I_a / I'_b K_a \big) \end{aligned} \tag{11.137}$$

where $F_a = F(a)$, $K_\rho = K_m(\zeta_\rho)$, $I_\rho = I_m(\zeta_\rho)$, $\zeta_\rho = |k|\rho$, and A_0 is an arbitrary (and at this point) unknown constant.

The same quantities must next be evaluated on the plasma side of the boundary. The normal component of $\mathbf{B}_1 \equiv \mathbf{Q}$ is directly obtained from Eq. (11.126),

$$\mathbf{e}_r \cdot \mathbf{Q} \Big|_a = i F(a) \xi(a) \tag{11.138}$$

The parallel component of $\mathbf{Q}$ requires a short calculation. One starts with $Q_\parallel$ given by Eq. (11.126), substitutes η from Eq. (11.129), and makes use of the $\mathbf{J} = 0$ edge relations, $p'(a) = 0$, $B'_z(a) = 0$, $B'_\theta(a) = -B_\theta(a)/a$. A straightforward calculation yields

$$\mathbf{B} \cdot \mathbf{Q} \Big|_a = - \left[\frac{B^2}{r} \frac{\omega^2 - \omega_a^2}{\omega^2 - k_0^2 V_A^2} \right]_a (r\xi)'_a + \left[\frac{2}{r} \frac{\omega^2 B_\theta^2 - V_A^2 F(m B_\theta / r)}{\omega^2 - k_0^2 V_A^2} \right]_a \xi(a) \tag{11.139}$$

The required boundary condition is calculated by equating the ratio of the jump conditions in each region: $\big[\hat{\mathbf{B}} \cdot \hat{\mathbf{B}}_1 / \mathbf{e}_r \cdot \hat{\mathbf{B}}_1 \big]_a = [\mathbf{B} \cdot \mathbf{Q} / \mathbf{e}_r \cdot \mathbf{Q}]_a$. This operation

eliminates the unknown constant A_0 from the vacuum region. After transforming dependent variables from ξ to U one arrives at the desired boundary condition

$$
\begin{aligned}
&c_1 a U'(a) - c_2 U(a) = 0 \\
&\quad c_1 = \left[B^2 (\omega^2 - \omega_a^2) \right]_a \\
&\quad c_2 = \left[2B_\theta^2 - r^2 F^2 \Lambda / m \right]_a \omega^2 - \left[2mB_\theta F / r - k_0^2 r^2 F^2 \Lambda / m \right]_a
\end{aligned}
\tag{11.140}
$$

where Λ is the wall stabilization factor defined in Eq. (11.96). Note that the eigenvalue ω^2 appears in the boundary condition.

Equation (11.133), combined with the regularity condition at the origin and either the internal boundary mode condition Eq. (11.135) or the external boundary mode condition Eq. (11.140) represent the self-consistent formulation of the normal mode eigenvalue problem. As previously stated, the formulation is sufficiently complex that it is difficult to obtain much analytic insight. Still, it is in a very convenient form for numerical implementation.

11.5.5 The oscillation theorem

An important result concerning the stability of a general screw pinch has been derived by Goedbloed and Sakanaka (1974). They demonstrate the existence of an oscillation theorem, analogous to Sturm's well-known oscillation theorem, which relates the number of radial nodes in the eigenfunction to the relative size of the eigenvalue. Specifically, they show that for fixed m and k as the number of internal radial nodes l in a sequence of unstable eigenfunctions monotonically decreases, the corresponding eigenvalue ω_l^2 also decreases (i.e., becomes more negative). In other words, the most unstable eigenfunction is always the one with zero internal radial nodes. Their proof is elegant and non-trivial since the eigenvalue ω^2 appears in a very complicated way in the MHD stability equation (i.e., Eq. (11.133)) as compared to a classic Sturm–Liouville system. The derivation and interpretation of the MHD oscillation theorem is presented below.

The basic reason why an oscillation theorem exists is directly tied to the self-adjoint property of $\mathbf{F}(\boldsymbol{\xi})$. The analysis proceeds by considering the general 3-D normal mode formulation of MHD stability with attention focused on the unstable part of the spectrum; discrete eigenmodes with $\omega^2 < 0$. After several clever relations are derived that make use of the self-adjointness of $\mathbf{F}(\boldsymbol{\xi})$, the cylindrical symmetry assumption is introduced, from which one obtains the oscillation theorem. The task that motivates the analysis is the determination of which radial direction (i.e., inward or outward) the node of an unstable trial function moves as the value of ω^2 is changed.

The 3-D analysis

The starting point of the derivation is the general 3-D MHD stability equation: $-\omega^2 \rho \boldsymbol{\xi} = \mathbf{F}(\boldsymbol{\xi})$. Two independent trial functions $\boldsymbol{\xi}$ and $\boldsymbol{\eta}$, each satisfying regularity at the origin, but not $\mathbf{n} \cdot \boldsymbol{\xi} = 0$ or $\mathbf{n} \cdot \boldsymbol{\eta} = 0$ on the plasma surface, are substituted into the following integrals, a step motivated by the analysis in Chapter 8 (i.e., Eq. (8.25)):

$$\frac{1}{2} \int \boldsymbol{\eta} \cdot \mathbf{F}(\xi) \, d\mathbf{r} = -\delta W_F(\boldsymbol{\eta}, \boldsymbol{\xi}) - \frac{1}{2} \int (\mathbf{n} \cdot \boldsymbol{\eta}) \left[\frac{1}{\mu_0} \mathbf{B} \cdot \mathbf{Q}(\xi) + p_1(\xi) \right] dS$$

$$\frac{1}{2} \int \boldsymbol{\xi} \cdot \mathbf{F}(\eta) \, d\mathbf{r} = -\delta W_F(\boldsymbol{\xi}, \boldsymbol{\eta}) - \frac{1}{2} \int (\mathbf{n} \cdot \boldsymbol{\xi}) \left[\frac{1}{\mu_0} \mathbf{B} \cdot \mathbf{Q}(\eta) + p_1(\eta) \right] dS$$

$$(11.141)$$

Here, it is important to keep in mind that the integration volume and surface area correspond to an arbitrary internal flux surface, not in general the plasma boundary. The relations derived in Chapter 8 can easily be shown to apply to this case since all that is required is the fact that $\mathbf{n} \cdot \mathbf{B} = 0$ on the integration surface. Also, the analysis is simplified by treating $\boldsymbol{\xi}$ and $\boldsymbol{\eta}$ as real quantities.

The next step is to subtract these integrals, making use of $\delta W_F(\boldsymbol{\eta}, \boldsymbol{\xi}) = \delta W_F(\boldsymbol{\xi}, \boldsymbol{\eta})$ since they are self-adjoint by construction. The result is

$$\int [\boldsymbol{\eta} \cdot \mathbf{F}(\xi) - \boldsymbol{\xi} \cdot \mathbf{F}(\eta)] d\mathbf{r} = -\int [(\mathbf{n} \cdot \boldsymbol{\eta}) \hat{p}_1(\xi) - (\mathbf{n} \cdot \boldsymbol{\xi}) \hat{p}_1(\eta)] \, dS \quad (11.142)$$

where $\hat{p}_1 = p_1 + \mathbf{B} \cdot \mathbf{Q}/\mu_0$.

Introducing cylindrical symmetry

At this point it is convenient to introduce the cylindrical symmetry assumption. The volume integral becomes a 1-D integral and the surface integral becomes an evaluation on S. The region of integration is $0 \leq r \leq r_S$ with $r = r_S$ representing the boundary flux surface of interest. Equation (11.142) reduces to

$$\int_0^{r_S} [\boldsymbol{\eta} \cdot \mathbf{F}(\xi) - \boldsymbol{\xi} \cdot \mathbf{F}(\eta)] r dr = -r_S \left[\eta \hat{p}_1(\xi) - \xi \hat{p}_1(\eta) \right]_{r_S} \quad (11.143)$$

Here $\xi = \mathbf{e}_r \cdot \boldsymbol{\xi}$ and $\eta = \mathbf{e}_r \cdot \boldsymbol{\eta}$.

One now has to make clever choices for ξ and η to prove the oscillation theorem. To do this, choose an arbitrary negative value of $\omega^2 = \omega_0^2 < 0$, which in general will not be an eigenvalue. The basic differential equation (i.e., Eq. (11.133) is then integrated from 0 to a assuming that the choice for ω_0^2 leads to a solution with N radial nodes. A typical solution is illustrated in Fig. 11.23. A clever choice for r_S assumes that it coincides with one of the radial nodes, for instance r_n: $r_S = r_n$. This
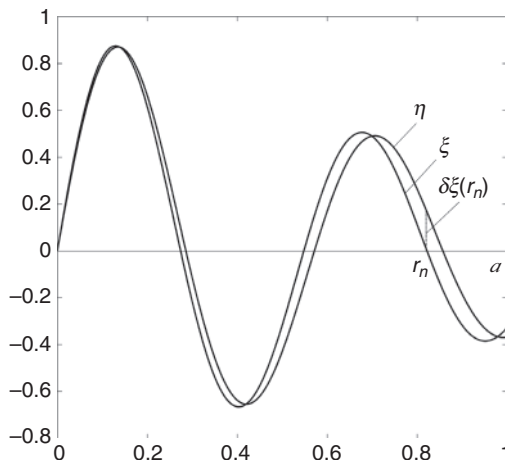
Figure 11.23   Solution for ξ and η used in the derivation of the oscillation theorem.

solution is defined as $\xi(r)$ and satisfies $\xi(r_n) = 0$. Also, since ω_0^2 is not an eigenvalue then in general $\xi(a) \neq 0$.

Consider next the choice for $\eta(r)$. Imagine repeating the previous calculation for a slightly different value of ω^2. Specifically choose $\omega^2 = \omega_0^2 + \delta\omega^2$ with $\delta\omega^2 \ll \omega_0^2$. The resulting solution is defined as $\eta(r)$ and will be only slightly different than $\xi(r)$ when $\delta\omega^2$ is small. In other words, $\eta(r) = \xi(r) + \delta\xi(r)$ with $\delta\xi(r) \ll \xi(r)$. Note that since ω^2 has changed slightly, then the location of the nth node will also have shifted slightly. The direction of this shift can be determined by calculating the value of $\delta\xi(r_n)$. From Fig. 11.23 it follows that, when $\delta\xi(r_n) > 0$, the node has shifted outward. Conversely, when $\delta\xi(r_n) < 0$, the node has shifted inward. The opposite signs apply for node r_{n-1}.

The basic question to be addressed, and whose answer forms the foundation of the oscillation theorem, is whether the nodal shift in is always outwards, always inwards, or can go in either direction, as ω^2 is changed monotonically; that is, mathematically one needs to determine a relation between $\delta\xi(r_n)$ and $\delta\omega^2$.

The relation between $\delta\xi(r_n)$ and $\delta\omega^2$

The answer to the question is obtained by evaluating the various terms in Eq. (11.143). The left-hand side is evaluated by making use of the fact that $\xi(r)$ and $\eta(r) = \xi(r) + \delta\xi(r)$ satisfy

$$-\omega_0^2 \rho\boldsymbol{\xi} = \mathbf{F}(\boldsymbol{\xi})$$
$$-\left(\omega_0^2 + \delta\omega^2\right)\rho(\boldsymbol{\xi} + \delta\boldsymbol{\xi}) = \mathbf{F}(\boldsymbol{\eta})$$

(11.144)

Now, form the dot product of the first equation with $\boldsymbol{\eta}$ and the second with $\boldsymbol{\xi}$ and integrate from 0 to r_S. The resulting equations are subtracted with the first non-vanishing term given by

$$\int_0^{r_S} [\boldsymbol{\eta} \cdot \mathbf{F}(\boldsymbol{\xi}) - \boldsymbol{\xi} \cdot \mathbf{F}(\boldsymbol{\eta})] r dr \approx \delta\omega^2 \int_0^{r_n} \rho(\xi)^2 r dr \qquad (11.145)$$

The left-hand side, which coincides with the left-hand side of Eq. (11.143), is evaluated by substituting the expressions for $\hat{p}_1$ from Eq. (11.132). A short calculation shows that the first non-vanishing term that survives the cancellation can be written as

$$-r_S \Big[\eta\hat{p}_1(\xi) - \xi\hat{p}_1(\eta) \Big]_{r_S} = \Big[r^2 A \Big(\eta\,\xi' - \xi\,\eta' \Big) \Big]_{r_n}$$

$$\approx \Big[r^2 A \xi' \Big]_{r_n} \delta\xi(r_n) \qquad (11.146)$$

where $A(r)$ is defined by Eq. (11.134). Equating the terms in Eqs. (11.145) and (11.146) yields the desired relation between $\delta\xi(r_n)$ and $\delta\omega^2$,

$$\delta\xi(r_n) = \frac{\displaystyle\int_0^{r_n} \rho^2(\xi)^2 r dr}{[r^2 A \xi']_{r_n}} \, \delta\omega^2 \qquad (11.147)$$

The oscillation theorem

The oscillation theorem can now be easily derived by examining Eq. (11.147). Observe that the numerator is positive. Similarly, when $\omega^2 < 0$ the function $A(r)$ is also positive. Lastly for the node r_n illustrated in Fig. 11.23 one sees that $\xi'(r_n)$ is negative. Consequently, when $\delta\omega^2 < 0$ then $\delta\xi(r_n) > 0$; the node always moves outward. The same conclusion applies to the node at r_{n-1}. For this case $\xi'(r_n)$ becomes positive and $\delta\xi(r_n) < 0$, again leading to an outward movement of the node.

Continuous application of this result for a sequence of negative $\delta\omega^2$'s leads to the oscillation theorem. If an unstable eigenfunction exists with n radial nodes then as ω^2 is continuously decreased (corresponding to increased instability), every time $\xi(a)$ happens to cross zero, the result is an unstable eigenfunction with $n-1$, $n-2, n-3, \ldots, 0$ radial nodes. In all cases the zero node mode has the maximum growth rate. This is the main conclusion from the oscillation theorem.

As previously stated the oscillation theorem has important implications with regard to Suydam's criterion. When the criterion is violated the oscillation theorem guarantees the existence of a zero node mode with maximum growth rate. The oscillation theorem also shows that $\omega^2 = 0$ is a point of accumulation from the
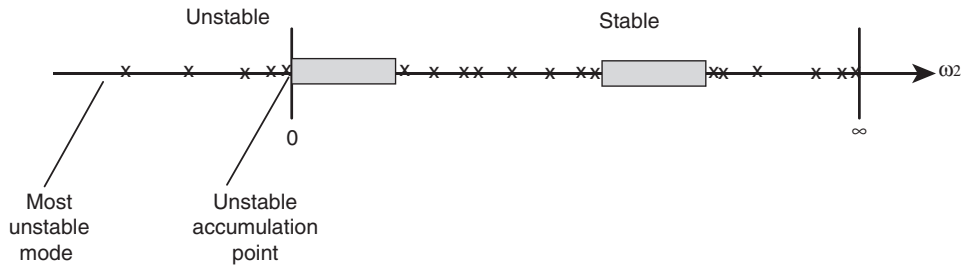
Figure 11.24 Illustration of an accumulation point at $\omega^2 = 0$ from the unstable side of the spectrum when Suydam's criterion is violated.

unstable side of the spectrum when Suydam's criterion is violated as shown in Fig. 11.24. An elegant and complete analysis of the oscillation theorem and its implication on the stable as well as unstable side of the spectrum has been given by Goedbloed and Poedts (2004).

An important practical consequence of the oscillation theorem is that when carrying out numerical studies of MHD stability of a cylindrical screw pinch, one need only focus on the eigenfunction with zero nodes (for the given m and k) to determine the most unstable mode.

11.5.6 The resistive wall mode

The final general theoretical result for the screw pinch concerns the resistive wall mode (Goedbloed *et al.*, 1972). This is a potentially very serious external MHD instability, important in both RFPs and tokamaks. If the mode is excited it often leads to major disruptions. Understanding the resistive wall mode in its simplest form in a cylindrical geometry is the goal of the present subsection.

The mode arises as follows. In fusion-grade experiments the first wall surrounding the plasma, often the vacuum chamber, is metallic. Thus, to a certain extent the wall behaves approximately like a perfect conductor. If so, this leads to a large improvement in MHD stability. The physics is straightforward. As a cylindrical plasma deforms due to an MHD perturbation, parts of the cross section move closer to the wall while other parts move further away. For the closer parts the poloidal field trapped between the surface and the wall increases since the trapped flux must remain constant (i.e., both the plasma and wall are perfect conductors). The resulting increased magnetic tension pushes back on the plasma, attempting to restore it to its original circular shape. This is clearly the wall stabilization effect. A similar argument holds for the parts of the surface that are further away.

Now, in practice the first wall is obviously not a perfect conductor. In fact it is often deliberately designed to have a substantial resistivity (compared to a thick

copper shell). This allows externally applied vertical fields to penetrate the chamber sufficiently rapidly to provide effective feedback control of the equilibrium position of the plasma. Also, with a higher resistivity smaller currents are induced in the first wall during transients, alleviating power supply requirements.

The problem that arises with a resistive wall with respect to stability is that over a period of time the compressed and expanded portions of the poloidal field diffuse through the wall. In fact, after several "resistive wall diffusion times" the effect of the wall vanishes and the stability boundaries return to those of the "no-wall" situation. The resulting decrease in MHD stability β limits is important in tokamaks since the no-wall values can be only marginally satisfactory for fusion energy applications. In the RFP the situation is even more serious since external modes are always unstable without a perfectly conducting wall; the no-wall limit is $\beta = 0$.

Avoiding the resistive wall mode requires feedback stabilization. This can be accomplished if the wall is close enough that the plasma would be stable if the wall was perfectly conducting. The reason is that the characteristic resistive wall growth time slows down to the order of the resistive wall diffusion time which is long enough so that practical feedback circuits can be constructed. If the perfectly conducting wall is not close enough to provide stability, then the mode grows with an ideal MHD growth rate which is too fast for practical feedback stabilization.

In the discussion below, the growth rate of the resistive wall mode is calculated and related to the ideal MHD stability boundaries with and without a perfectly conducting wall. This is the basic resistive wall mode in its simplest form. It should be noted that the resistive wall MHD stability limits are favorably affected by equilibrium plasma flows and plasma kinetic effects. While these effects improve the situation, they do not completely and reliably eliminate the problem in all practical situations and feedback will likely still be required. Flow and kinetic effects are advanced topics that will not be covered in this textbook.

The analysis is carried out in four steps: (1) reference cases are established for ideal MHD stability with and without a perfectly conducting wall; (2) magnetic fields are calculated in the vacuum regions and within the resistive wall itself; (3) jump conditions are derived that connect the fields across the resistive wall; and (4) the resulting set of equations is solved yielding the dispersion relation for the resistive wall mode in a general cylindrical screw pinch.

The reference cases

The reference cases needed for the analysis correspond to the values of δW for external modes with and without a perfectly conducting wall. The basic results have already been derived and are given by Eqs. (11.98) and (11.118), repeated here for convenience:

$$\frac{\delta W}{2\pi^2 R_0/\mu_0} = \int_0^a \left(f\xi'^2 + g\xi^2 \right) dr + \left(\frac{FF^\dagger}{k_0^2} + \frac{r^2 F^2 \Lambda}{m} \right)_a \xi^2(a)$$

$$= \left(\frac{F^2}{k_0^2} \frac{r\xi'}{\xi} + \frac{FF^\dagger}{k_0^2} + \frac{r^2 F^2 \Lambda}{m} \right)_a \xi^2(a) \tag{11.148}$$

Recall that the second form is obtained by assuming that a solution to the minimizing equation for ξ has been obtained and substituted into the integral in the first form. Also, keep in mind that the value of $(r\xi'/\xi)_a$ depends only on the plasma profiles and not the location of the conducting wall.

The two required reference values differ only because of the value of Λ and can be written as

$$\frac{\delta W_\infty}{2\pi^2 R_0/\mu_0} = \left(\frac{F^2}{k_0^2} \frac{r\xi'}{\xi} + \frac{FF^\dagger}{k_0^2} + \frac{r^2 F^2 \Lambda_\infty}{m} \right)_a \xi^2(a)$$

$$\frac{\delta W_b}{2\pi^2 R_0/\mu_0} = \left(\frac{F^2}{k_0^2} \frac{r\xi'}{\xi} + \frac{FF^\dagger}{k_0^2} + \frac{r^2 F^2 \Lambda_b}{m} \right)_a \xi^2(a) \tag{11.149}$$

where

$$\Lambda_\infty = -\frac{m K_a}{|ka| K_a'} \approx 1$$

$$\Lambda_b = \Lambda_\infty \left[\frac{1 - (K_b' I_a)/(I_b' K_a)}{1 - (K_b' I_a')/(I_b' K_a')} \right] \approx \frac{1 + (a/b)^{2m}}{1 - (a/b)^{2m}} \tag{11.150}$$

The approximate formulae are valid when $kb \sim ka \ll 1$. Clearly $\Lambda_b > \Lambda_\infty$. The interesting physical regime occurs when

$$\delta W_\infty < 0 < \delta W_b \tag{11.151}$$

That is, without a wall the plasma is unstable to an external MHD mode while with a wall the mode is stabilized.

Using the Energy Principle δW rather than the full eigenmode solutions is useful for the resistive wall analysis because the expected growth rates are anticipated to be very slow, on the order of the resistive wall diffusion time. Therefore, for the resistive wall analysis one can set $\omega^2 \approx 0$ in the full eigenmode equation which then reduces to the marginal stability minimizing equation $(f\xi')' - g\xi = 0$. The conclusion is that the value of $(r\xi'/\xi)_a$ appearing in the resistive wall analysis is identical to the value in both reference cases.
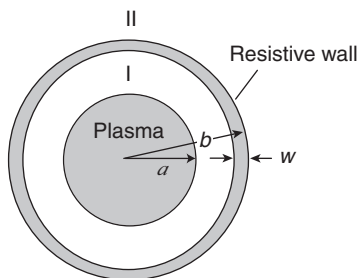
Figure 11.25   Geometry for the resistive wall stability analysis.

What remains is to calculate the exterior magnetic fields which are modified by the presence of the resistive wall.

The vacuum and wall solutions

The perturbed fields exterior to plasma require a three region solution as illustrated in Fig. 11.25. In the two vacuum regions the fields are again expressed in terms of potentials containing modified Bessel functions: $\hat{\mathbf{B}}_I = \nabla V_I$, $\hat{\mathbf{B}}_{II} = \nabla V_{II}$,

$$V_I = \left(A_0 K_\rho + A_1 I_\rho\right)\exp[\omega_i t + i(m\theta + kz)]$$
$$V_{II} = A_2 K_\rho \exp[\omega_i t + i(m\theta + kz)]$$

(11.152)

As before $K_\rho = K_m(\zeta_\rho)$, $I_\rho = I_m(\zeta_\rho)$, $\zeta_\rho = |k|\rho$. The A_j are unknown coefficients to be calculated from the yet to be determined matching conditions. The time dependence has been explicitly shown with $\omega = i\omega_i$ in anticipation of the fact that the growth rate will turn out to correspond to a purely growing mode. Observe also that V_{II} has only a K_ρ contribution since regularity requires that $V_{II} \to 0$ as $r \to \infty$.

Consider next the magnetic field within the resistive wall which is determined from Faraday's law, after substituting $\hat{\mathbf{E}}_1 = \eta \hat{\mathbf{J}}_1 = (\eta/\mu_0)\nabla \times \hat{\mathbf{B}}_w$ with η the resistivity of the wall. Using the fact that $\nabla \cdot \hat{\mathbf{B}}_w = 0$ one obtains the standard magnetic diffusion equation

$$\frac{\partial \hat{\mathbf{B}}_w}{\partial t} = \frac{\eta}{\mu_0}\nabla^2 \hat{\mathbf{B}}_w$$

(11.153)

The solution to Eq. (11.153) is not very complicated but does require some thought. The key point is to assume that $w \ll b$, corresponding to the "thin wall" approximation. This leads to the following simplifications: (1) Only the radial component $\hat{B}_{wr}$ is required for the analysis. (2) The geometry becomes slab-like with the introduction of a local radial coordinate x: $r = b + x$ with $0 \le x \le w$. (3) For a thin wall there is rapid radial variation over the narrow distance in x. The variation over θ and z is much slower implying that $\nabla^2 \approx \partial^2/\partial x^2$. (4) The radial magnetic field $\hat{B}_{wr}$ can be Fourier analyzed: $\hat{B}_{wr} = \hat{B}_{wr}(x)\exp[\omega_i t + i(m\theta + kz)]$.

(5) The typical magnitude of ω_i corresponds to the inverse wall diffusion time: $\omega_i \sim \eta/\mu_0 b w$.

Formally the analysis is carried out by introducing the thin wall expansion parameter $\delta = w/b \ll 1$. The various terms appearing in the analysis are ordered as follows:

$$\frac{1}{r^2}\frac{\partial^2}{\partial\theta^2} \sim \frac{\partial^2}{\partial z^2} \sim \delta\frac{\mu_0\omega_i}{\eta} \sim \delta^2\frac{\partial^2}{\partial x^2} \tag{11.154}$$

Under these conditions only the radial component of Eq. (11.153) is required, which reduces to

$$\frac{\partial^2\hat{B}_{wr}}{\partial x^2} - \frac{\mu_0\omega_i}{\eta}\hat{B}_{wr} = 0 \tag{11.155}$$

Furthermore, for this equation to be self-consistent $\hat{B}_{wr}$ must be ordered such that

$$\hat{B}_{wr} = \hat{B}_{r0} + \hat{B}_{r1} + \cdots \tag{11.156}$$

with $\hat{B}_{r1}/\hat{B}_{r0} \sim \delta$ and $\hat{B}_{r0} = \text{constant}$.

The wall solution is obtained by substituting Eq. (11.156) into Eq. (11.155). The leading- and first-order equations are given by

$$\begin{aligned} \frac{\partial^2\hat{B}_{r0}}{\partial x^2} &= 0 \\ \frac{\partial^2\hat{B}_{r1}}{\partial x^2} &= \frac{\mu_0\omega_i}{\eta}\hat{B}_{r0} \end{aligned} \tag{11.157}$$

The solutions can be written as

$$\begin{aligned} \hat{B}_{r0} &= B_{r0} = \text{constant} \\ \hat{B}_{r1} &= B_{r0}\left(\frac{\mu_0\omega_i}{2\eta}x^2\right) + B_{r1}\left(\frac{x}{w}\right) \end{aligned} \tag{11.158}$$

where B_{r0} and B_{r1} are unknown constants of zeroth- and first-order respectively. Note that $\mu_0\omega_i x^2/\eta \sim \delta$ in the thin wall approximation. The complete solution for $\hat{B}_{wr}$ has the form

$$\hat{B}_{wr} \approx \hat{B}_{r0} + \hat{B}_{r1} = B_{r0}\left(1 + \frac{\mu_0\omega_i}{2\eta}x^2\right) + B_{r1}\left(\frac{x}{w}\right) \tag{11.159}$$

The solutions in all three regions have now been specified in terms of five unknown constants A_0, A_1, A_2, B_{r0}, B_{r1}. These constants are determined by appropriate matching conditions.

The jump conditions across the wall

There are four boundary conditions across the resistive wall. These conditions can be reduced to a simple set of jump conditions relating the potential functions $\hat{V}_I$ to $\hat{V}_{II}$ at $r = b$.

To begin note that although the wall is thin, it still has a finite thickness. Therefore there are no surface currents on either surface of the wall. The implication is that both the normal and tangential components of the wall magnetic field must be continuous with the corresponding adjacent vacuum fields on each wall surface. Continuity of the normal component of magnetic field requires

$$\left.\frac{\partial \hat{V}_I}{\partial r}\right|_{b^-} = \left.\hat{B}_{wr}\right|_{x=0} \qquad \left.\frac{\partial \hat{V}_{II}}{\partial r}\right|_{b^+} = \left.\hat{B}_{wr}\right|_{x=w} \tag{11.160}$$

To evaluate continuity of the tangential magnetic field observe that the condition $\nabla \cdot \mathbf{B} = 0$ within the wall implies that $i\mathbf{k} \cdot \hat{\mathbf{B}}_w = -\partial \hat{B}_{wr}/\partial x$ with $\mathbf{k} = (m/b)\mathbf{e}_\theta + k\mathbf{e}_z$. Similarly, in the vacuum regions $i\mathbf{k} \cdot \hat{\mathbf{B}}_1 = -k_b^2 \hat{V}$, where $k_b^2 = k^2 + m^2/b^2$. Thus continuity of the tangential fields requires

$$\left.\hat{V}_I\right|_{b^-} = \left.\frac{1}{k_b^2}\frac{\partial \hat{B}_{wr}}{\partial x}\right|_{x=0} \qquad \left.\hat{V}_{II}\right|_{b^+} = \left.\frac{1}{k_b^2}\frac{\partial \hat{B}_{wr}}{\partial x}\right|_{x=w} \tag{11.161}$$

After a short calculation the constants $\hat{B}_{r0}$ and $\hat{B}_{r1}$ can be eliminated from Eqs. (11.160) and (11.161) resulting in the following set of jump conditions for the vacuum potential functions. Each condition contains the first non-vanishing contribution in the w/b expansion:

$$\left.\frac{\partial \hat{V}_I}{\partial r}\right|_{b^-} = \left.\frac{\partial \hat{V}_{II}}{\partial r}\right|_{b^+}$$

$$\left.\hat{V}_I\right|_{b^-} = \left.\hat{V}_{II}\right|_{b^+} - \left(\frac{\mu_0 \omega_i w}{\eta k_b^2}\right)\left.\frac{\partial \hat{V}_{II}}{\partial r}\right|_{b^+} \tag{11.162}$$

In terms of the coefficients A_j these conditions can be written as

$$A_0 K_b' + A_1 I_b' - A_2 K_b' = 0$$

$$A_0 K_b + A_1 I_b - A_2 \left(K_b - \frac{\mu_0 \omega_i w |k|}{\eta k_0^2} K_b'\right) = 0 \tag{11.163}$$

Equation (11.163) should be viewed as two linear algebraic equations for the two unknown coefficients A_1, A_2 in terms of the third coefficient A_0. Solving these equations yields

$$\Delta A_1 = -vK_b'A_0$$
$$\Delta A_2 = \left(I_bK_b' - K_bI_b'\right)A_0$$
$$v = \left(\mu_0 \left|k\right| w/\eta k_b^2\right)\omega_i$$
$$\Delta = I_bK_b' - K_bI_b' + vK_b'I_b'$$

$$(11.164)$$

Here v is a normalized form of the growth rate.

The resistive wall dispersion relation

The required information from the exterior region is now available to determine the dispersion relation, which is obtained by matching the two jump conditions across the plasma surface:

$$[\![B_{1r}]\!]_a = 0$$
$$[\![\mathbf{B} \cdot \mathbf{B}_1]\!]_a = 0$$

$$(11.165)$$

This calculation can be conveniently carried out by dividing the jump conditions by each other; that is, the dispersion relation is determined by setting

$$\left[\frac{\mathbf{B} \cdot \mathbf{Q}}{Q_r}\right]_a = \left[\frac{\hat{\mathbf{B}} \cdot \hat{\mathbf{B}}_1}{\hat{B}_{1r}}\right]_a$$

$$(11.166)$$

After eliminating A_1 by means of Eq. (11.164), one finds that the right-hand side can be written as

$$\left[\frac{\hat{\mathbf{B}} \cdot \hat{\mathbf{B}}_1}{\hat{B}_{1r}}\right]_a = \frac{iF_a}{|k|}\left(\frac{\Delta K_a - vI_aK_b'^2}{\Delta K_a' - vI_a'K_b'^2}\right)$$

$$(11.167)$$

where $F_a = F(a)$. Similarly, the left-hand side can be evaluated by using the general normal mode relations given by Eqs. (11.126) and (11.132) after setting $\omega^2 = 0$,

$$\left[\frac{\mathbf{B} \cdot \mathbf{Q}}{Q_r}\right]_a = \frac{i}{aF_a}\left[\frac{F^2}{k_0^2}\frac{r\xi'}{\xi} + \frac{FF^\dagger}{k_0^2}\right]_a$$

$$(11.168)$$

The dispersion relation is now obtained by equating Eq. (11.167) to Eq. (11.168) and solving for v. After untangling the notation and making use of the reference values of δW one finds

$$\omega_i\tau_w = -\frac{\delta W_\infty}{\delta W_b}$$

$$(11.169)$$

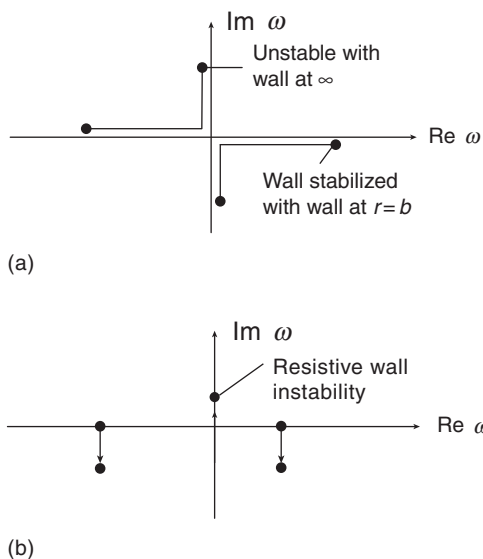Here, τ_w is the resistive wall diffusion time

Figure 11.26   Spectral behavior of resistive wall instabilities: (a) ideal wall stabilization of a mode that is unstable with the wall at infinity; (b) growth of a resistive wall mode from the origin $\omega^2 = 0$.

$$\tau_w = -\frac{\mu_0 wb}{\eta} g$$

$$g = \frac{\left|k\right| K'_b}{k_b^2 b K_b} \left(\frac{1 - I'_a K'_b / I'_b K'_a}{1 - I_b K'_b / I'_b K_b}\right) \approx \frac{1}{2m} \left[1 - \left(\frac{a}{b}\right)^{2m}\right] \tag{11.170}$$

The geometry factor $g \sim 1$ with the approximate value corresponding to $kb \ll 1$.

Discussion

There are a number of points to observe from the remarkably simple dispersion relation given by Eq. (11.169). First, the eigenfrequency is real indicating pure growth or decay depending upon the sign of $\delta W_\infty / \delta W_b$. Second, as assumed, ω_i has a characteristic growth (or decay) time of order $1/\tau_w$. Third, in the interesting case which is unstable with the wall at $r = \infty$ (i.e., $\delta W_\infty < 0$) but is stabilized with a perfectly conducting wall at $r = b$ (i.e., $\delta W_b > 0$) then $\omega_i > 0$; the presence of a resistive wall introduces a new slowly growing mode into the system so that the stability boundary reverts back to the one with the wall at infinity. Both δW_∞ and δW_b must be positive for stability.

   The spectral picture is illustrated in Fig. 11.26. In Fig. 11.26a the trajectory of an initially unstable MHD mode is traced in the complex ω plane as a perfectly conducting wall is moved inward from infinity. Since ω^2 is real for an ideal wall,

the roots must lie on either the real or imaginary axis. In Fig. 11.26b the roots are traced as the wall at $r = b$ is transformed from perfectly conducting to resistive. Although not proven here, it can be shown that the ideal wall stabilized roots become slightly damped. The resistive wall instability corresponds to the development of a new mode growing out of the origin $\omega^2 = 0$.

To conclude, the resistive wall mode represents a serious MHD instability, often leading to major disruptions. It would be highly desirable for fusion applications to have a configuration that is MHD stable at sufficiently high β with the wall at infinity, thereby avoiding the resistive wall mode. If this is not possible then some form of feedback would be required. Alternatively, one could depend on plasma rotation and/or kinetic effects to stabilize the mode, but this requires highly reliable plasma performance over narrow windows of operation which has not been that easy to achieve experimentally, at least up until the present time.

11.6 The "straight" tokamak

The stage has now been set to apply the general screw pinch analysis to modern fusion concepts. The first such concept is the "straight" tokamak. In this configuration the tokamak is straightened out into a cylindrical column of length $2\pi R_0$ with the fields satisfying the tokamak inverse aspect ratio expansion: $B_\theta/B_z \sim \varepsilon$, $q \sim 1$, and $2\mu_0 p/B_z^2 \sim \varepsilon^2$, where $\varepsilon = a/R_0 \ll 1$. Substituting this expansion into the general screw pinch analysis leads to a remarkably simple form for δW_F. This form, nonetheless, describes at a basic level many practical limits on tokamak operation.

To put the analysis in perspective one should keep in mind that, in general, experimental tokamak performance seriously degrades when either the current or pressure becomes too large. The straight tokamak is surprisingly accurate in describing the effects of large current. It is not very reliable with respect to pressure-driven limitations because the effects of toroidicity tend to dominate and are obviously not included in the straight tokamak model. With this as background, the specific tokamak operational limits discussed in this section include the following:

- Sawtooth oscillations – internal $m = 1$ mode
- Current-driven disruptions – external low m modes
- Density-driven disruptions – external low m modes
- Resistive wall modes – external low m modes
- Edge localized modes (ELMs) – external high m modes.

It is worth emphasizing that each of the above phenomena is macroscopic in nature and readily observed experimentally. A complete description of any of these

phenomena requires non-linear simulations plus the inclusion of additional physical effects not contained in the straight, ideal MHD, tokamak model. Such effects include toroidicity, non-circularity, resistivity, two-fluid modeling, kinetic behavior, and turbulent transport. Still, at the initiation, each phenomenon is driven by an ideal MHD instability.

The net result of exceeding any of the above operational limits is highly degraded experimental performance ranging from greatly enhanced transport to catastrophic termination. Ideal MHD achieves the important goal of describing how to avoid such unfavorable behavior from occurring in the first place. The answers can be quite helpful in that the theory provides certain quantitative guidelines that can be implemented experimentally; for example, keep the current or pressure peaked and below a critical value. Other guidelines, while straightforward conceptually, are often not easy to implement experimentally; for example, keep the edge current density gradient below a critical value. Here is where the skill and inventiveness of experimentalists are crucial.

It should also be noted that there are additional operational limits on tokamaks that are not initiated by ideal MHD instabilities. Neo-classical tearing modes leading to disruptions are one example. These require advanced analysis and are not discussed here.

The analysis below starts with a derivation of the reduced form of δW applicable to the straight tokamak. Each of the phenomena listed above is then described physically and investigated by means of the straight tokamak MHD model.

11.6.1 Reduction of δW *for the straight tokamak*

The large aspect ratio expansion

The straight tokamak potential energy is obtained by substituting the tokamak expansion into the general screw pinch form of δW given by Eqs. (11.98) and 11.90). The result is an asymptotic expansion of the form $\delta W = \delta W_0 + \delta W_2 + \delta W_4 + \cdots$, where each term scales as $\delta W_n \sim \varepsilon^n \delta W_0$ with $\delta W_0 \sim B_0^2 R_0 \xi^2 / \mu_0$. The calculation is straightforward although one must include the toroidal periodicity constraint by setting

$$k = -\frac{n}{R_0} \tag{11.171}$$

Here, n is an integer representing the toroidal mode number. The toroidal periodicity constraint is important in a tokamak since most of the unstable modes have long wavelengths, corresponding to $n \sim 1$; in other words, k cannot realistically be thought of as a continuously varying parameter.

The first non-vanishing contribution to δW is of second order and is given by (Shafranov, 1970)

$$
\delta \hat{W}_2 = \frac{\delta W_2}{\varepsilon^2 W_0} = \int_0^a \left(\frac{n}{m} - \frac{1}{q} \right)^2 \left[r^2 \xi'^2 + \left(m^2 - 1 \right) \xi^2 \right] r\, dr
$$
$$
+ \left(\frac{n}{m} - \frac{1}{q_a} \right) \left[\left(\frac{n}{m} + \frac{1}{q_a} \right) + m\Lambda \left(\frac{n}{m} - \frac{1}{q_a} \right) \right] a^2 \xi_a^2
$$

$$(11.172)$$

where $W_0 = 2\pi^2 R_0 B_0^2 / \mu_0 a^2$ and the subscript "a" denotes evaluation at $r = a$. Also, keep in mind that without loss in generality it has been assumed that $m \geq 0$ and $-\infty < n < \infty$. One major advantage of the straight tokamak configuration, as demonstrated in the relevant examples below, is that complete MHD stability against all MHD modes can be achieved without the need for a conducting wall.

The absence of pressure

An interesting feature of the straight tokamak form of δW is the absence of the pressure, a consequence of the fact that β is assumed to be small in either the ohmic or high β tokamak expansions. This feature can also be demonstrated by examining Suydam's criterion for localized interchanges which is exact, requiring no expansion in ε. It does, however, simplify when the ε expansion is substituted. Using the definition $\beta(r) = 2\mu_0 p(r)/B_0^2$, one finds that Suydam's criterion for stability reduces to

$$
\left(\frac{rq'}{q} \right)^2 + 4r\beta' > 0
$$

$$(11.173)$$

Since $\beta \sim \varepsilon$ or ϵ^2 and $rq'/q \sim 1$ it follows that Suydam's criterion is easily satisfied over almost the entire profile. The only exception is near the axis where, because of cylindrical geometric effects the shear is small. Expanding near the axis allows Eq. (11.173) to be written as

$$
\left(\frac{q_0''}{q_0} \right)^2 r^2 + 4\beta_0'' > 0
$$

$$(11.174)$$

where the "0" subscript denotes evaluation at $r = 0$. The criterion is always violated near the axis unless the pressure is flattened over a small region,

$$
\Delta r/a = \left(2q_0/aq_0'' \right) \left(-\beta_0'' \right)^{1/2} \sim \beta^{1/2} \ll 1
$$

$$(11.175)$$

Stability requires only a mild alteration of the profile. It is worth noting, neverthe-less, that this is one example where the pressure effects in the straight tokamak lead to a qualitatively different result than for the toroidal case. The differences are discussed in the next chapter where it is shown that toroidal curvature effects modify the stability criterion such that under reasonable conditions on q_0 no flattening of the pressure profile is required.

11.6.2 Sawtooth oscillations – the internal **m** = 1 mode

The first important straight tokamak instabilities to investigate are the low m internal kink modes. The analysis shows that only the $m = 1$ mode can lead to an instability whose non-linear evolution results in sawtooth oscillations. The internal kink mode theory and corresponding experimental description of sawtooth oscillations are described below.

Evaluation of δW_F for internal modes

For internal modes one sets $\xi(a) = 0$ and $\delta W = \delta W_F$. The general form of the potential energy, given by Eq. (11.172), reduces to

$$\delta \hat{W}_2 = \int_0^a \left(\frac{n}{m} - \frac{1}{q} \right)^2 \left[r^2 \xi'^2 + (m^2 - 1)\, \xi^2 \right] r dr \tag{11.176}$$

At first glance it would appear that all internal modes are stable since every term is positive. This is certainly true for $m \geq 2$ since both terms in the integrand are positive and non-zero.

For $m = 1$ one needs to be more careful before concluding stability since the second term in the integrand vanishes. The $m = 1$ mode is stable when the $q(r)$ profile increases with r (as it usually does for a tokamak) and $nq_0 > q_0 > 1$ or when $n \leq 0$. For these cases $n/m - q(r)$ never vanishes and only enters the integrand as a positive coefficient.

However, if a $q = 1$ surface exists in the plasma (i.e., $q_0 < 1 < q_a$) then an $n = 1$ trial function can be constructed, as shown in Fig. 11.27, that causes $\delta \hat{W}_2 \to 0$ as the width of the pedestal δ shrinks to zero. Specifically, for the trial function in Fig. 11.27 one can easily show that

$$\delta \hat{W}_2 = \frac{1}{12} \left(r_1^3 q_1'^2 \xi_0^2 \right) \delta \to 0 \tag{11.177}$$

Here, the subscript "1" denotes evaluation at the $q = 1$ surface.

The implication is that plasma is marginally stable to order ε^2 when a $q = 1$ surface exists in the plasma. To determine stability requires the evaluation of the next non-vanishing contribution to δW which for the straight tokamak occurs
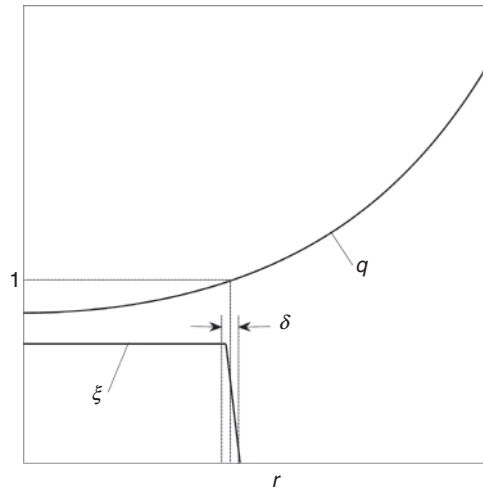
Figure 11.27   Trial function for an $m = 1$ internal kink mode in a straight tokamak.

in order ε^4. This contribution is obtained by a straightforward expansion of Eq. (11.90) and leads to (Rosenbluth *et al.*, 1973)

$$\delta\hat{W}_4 = \frac{\delta W_4}{\varepsilon^4 W_0} = \xi_0^2 \int_0^{r_1} \left[r\beta' + \frac{r^2}{R_0^2}\left(1 - \frac{1}{q}\right)\left(3 + \frac{1}{q}\right) \right] r\,dr \qquad (11.178)$$

Both contributions to the integrand are negative indicating that the plasma is unstable. Physically, when a plasma has an internal $q = 1$ surface, the stabilizing effects of line bending vanish and the destabilizing effects due to the parallel current and unfavorable curvature dominate, leading to instability.

Toroidal effects have a large impact on the form of the correction to δW_2 and are discussed in Chapter 12. The results are more complicated but essentially the same conclusion is reached – stability against the internal $m = 1$, $n = 1$ requires

$$q_0 > 1 \qquad (11.179)$$

The next question to address is "What happens to the plasma when the stability criterion is violated?"

Sawtooth oscillations

Tokamak experiments experience a form of relaxation oscillation known as the "sawtooth oscillation" when $q_0 < 1$. Although the mode structure can be complex in a torus, the dominant harmonic is $m = 1$, $n = 1$. Thus, the mode is closely connected, at least in terms of its initial drive, with the ideal mode just discussed.
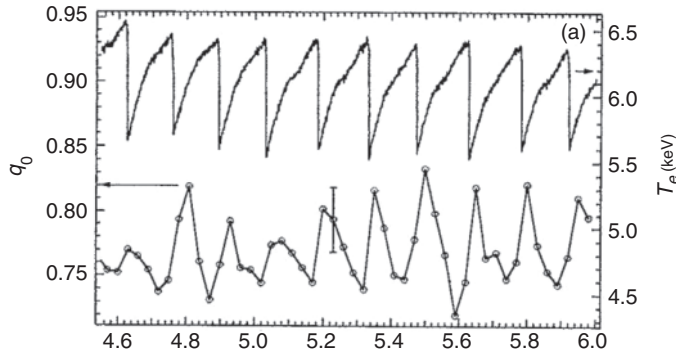
Figure 11.28   Experimental trace of the $T_e(0)$ and q_0 vs. time showing sawtooth oscillations (from Yamada *et al.*, 1994). Reproduced with permission.

Typical experimental traces of the on axis plasma temperature and safety factor as a function of time during a sawtooth oscillation are illustrated in Fig. 11.28 (Yamada *et al.*, 1994). The shape of the time evolution makes it obvious why it is called a sawtooth oscillation. A qualitative picture of the behavior is as follows. The oscillation is basically a two-stage process. In the first stage, corresponding to the long run-up before the collapse, the plasma is heated by classical means, usually ohmic power. Since the current density $J \approx E_0/\eta \propto T^{3/2}$, its central value J_0 increases with time as the heating progresses. Furthermore, since

$$q_0 = \frac{2B_0}{\mu_0 R_0 J_0} \tag{11.180}$$

one sees that an increase in J_0 causes a decrease in q_0.

Eventually, q_0 decreases below the marginal stability value $q_0 = 1$, after which the $m = 1, n = 1$ MHD mode is excited. This second stage corresponds to the rapid "crash" of the sawtooth. During this phase energy and current are expelled from the $q_0 < 1$ region and redistributed to the mid to outer regions of the plasma. Once the crash is completed, another run-up period begins and the process repeats itself. Overall, sawtooth oscillations do not cause a major degradation of plasma performance. Their main effect is to limit the maximum current density on axis to the value

$$J_0 \leq J_{\text{max}} = \frac{2B_0}{\mu_0 R_0} \tag{11.181}$$

Only when the instability criterion is exceeded by a large amount can the sawtooth oscillations negatively affect plasma performance. In this regime the redistributed

energy can actually reach the plasma boundary and be lost from the system. This is rarely the regime in which tokamaks are operated.

If one does not look too closely, the above picture would seem to explain sawtooth oscillations and their connection to the internal $m = 1$, $n = 1$ MHD mode. However, a closer comparison of the data with non-linear simulations, including resistive effects, shows that certain important aspects of sawtooth behavior are still not understood from first principles. Specifically, it is difficult to predict (1) the length of the long run-up period, (2) the depth of the crash before the plasma recovers, and (3) the fact that in many tokamaks the central safety factor does not oscillate about the value $q_0 = 1$, but a slightly lower value $q_0 \simeq 0.75$.

At present, the sawtooth oscillation remains an active area of research. Still, stepping back, one sees that from an overall perspective, the ideal MHD stability criterion, $q_0 > 1$ provides a reasonable estimate of the maximum allowable current density on the axis of a tokamak. Also, in the context of the straight tokamak model, internal ideal MHD modes with $m \geq 2$ should be stable.

11.6.3 Current-driven disruptions – external low m *modes*

The second important class of instabilities described by the straight tokamak model is the low m external kink mode. This is the most dangerous mode experimentally, usually leading to a catastrophic collapse of the plasma current and pressure, known as a major disruption. Mathematically, external kinks are more dangerous energetically than internal kinks since their stability is determined solely by the second-order contribution to δW. The modes can be driven by too much current or a combination of too much current and too much pressure. The straight tokamak model provides a reasonable description of the purely current-driven external kink.

The analysis presented below separates into two parts. The first part involves the $m = 1$ mode and leads to the well-known Kruskal–Shafranov current limit for tokamaks. This is a purely analytic calculation. The second part treats the case of $m \geq 2$ external kinks. These modes produce a more restrictive limit on the allowable current whose value is determined by a combination of analytic and numerical calculations.

The $m \geq 2$ stability boundary depends, not only on the total current, but on the current density profile as well, particularly the steepness of the edge gradient. This behavior is demonstrated by analyzing several profiles with increasing flatness of the edge gradient.

As stated earlier, all external modes can be stabilized for reasonable profiles without the need of a perfectly conducting wall.

Possible ranges of unstable wave numbers

The stability of low m external kinks is determined by an analysis of the full δW given by Eq. (11.172) but with the conducting wall moved to infinity: $b/a \to \infty$ implying that $\Lambda = 1$. The potential energy is thus given by

$$
\begin{aligned}
\delta \hat{W}_2 = \int_0^a & \left(\frac{n}{m} - \frac{1}{q} \right)^2 \left[r^2 \xi'^2 + \left(m^2 - 1 \right) \xi^2 \right] r \, dr \\
& + \left(\frac{n}{m} - \frac{1}{q_a} \right) \left[\left(\frac{n}{m} + \frac{1}{q_a} \right) + m \left(\frac{n}{m} - \frac{1}{q_a} \right) \right] a^2 \xi_a^2
\end{aligned}
\tag{11.182}
$$

One can gain some insight into the possible range of unstable wave numbers by noting that the integral contribution to $\delta \hat{W}_2$ is either positive or zero and again assuming without loss in generality that $q_a > 0$, $m > 0$, and $-\infty < n < \infty$. By examining the boundary term one then sees that sufficient conditions for stability to a given m, n mode can be written as

$$
\begin{aligned}
\frac{n}{m} &> \frac{1}{q_a} \\
\frac{n}{m} &< 0
\end{aligned}
\tag{11.183}
$$

Alternatively this implies that a necessary condition for instability is that

$$
0 < nq_a < m
\tag{11.184}
$$

If $q(r)$ is an increasing function of radius as it is for a tokamak, then Eq. (11.184) implies that the resonant surface for an external mode, located at the radius r_s where $nq(r_s) = m$, must lie in the vacuum region: $q(r_s) > q_a$.

The m = *1 Kruskal–Shafranov limit*

Consider now the $m = 1$ mode. For this case the minimizing trial function in the plasma is simply given by $\xi(r) = \xi_a = $ constant. This choice makes the integral contribution to $\delta \hat{W}_2$ vanish. Note that such a trial function can only be chosen for an external mode since the internal mode boundary condition $\xi_a = 0$ no longer need be applied. In addition, since the trial function $\xi(r) = $ constant actually minimizes the integral contribution, it thereby coincides with the true eigenfunction for the mode. A final important point is that the minimizing trial function is independent of the $q(r)$ profile. This leads to the important conclusion that the $m = 1$ stability boundary is a function only of q_a. In other words, the criterion depends only on the total current but not the current profile.
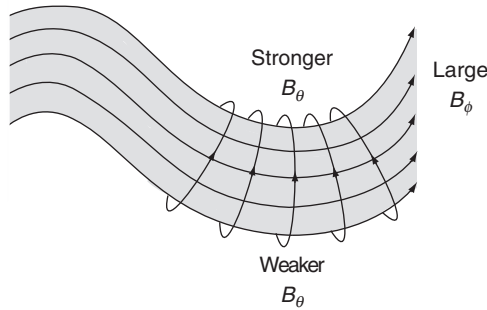
Figure 11.29   Physical driving mechanism for the $m = 1$ Kruskal–Shafranov external kink mode. Note the compression of the field near the inside of the kink perturbation and the bending of the toroidal field lines.

After making use of these results one finds that $\delta\hat{W}_2$ reduces to

$$\delta\hat{W}_2 = \frac{2a^2\xi_a^2}{q_a}n(nq_a - 1) \tag{11.185}$$

From Eq. (11.185) it follows that the condition to stabilize the $m = 1$ external kink mode for the most restrictive case, $n = 1$, is given by

$$q_a > 1 \tag{11.186}$$

This criterion is known as the Kruskal–Shafranov condition (Kruskal and Schwarschild, 1954; Shafranov, 1956). It imposes an important constraint on tokamak operation in that it limits the total toroidal current that can flow to

$$I < I_{KS} = \frac{2\pi a^2 B_0}{\mu_0 R_0} = \frac{5a^2 B_0}{R_0}\,\text{MA} \tag{11.187}$$

For, $a = 2\,\text{m}$, $R_0 = 6\,\text{m}$, and $B_0 = 6\,\text{T}$, then $I_{KS} = 20\,\text{MA}$. This limit can be increased substantially for tokamaks with an elongated cross section.

The driving mechanism for the instability is similar to that of a Z-pinch as discussed in Section 11.4.1 and illustrated here for the tokamak case in Fig. 11.29. The one main difference is that the modes are restricted to long wavelengths in order to minimize the strong stabilizing effects of bending the B_z field lines. In fact the criterion $q_a > 1$ can also be viewed as a constraint on the geometry that prevents the formation of long wavelength modes by not allowing them to fit in the torus because of toroidal periodicity requirements.

In practical situations the $m = 1$ mode is rarely seen experimentally because of the unfortunate fact that higher m modes produce even stricter requirements on the maximum allowable current. These modes have slightly lower growth rates and are

more dependent on the current density profile than the $m = 1$ mode but still lead to major disruptions. These modes are the next topic of discussion.

The m ≥ 2 external kink modes

The stability of $m \geq 2$ external kinks requires an evaluation of both the integral and boundary terms in $\delta \hat{W}_2$. As stated, in this subsection attention is focused on several current density profiles with increasing flatness of the edge gradient. The stability boundaries are determined either analytically or numerically by solving the differential equation for the $\xi(r)$ that minimizes the integral contribution to $\delta \hat{W}_2$. This equation is given by

$$\frac{d}{dr}\left[r^3 \left(\frac{n}{m} - \frac{1}{q}\right)^2 \frac{d\xi}{dr}\right] - (m^2 - 1)\, r\left(\frac{n}{m} - \frac{1}{q}\right)^2 \xi = 0 \tag{11.188}$$

$$\xi(\delta \to 0) = \delta^{m-1} \qquad \xi'(\delta \to 0) = (m-1)\delta^{m-2}$$

From this solution one evaluates $a\xi'_a/\xi_a$ and substitutes into the following form of $\delta \hat{W}_2$ obtained from Eq. (11.118) after substituting the tokamak expansion,

$$\delta \hat{W}_2 = \frac{1}{m^2 q_a^2}(nq_a - m)\left[(nq_a + m) + \left(m + \frac{a\xi'_a}{\xi_a}\right)(nq_a - m)\right]a^2\xi_a^2 \tag{11.189}$$

An accurate solution is required because the results are sensitive to the value of $a\xi'_a/\xi_a$, which therefore must be calculated with high precision. When a numerical solution is required it is easy to obtain since for an unstable mode there is no singular surface in the plasma.

A flat J(r) profile with a jump at r = a

The first case of interest corresponds to a flat current density profile which abruptly drops to zero at the plasma edge as illustrated in Fig. 11.30. As shown below this is the maximally unstable profile. The analysis is easy to carry out since the flat profile produces a $B_\theta \propto r$ which in turn leads to a constant safety factor profile: $q_0 = q_a = q(r) = rB_0/R_0 B_\theta(r) = $ constant. Clearly, the factor $n/m - 1/q(r)$ is also constant and factors out of the basic differential equation for ξ (i.e., Eq. (11.188)) which reduces to

$$\frac{d}{dr}\left[r^3 \frac{d\xi}{dr}\right] - (m^2 - 1)\, r\xi = 0 \tag{11.190}$$

Now, observe that the minimizing $\xi(r)$ that satisfies Eq. (11.190), is given by

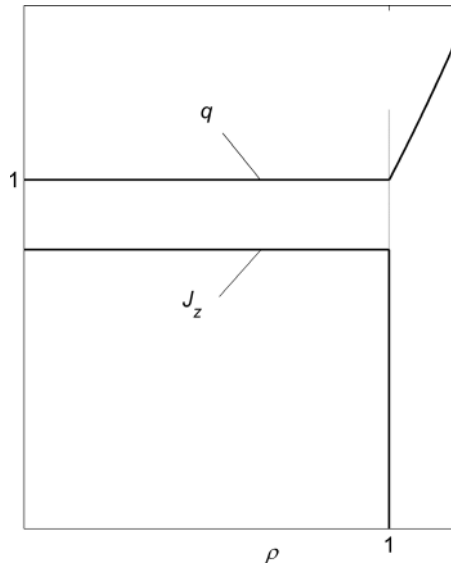$$\xi(r) = \xi_a \left(\frac{r}{a}\right)^{m-1} \tag{11.191}$$

Figure 11.30   A flat $J_z(r)$ profile with a jump at the plasma edge. Also shown is the $q(r)$ profile. Here $\rho = r/a$.

which implies that

$$\frac{a\xi_a'}{\xi_a} = m - 1 \tag{11.192}$$

Equation (11.192) is substituted into $\delta\hat{W}_2$ (i.e., Eq. (11.189)) yielding

$$\delta\hat{W}_2 = \frac{2}{mq_a^2}(nq_a - m)(nq_a - m + 1) \tag{11.193}$$

The conclusion is that, for a given value of m, the condition on q_a for instability can be written as

$$m - 1 < nq_a < m \tag{11.194}$$

The unstable values of nq_a are bracketed by adjacent values of m. By setting $n = 1$ and continuously incrementing m by unity it then follows that the plasma is unstable over the entire range $0 \leq q_a \leq \infty$! This is, therefore, the maximally unstable tokamak profile. When it comes to avoiding external kink modes, plasmas do not want to have edge current jumps.

Linear J(r) edge gradient

To show the sensitivity of the stability results to the current profile the calculation just presented is repeated for a $J(r)$ profile which vanishes at $r = a$ but with a linear edge gradient. For this case the model profile is given by
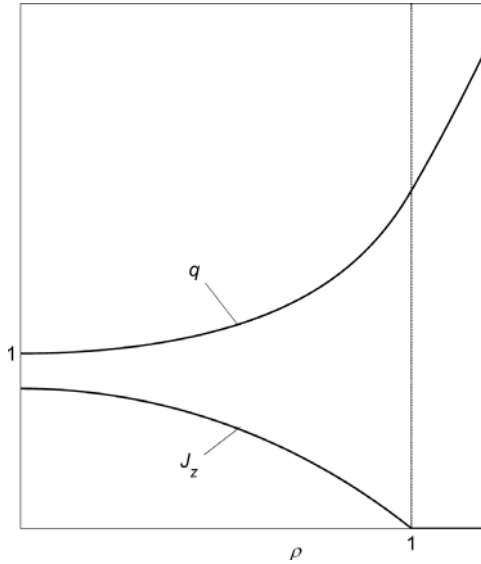
Figure 11.31 Profiles of $J_z(r)$ vs. r with zero edge current but a finite edge current gradient. Also shown is $q(r)$. Here $\rho = r/a$.

$$J(\rho) = J_0\left(\frac{1 - \rho^2}{1 - \alpha\rho^2}\right) \tag{11.195}$$

Here, $\rho = r/a$, J_0 is the current density on axis, and α is a free profile parameter that must lie in the range $-\infty < \alpha < 1$. The value of α determines the ratio q_a/q_0. For any value of α the edge gradient is a constant: $J'(1) = -2J_0/(1 - \alpha)$. A typical profile is illustrated in Fig. 11.31.

The $J(\rho)$ profile is substituted into Ampere's law yielding $B_\theta(\rho)$ and the safety factor $q(\rho) = (\varepsilon B_0)(\rho/B_\theta)$. The safety factor and its edge value, which are the quantities needed for the evaluation of $\delta\hat{W}_2$, can be written as

$$
\begin{aligned}
\frac{q_0}{q(\rho)} &= \frac{1}{\alpha^2\rho^2}\left[\alpha\rho^2 + (1 - \alpha)\ln\left(1 - \alpha\rho^2\right)\right] \\
\frac{q_0}{q_a} &= \frac{1}{\alpha^2}\left[\alpha + (1 - \alpha)\ln(1 - \alpha)\right]
\end{aligned}
\tag{11.196}
$$

where $q_0 = 2B_0/\mu_0 R_0 J_0$. The $q(\rho)$ profiles is also illustrated in Fig. 11.31.

The variational equation for ξ (i.e., Eq. (11.188)) is now solved numerically in order to evaluate $a\xi'_a/\xi_a$. In all cases the safety factor on axis has been set to $q_0 = 1$. This is a simple way to model the physical effects of sawtooth oscillation while mathematically guaranteeing that the plasma is stable to all internal MHD modes. In addition, since $q(\rho)$ is always an increasing function of ρ for the model profiles, this implies that $q_a \geq q_0 > 1$. The profiles automatically satisfy the Kruskal–Shafranov stability criterion.
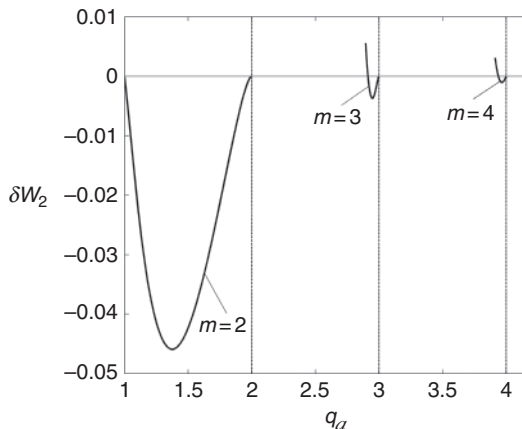
Figure 11.32   Plot of δW vs. q_a assuming $q_0 = 1$ and $n = 1$ for the constant edge gradient profile. Shown here are δW ($m = 2$), $100\delta W$ ($m = 3$), and $100\delta W$ ($m = 4$).

The quantity $a\xi_a'/\xi_a$ is substituted into the expression for $\delta\hat{W}_2$ (i.e., Eq. (11.189)) leading to the stability diagram illustrated in Fig. 11.32. Observe that the $m = 2$, $n = 1$ mode is again unstable for $1 < q_a < 2$. However, unlike the case with a finite current jump, there are narrow, rather than full, bands of instability just below $q_a = 3$ and $q_a = 4$. Note also the expanded vertical scale for $m = 3$ and $m = 4$. In fact it is shown in Section 11.6.6 that for a linear edge gradient these bands exist for all higher m values but become exponentially narrower as m increases. Also, the magnitude of $\delta\hat{W}_2$ corresponding to instability decreases rapidly with increasing m indicating weaker instability.

The overall conclusions are not as definitive as one would like. There are windows of stability between adjacent m values. However, practical operation of an experiment within such a window reduces its robustness against instability as the profiles evolve slowly in time. Often, tokamaks operate reasonably successfully with $q_a > 3$. Operation with $q_a \sim 2.5$ is sometimes possible, but can lead to major disruptions, tolerable in present experiments but not in ITER or a reactor.

Lastly, it is worth noting that the critical q_a for stability is affected by toroidicity and finite pressure. In addition, if the tokamak has a divertor then by definition $q_a = \infty$. By consensus, although not because of any rigorous mathematical analysis, the value of "q_a" in a diverted tokamak is assumed to be $q(\psi)$ evaluated at the ψ surface corresponding to 95% of the total flux and is often abbreviated as q_{95}. These issues are discussed in the next chapter.

For the present, it is reasonable to assume that $q_a > 3$ to safely avoid ideal MHD external kink modes which lead to major disruptions. Other, non-ideal effects can sometimes raise this limit even higher.
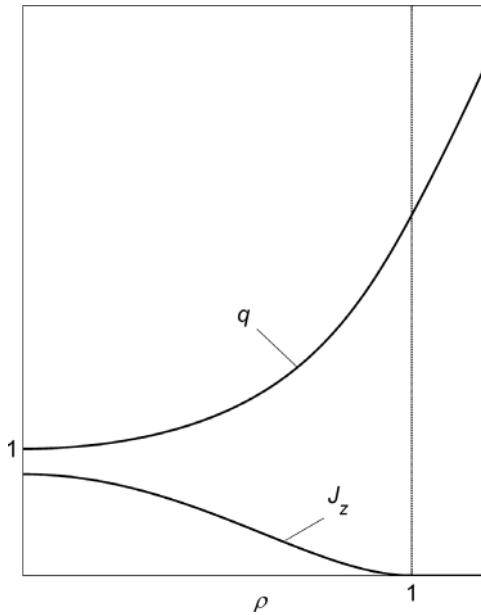
Figure 11.33   Profile of $J_z(r)$ vs. r with zero edge current and zero edge current gradient. Also shown is $q(r)$. Here $\rho = r/a$.

Flat J(r) *edge gradient*

A convenient choice for the current density profile with a flat edge gradient has the form

$$J(\rho) = J_0 \left(\frac{1 - \rho^2}{1 - \alpha\rho^2} \right)^2 \tag{11.197}$$

Again, $\rho = r/a$, J_0 is the current density on axis, and α is a free profile parameter that must lie in the range $-\infty < \alpha < 1$. Observe that both the current density and its gradient vanish at the plasma edge $\rho = 1$ for any value of α. A typical profile is illustrated in Fig. 11.33.

The safety factor and its edge value, obtained from Ampere's law, can be written as

$$
\begin{aligned}
\frac{q_0}{q(\rho)} &= \frac{1}{\alpha^3\rho^2} \left\{ \alpha\rho^2 \left[1 + \frac{(1-\alpha)^2}{(1-\alpha\rho^2)} \right] + 2(1-\alpha)\ln(1-\alpha\rho^2) \right\} \\
\frac{q_0}{q_a} &= \frac{1}{\alpha^3} \left[\alpha(2-\alpha) + 2(1-\alpha)\ln(1-\alpha) \right]
\end{aligned}
\tag{11.198}
$$

where $q_0 = 2B_0/\mu_0 R_0 J_0$. The safety factor profile is also plotted in Fig. 11.33.
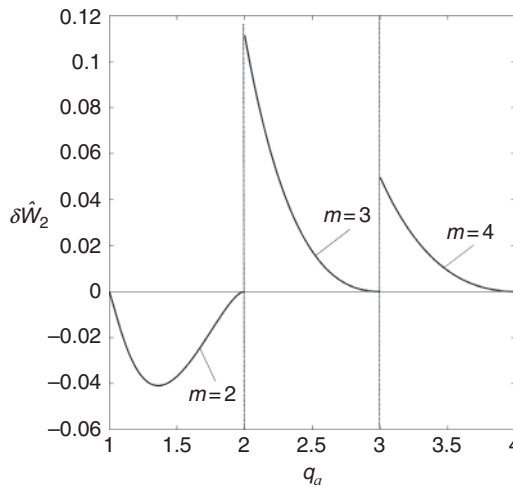
Figure 11.34   Plot of $\delta\hat{W}$ vs. q_a assuming $q_0 = 1$ for several values of m and $n = 1$ corresponding to the zero edge gradient profile.

The stability problem has now been fully formulated. The resulting numerical solutions determine $a\xi'_a/\xi_a$, which is substituted into the expression for $\delta\hat{W}_2$. The stability boundaries are presented in Fig. 11.34 which illustrates curves of $\delta\hat{W}_2$ vs. q_a for $q_0 = 1$, $n = 1$, and various values of m.

From Fig. 11.34 one sees that only $m = 2$ is unstable. The upper boundary is $q_a = 2$ while the lower boundary is $q_a = 1$. Higher $m \geq 3$ bands of instability no longer exist. The overall conclusion is that the condition for a straight tokamak to be stable against external kinks, subject to the constraints that (1) q_0 account for sawtooth oscillations and (2) the edge current density and its gradient are both zero, is given by

$$q_a > 2 \tag{11.199}$$

The maximum allowable current is one half of the Kruskal–Shafranov current. The situation has improved over the finite edge gradient case but it is not clear whether such flat edge gradients can be reliably achieved experimentally. Still, complete stability is possible without the need of a conducting wall.

Maximally flat J(r) edge gradient

The last profile of interest corresponds to the maximally flat $J(r)$ edge gradient. This profile, first suggested by Shafranov (1970), is illustrated in Fig. 11.35. Observe that the current density is uniform between $0 < r < r_0$ and zero between $r_0 < r < a$. This implies that the safety factor $q(r) = q_0$ between $0 < r < r_0$ and $q(r) = q_0\left(r^2/r_0^2\right)$ between $r_0 < r < a$. Clearly, the free radial parameter r_0 sets the edge value of q: $q_a = q_0\left(a^2/r_0^2\right)$.
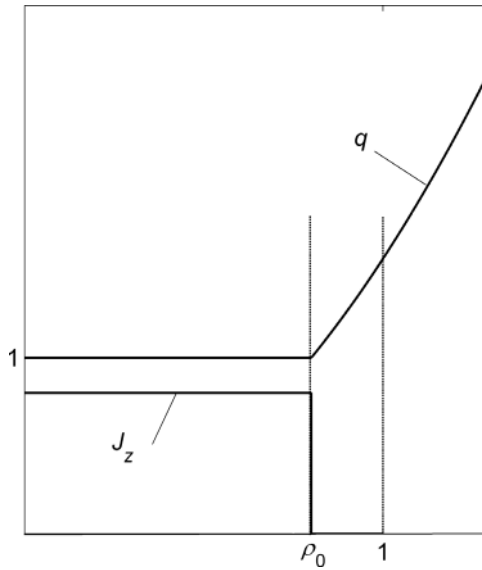
Figure 11.35   The maximally flat edge current gradient profile $J_z(r)$ vs. r. Also shown is the corresponding $q(r)$ profile. Here $\rho_0 = r_0/a$.

There are several reasons for analyzing this idealized profile. First, the calculation is completely analytic. Second, the advantages of a flat edge gradient are explicitly demonstrated. Third, because of its simplicity, it is easy to obtain a global picture of external kink mode stability as a function of q_0 and q_a.

Interestingly, the stability results for this maximally flat $J(r)$ edge gradient model can be directly obtained from the maximally unstable profile with the edge current jump. The reasoning is as follows. The interior region of the plasma has a flat current density which jumps to zero at $r = r_0$. This produces the same contribution to δW_F as the profile with the edge jump if one sets $a \to r_0$ and $q_a \to q_0$.

Next, observe that the contribution to δW_F from the region $r_0 < r < a$ is simply given by

$$\delta W_F = \frac{1}{2\mu_0} \int \mathbf{Q}^2 \, d\mathbf{r} = \frac{1}{2\mu_0} \int \mathbf{B}_1^2 \, d\mathbf{r} \qquad (11.200)$$

since $J(r) = 0$ in this region and $p(r)$ is negligible because of the tokamak ordering. Equation (11.200) is the same form as the vacuum energy. Therefore, the combined contribution to δW from the region $r_0 < r < a$ plus the actual vacuum region is identical to that obtained from the profile with the edge jump if one again sets $a \to r_0$ and $q_a \to q_0$.
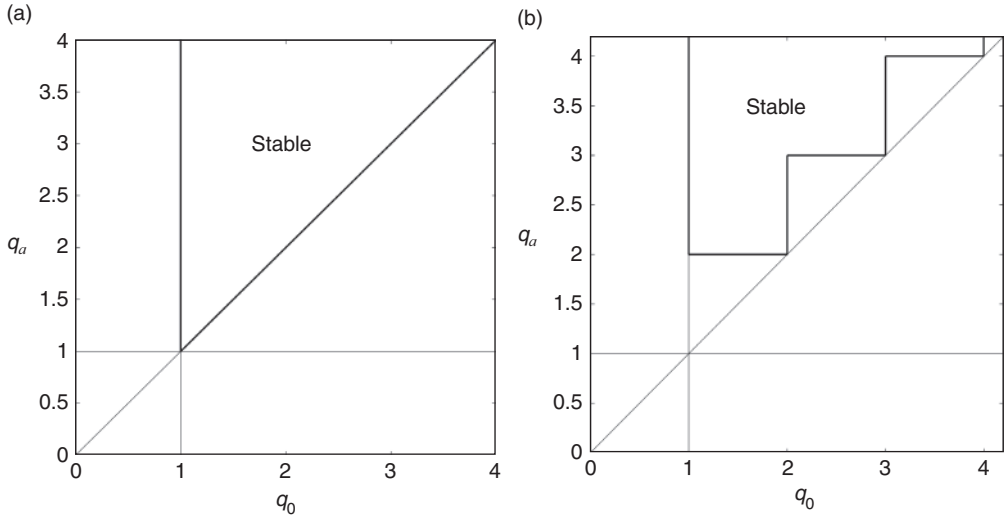
Figure 11.36   Stability diagram of q_a vs. q_0 for $n = 1$ corresponding to the maximum flat edge gradient profile: (a) basic diagram only including the $m = 1$ mode; (b) complete diagram including higher m modes. Note the additional regions of instability. In all cases the region encompassed by the heavier lines is stable.

The end result is that δW for the flat edge gradient model, with one crucial additional constraint, can be directly written down from Eq. (11.193) in terms of the equivalent variables as follows:

$$\delta \hat{W}_2 = \frac{2}{mq_0^2} (nq_0 - m)(nq_0 - m + 1) \qquad (11.201)$$

For a given m the plasma is unstable for

$$m - 1 < nq_0 < m \qquad (11.202)$$

Consider now the additional constraint that follows from the fact that external modes can only be unstable if the resonant surface lies in the vacuum region. Stated differently, the above analysis is only valid if there is no resonant surface in the region $r_0 < r < a$. See the discussion associated with Eq. (11.183) which applies to arbitrary profiles. As has already been shown Eq. (11.183) implies that for the resonant surface to lie in the vacuum region one requires that $nq_a < m$. This condition, combined with the fact that $q_a > q_0$ for a tokamak, leads to an instability constraint on q_a that can be written as

$$nq_0 < nq_a < m \qquad (11.203)$$

Equations (11.202) and (11.203) define the stability boundaries for the flat edge gradient model. They can be conveniently illustrated in Fig. 11.36 as a diagram of

q_a vs. q_0 for the most dangerous case $n = 1$. Figure 11.36a shows the basic diagram consisting of the $q_0 > 1$ boundary for sawtooth stability, $q_a > 1$ for Kruskal–Shafranov stability, and $q_a > q_0$ the basic definition of a tokamak. The area encompassed by the heavier lines is stable under these constraints.

Figure 11.36b shows the additional unstable regions due to higher m external kinks as described by Eqs. (11.202) and (11.203). For a given m Eq. (11.202) corresponds to a vertical band of instabilities. Similarly, Eq. (11.203) produces a triangular wedge. The overlap of these two regions corresponds to an instability. The net result is that the stable region has been reduced in size because of the higher m kink modes. The maximum allowable plasma current (i.e., lowest allowable q_a) corresponds to $q_a = 2$ and occurs for $1 < q_0 < 2$.

The analysis just presented has shown analytically that a flat edge gradient is desirable for good stability to $m > 2$ external kink modes.

Major disruptions

With the theory of external kink modes now established, the final topic of interest is a basic description of a major disruption. The actual physics describing the evolution of a major disruption is quite complicated involving both ideal and resistive MHD. An excellent description has been given by Wesson (2011). Qualitatively what happens during a disruption is as follows. As the total current in the plasma is increased sawtooth oscillations continue to limit the safety factor on axis to $q_0 = 1$, which corresponds to $J_0 = 2B_0/\mu_0 R_0$. Since the current density on axis is fixed and the total current is increasing, the implication is that the current profile must become broader. The edge gradient becomes steeper and the $q = 2$ surface moves closer to the plasma edge.

These are just the conditions necessary to excite internal resistive tearing modes, particularly the $m = 2$ mode. The tearing modes lead to the development of magnetic islands which tend to further flatten the current profile within the islands. Equally important, when islands with different m, n combinations overlap the magnetic field can become stochastic leading to greatly enhanced transport. The enhanced transport in turn first leads to a rapid quenching of the plasma thermal energy. This thermal quench is one of two main dangers due to major disruptions. Specifically, all the plasma energy is rapidly deposited on the first wall which may not be able to withstand the resulting thermal loads, particularly in large devices.

An equally important effect that occurs on a slightly slower time scale is the unfavorable redistribution of the current density. The profile becomes flat over the core because of the turbulence eventually reaching a state where an ideal external MHD mode is excited. In reality, $\text{Im}(\omega)$ is much smaller than the ideal growth rate because the core is surrounded by a low-temperature resistive plasma and not a
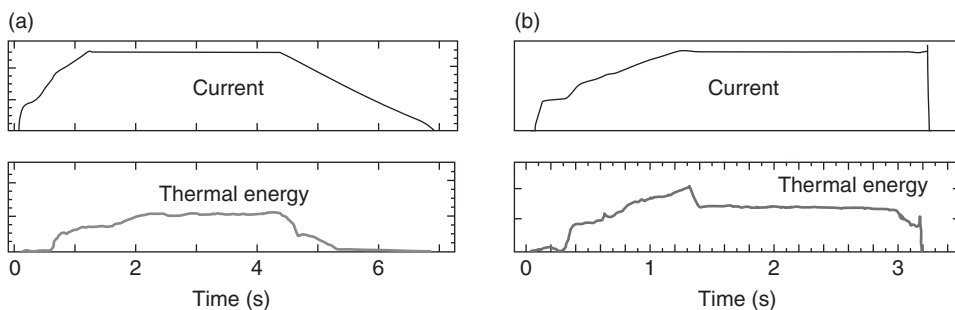
Figure 11.37　Experimental observation of the quenching of pressure and current during a major disruption (reproduced with permission from Kikuchi *et al*., 2012). (a) No disruption, (b) major disruption at $t = 3.2$ sec.

pure vacuum. Even so the end result is the same in that the entire plasma starts to move away from its equilibrium position.

This motion, which carries the plasma to the wall of the vacuum vessel, is the second main danger due to major disruptions. During the time that the plasma is moving its current quenches because of enhanced magnetic transport and transference of current to the wall by direct contact. In a short time the entire plasma current is quenched and reappears in the wall with a non-uniform distribution approximately corresponding to the m, n mode structure of the MHD instability. This large, non-uniform current produces very large, potentially damaging electromagnetically driven mechanical stresses on the first wall.

Experimental data demonstrating the quenching of the pressure and current during a major disruption are illustrated in Fig. 11.37 (Kikuchi *et al*., 2012). The rapid increase in wall current leads to enormous forces on the vacuum chamber and this is the main danger of a major disruption. Current experiments are small enough to withstand these forces but in much larger reactor scale devices the forces are also much larger. There is general consensus that major disruptions must be avoided in a tokamak reactor in order to prevent irreversible damage to the vacuum chamber.

11.6.4 Density-driven disruptions – external low m modes

Overview

High-performance operation of a tokamak requires that the plasma density lie below a critical value, known as the "Greenwald density limit." As the plasma density approaches the limit from below, the edge begins to cool and transport starts to degrade. When the limit is exceeded, a major disruption occurs. The empirical value of the density limit has a surprisingly simple form and is valid over

a very wide range of parameters. Its value is given by (Greenwald *et al.*, 1988; Greenwald, 2002)

$$n_{20} < n_G = \frac{I_M}{\pi a^2} \qquad (11.204)$$

There is general agreement that the density limit disruptions are connected to a low m external kink mode. The intuition leading to this connection is as follows. Assume that a tokamak is operating with an edge safety factor sufficiently high that external MHD modes are not excited. As the density is raised, particularly in edge fueled tokamaks, a narrow turbulent boundary layer is formed just inside $r = a$ with high density and low temperature. The resistivity in this region becomes sufficiently high that very little current flows. Since the total current remains constant, it must now flow through a slightly smaller cross section since the edge region no longer carries current. A plasma with a fixed safety factor on axis due to the sawtooth limit, carrying the same current over a slightly smaller cross sectional area, has a correspondingly smaller safety factor at its effective edge.

As the density continues to increase the boundary region grows in width and the safety factor at the effective edge of the plasma core further decreases. Eventually the safety factor at the effective edge of the core falls below the critical value needed to avoid disruptions. Once this occurs the plasma does indeed suffer a major disruption.

While there is basic agreement on this qualitative description of density-driven disruptions, there is no first principles theory that explains why, and how much, the edge region grows as a function of increasing density. At least two possible explanations have been put forth. The first and earliest theory invokes a radiation collapse of the plasma edge. Here, line radiation due to impurities (proportional to $n_e n_Z$) increases rapidly with increasing density shifting the balance of plasma energy loss from thermal conduction to radiation. Eventually, all the energy loss is through radiation. Further increases in density cause the plasma to detach from the wall (or divertor plate). In other words, the plasma core shrinks in radius as it becomes surrounded by an increasingly growing radiation layer. This is just the situation that eventually leads to a major disruption as described above. The theory of the radiation collapse density limit has been derived in a simple but elegant calculation by Wesson (2011) and would seem, at least at first glance, to explain the experimental observations.

However, a closer look at an ever increasing amount of data raises some serious doubts that the radiation collapse is the primary explanation for the density limit. There are two basic problems. First, if line radiation is the dominant loss mechanism then one would expect the density limit to depend directly upon the type of impurity in the edge and its corresponding charge state Z. This dependence is not

observed experimentally. Second, the calculation of the density limit depends upon the amount of energy lost from the plasma core which in turn depends on the core thermal conductivity κ. Now, assume that κ is a free quantity chosen so that the resulting density limit coincides with the Greenwald limit. The value and scaling of κ also do not agree with experimental measurements. Therefore, while the radiation collapse mechanism may play a role in the setting the density limit, it would appear to not be the major role.

This leads to a second possible explanation for development and growth of an edge boundary layer (Greenwald, 2002). The explanation again depends on the fact that the edge temperature becomes progressively smaller as the density increases. At low temperatures the edge behaves more like a collision dominated fluid than a collisionless kinetic plasma. Certain collision dominated MHD plasma instabilities driven by the pressure gradient and unfavorable curvature (e.g., resistive ballooning modes) can become noticeably stronger than the collisionless drift wave instabilities that dominate core turbulence, thereby leading to a region of enhanced transport near the plasma edge. It is this enhanced transport that quenches the edge plasma current, forcing it into a smaller core region. One again has a situation where increasing density and lower temperature shrink the plasma core, thus lowering q_a, and eventually leading to a major disruption.

A simple model problem is described below showing how this behavior can occur. The end result is a demonstration of how edge turbulence produces a density limit. However, it is not possible to actually reproduce the Greenwald limit since this would require a detailed knowledge of the anomalous thermal diffusivities in the core and edge regions which at present are not well known from a first principles theory. Still the analysis does provide some intuition into the basic nature of the density limit.

A model problem for a turbulence-driven density limit

The model problem discussed below separates the plasma into two regions, the main core and the turbulent edge boundary layer (see Fig. 11.38). The core is characterized by a thermal conductivity κ_1 which itself may be anomalous. Similarly the edge is characterized by a strongly MHD turbulent conductivity κ_2. Two assumptions are made. First, the edge turbulence is much larger than the core turbulence: $\kappa_2 \gg \kappa_1$. Second, as a result of localized MHD instabilities, the edge turbulence is assumed to be generated when the pressure gradient exceeds a critical value; that is, edge turbulence occurs when $p'(r)/p'_C > 1$. Here, both $p'(r)$ and p'_C are negative and for mathematical simplicity the critical gradient p'_C is assumed to be a constant.

The basic equation to be solved in each region corresponds to steady state conservation of energy, which for the straight tokamak is given by
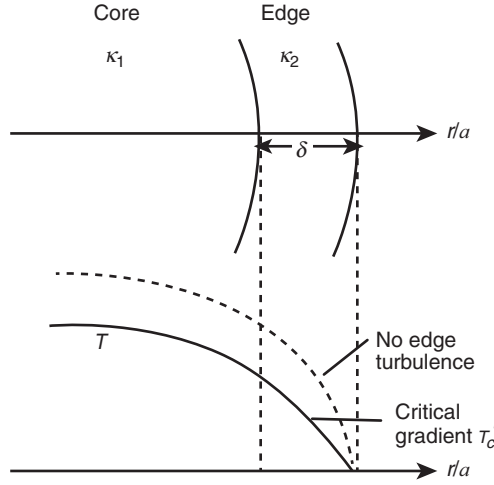
Figure 11.38   Edge geometry for the turbulence-driven density limit model.

$$\frac{1}{r}\frac{d}{dr}\left(\kappa\frac{dT}{dr}\right) + S = 0 \tag{11.205}$$

For mathematical simplicity the heating source S and plasma density n are both assumed to be constant across the entire plasma. The constant density assumption implies that edge turbulence occurs when $T'(r)/T'_C > 1$ with $T'_C = p'_C/n = \text{constant}$.

In the core and edge regions, denoted by the subscripts "1" and "2" respectively, the thermal conductivities, in accordance with the above discussion, are given by

$$
\begin{aligned}
\kappa &= \kappa_1 & &\text{core region } T'/T'_C < 1 \\
\kappa &= \kappa_1 + \kappa_2\left(\frac{T'}{T'_C} - 1\right) & &\text{edge region } T'/T'_C > 1
\end{aligned}
\tag{11.206}
$$

Here, κ_1 and κ_2 are both assumed to be constants, also for mathematical simplicity. Observe that there is a linear transition in κ as a function of $T'(r)$ from core transport to edge transport in the edge region.

The boundary conditions assume regularity at the origin and a perfect heat sink at the plasma edge,

$$
\begin{aligned}
T'_1(0) &= 0 \\
T_2(a) &= 0
\end{aligned}
\tag{11.207}
$$

Across the core–edge transition both the temperature and heat flux must be continuous. This transition is assumed to occur at a radius $r = r_\delta = a(1 - \delta)$, which leads to

$$[\![T]\!]_{r_\delta} = 0$$
$$[\![T']\!]_{r_\delta} = 0 \tag{11.208}$$

The value of δ is unknown. It is determined by the additional constraint that the temperature gradient at the transition radius r_δ actually be set equal to T'_C:

$$T'(r_\delta) = T'_C \tag{11.209}$$

The main goal of the analysis is in fact to calculate δ and show how it grows as n increases. When δ becomes sufficiently large the edge current forced into the core region lowers $q(r_\delta)$ sufficiently to cause a major disruption.

The problem has now been fully formulated and the solution is obtained as follows. Consider first the core region. The energy equation can be easily integrated and the solution satisfying the boundary condition at the origin can be written as

$$T_1(\rho) = \frac{a^2 S}{4\kappa_1}(1 - c_1 - \rho^2) \tag{11.210}$$

where $\rho = r/a$ and the free integration constant has, for convenience, been defined as $1 - c_1$. Note that when there is no edge turbulence then $c_1 = 0$ and the maximum temperature gradient occurs at the plasma edge. It has the value

$$a\frac{dT_1(a)}{dr} = -\frac{a^2 S}{2\kappa_1} \tag{11.211}$$

Equation (11.210) with $c_1 = 0$ is the correct solution for the entire plasma when the edge gradient is not steep enough to excite MHD edge turbulence. The interesting regime of the density limit occurs when this assumption is violated. In other words, edge turbulence is excited when

$$\zeta = \frac{aS}{2\kappa_1 \left| T'_C \right|} > 1 \tag{11.212}$$

If $\zeta > 1$ then one must calculate $T_2(r)$ in the edge region and match the solutions across the transition surface. A simple analytic solution can be obtained by assuming that the edge region is narrow. There is only a small region of edge turbulence where $\Delta = \kappa_1/\kappa_2 \ll 1$, which implies that $\delta \ll 1$ and $\zeta - 1 \ll 1$. Under these conditions, to a high degree of accuracy, the edge temperature profile simply tracks the marginally stable critical temperature gradient:

$$\frac{dT_2}{d\rho} \approx -a \left| T'_C \right| \tag{11.213}$$

The solution satisfying the edge boundary condition and the temperature gradient constraint at $r = r_\delta$ is given by

$$T_2(\rho) = a \left| T_C' \right| (1 - \rho) \tag{11.214}$$

The solutions now contain two unknown parameters: c_1, δ. These are determined by matching $T_1(\rho)$ and $dT_1(\rho)/d\rho$ across $r = r_\delta$ using the two jump conditions, i.e., Eq. (11.208). One finds

$$c_1 = 2\left(\zeta - 1\right)^2 \sim O\!\left(\delta^2\right)$$
$$\delta = (\zeta - 1)/\zeta \tag{11.215}$$

The last relation is the most important one. It demonstrates that as ζ increases above its marginal value of unity, the edge region becomes wider. The relation can be more conveniently expressed in terms of the safety factor and the density. Specifically, in the region $r_\delta < r < a$ the current density is negligible because of the strong turbulence. In this region $B_\theta \propto 1/r$ implying that the safety factor can be written as $q = q_a \rho^2$, where q_a is assumed to be sufficiently large so that without edge turbulence, external kink modes would not be excited.

However, the actual plasma edge where the current density vanishes occurs at $r_\delta = a(1 - \delta)$ and it is the safety factor at this radius that determines whether or not an external kink mode is excited. If the critical safety factor for external kinks is denoted by q_C, then the condition to avoid a disruption is given by $q(r_\delta) = q_a(1 - \delta)^2 > q_C$. Untangling the notation leads to the following condition to avoid external kink modes: $aS/2\kappa_1|T_C'| < q_a/q_C$. If one now recalls that the onset of edge turbulence arises from MHD modes then, as stated, the threshold gradient is really due to the pressure rather than the temperature. In other words, it is more accurate to write (for a constant density) $T_C' = p_C'/n$. The end result is that the condition to avoid external kink modes, and by inference major disruptions, has the form of a density limit that can be written as

$$n < \frac{2\kappa_1 p_C'}{aS} \left(\frac{q_a}{q_C}\right)^{1/2} \tag{11.216}$$

Interestingly, when $\kappa_2 \gg \kappa_1$ the density limit is predicted to be independent of the details of the edge turbulence and depends only on the core turbulence.

Finally, it is worth emphasizing that the density limit derived above arises from a simple model calculation. While the scaling information may be qualitatively correct it is still an incomplete calculation. The reason is that p_C' is a function of ε and q_a while κ_1 is at present still only a marginally known function of T, n, B, S, ε, q_a which depends on the nature of the core turbulence. A more accurate knowledge

of turbulent core transport is needed before closing the analysis to see whether Eq. (11.216) does indeed reduce to the Greenwald limit. Still, the calculation does show how a major disruption can be initiated when the density becomes too large.

11.6.5 *Resistive wall modes – external low* m *modes*

The analysis of external low m modes has shown that the current and density must be kept sufficiently small in order to avoid major disruptions. A question then arises as to whether the critical values can be increased (a favorable result) by the presence of a perfectly conducting wall. Of course, if improved stability is possible then the original no-wall instabilities would reappear in the form of resistive wall modes. However, it will be optimistically assumed that resistive wall modes can be stabilized by feedback and/or rotation. The issue then is to determine the effect of a perfectly conducting wall on external kink modes and see how large an improvement can be realized.

The calculation is straightforward but the results are mixed – some favorable and some unfavorable. The required information is easily obtained from the straight tokamak Energy Principle given by Eq. (11.189), generalized to include the effect of a perfectly conducting wall as presented in Eq. (11.172). The generalized relation is given by

$$
\delta \hat{W}_2 = \frac{1}{m^2 q_a^2}(nq_a - m)\left[(nq_a + m) + \left(m\Lambda + \frac{a\xi_a'}{\xi_a}\right)(nq_a - m)\right]a^2\xi_a^2
$$

$$
\Lambda \approx \frac{1 + (a/b)^{2m}}{1 - (a/b)^{2m}}
$$

$$
\tag{11.217}
$$

The required information is obtained by rewriting Eq. (11.217) as follows:

$$
\delta \hat{W}_2 = \frac{m\Lambda + 1 + a\xi_a'/\xi_a}{m^2 q_a^2}(nq_a - m)(nq_a - M_\infty - M_\Lambda) \tag{11.218}
$$

Here,

$$
M_\infty = m\left(\frac{m - 1 + a\xi_a'/\xi_a}{m + 1 + a\xi_a'/\xi_a}\right) \tag{11.219}
$$

is the critical value of nq_a with the wall at infinity and

$$
M_\Lambda = 2(\Lambda - 1)\frac{m^2}{\left(m + 1 + a\xi_a'/\xi_a\right)\left(m\Lambda + 1 + a\xi_a'/\xi_a\right)} \tag{11.220}
$$

is the modification due to a perfectly conducting wall at $r = b$.

As expected when the wall is at infinity (i.e., $\Lambda = 1$) then $M_\Lambda = 0$ leading to the no-wall stability boundary $nq_a = M_\infty$. Similarly, when the wall is on the plasma (i.e., $\Lambda = \infty$) then $M_\infty + M_\Lambda = m$ and the band of unstable q_a values shrinks to zero – the plasma is stable. Now, keeping in mind that $a\xi_a'/\xi_a$ is always positive, it follows that for the general case a band of unstable q_a values exists between

$$M_\infty + M_\Lambda < nq_a < m \tag{11.221}$$

What conclusions can be drawn from this result? There are two. First, the upper limit on the unstable band, $nq_a = m$, is unaffected by the presence of a conducting wall. This is an unfavorable result in that the maximum allowable current before the onset of external current-driven kink modes is unchanged by a conducting wall. Second, since $M_\Lambda > 0$ the lower limit on the unstable band, $nq_a = M_\infty + M_\Lambda$ has increased over the no-wall value $nq_a = M_\infty$. That is, the width of the unstable band has narrowed, which is a favorable result.

It is disappointing that a conducting wall does not allow a higher maximum current. However, the wall does have a stronger positive effect on the maximum allowable pressure but this requires the inclusion of toroidal effects in the analysis, which are obviously not included in the straight tokamak model.

11.6.6 Edge localized modes (ELMs) – external high m modes

The final topic of interest concerns external high m external kink modes. These modes typically occur during H-mode operation of a tokamak. This regime is characterized by improved energy confinement, clearly an advantage. However, an H-mode tokamak also has substantial edge gradients, which can drive high m MHD instabilities, known as "edge localized modes" or "ELMs" for short. Typically the unstable modes have $n \sim 10$, $m \sim 30$. Pressure, density, temperature, and current profiles exhibiting H-mode edge pedestals are illustrated in Fig. 11.39 (Hughes *et al.*, 2013).

ELMs are believed to be driven by a combination of large edge pressure gradients and large edge current gradients; the resulting instability is sometimes referred to as a peeling–ballooning mode (Snyder *et al.*, 2005). A complete description requires a toroidal calculation including pressure effects. The straight tokamak model provides a basic description of the peeling component of the mode which is driven by the edge current gradient. The analysis shows that large edge current gradients can indeed excite high m external kink modes, but it does not predict which particular m values are the most dangerous. This requires the inclusion of pressure-driven ballooning effects which are described in the next chapter.
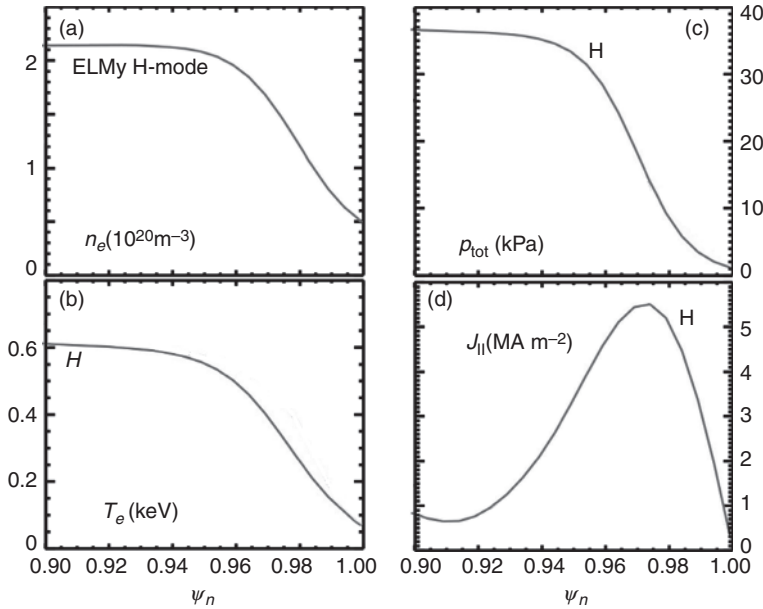
Figure 11.39 Experimental profiles of density, temperature, pressure, and current density profiles in an H-mode discharge showing edge pedestals (reproduced with permission from Hughes *et al.*, 2013).

The specific goal of the present subsection is to derive the stability windows in q_a space for high m modes driven by large edge current gradients neglecting all pressure effects. Following the derivation is an experimental description of the impact of ELMs on present and future tokamaks.

Stability of the constant current density tokamak (reference case)

Stability boundaries for high m external kink modes are again determined by the straight tokamak stability equation given by Eq. (11.189) with the minimizing ξ satisfying Eq. (11.188). These equations (for $\Lambda = 1$) are repeated here for convenience:

$$\delta \hat{W}_2 = \frac{1}{m^2 q_a^2} (nq_a - m) \left[(nq_a + m) + \left(m + \frac{a\xi'_a}{\xi_a} \right)(nq_a - m) \right] a^2 \xi_a^2$$

$$\frac{d}{dr} \left[r^3 \left(\frac{n}{m} - \frac{1}{q_a} \right)^2 \frac{d\xi}{dr} \right] - (m^2 - 1) r \left(\frac{n}{m} - \frac{1}{q_a} \right)^2 \xi = 0 \qquad (11.222)$$

The stability analysis considers a sequence of current density profiles. At one end of the sequence is a profile that is flat across the plasma with a finite jump at the
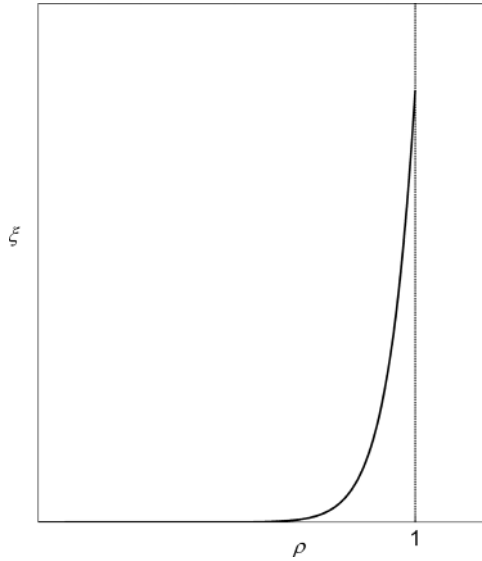
Figure 11.40   Curve of $\xi(r) = \xi(a)(r/a)^{m-1}$ vs. r for $m = 10$. Note the localization of the eigenfunction near the plasma edge. Here, $\rho = r/a$.

plasma edge. This is the reference case already analyzed in Section 11.6.3. As the sequence progresses the current density becomes more peaked but still has a finite jump at the edge. At the end of the sequence, the current density vanishes at the plasma edge but has a finite gradient.

The stability results for the reference case are given by Eq. (11.193), which shows that the condition for instability is given by

$$m - 1 < nq_a < m \tag{11.223}$$

As previously stated, Eq. (11.223) is a very pessimistic result because by setting $n = 1$ and continuously incrementing m by unity, one sees that the plasma is unstable over the entire range $0 \leq q_a \leq \infty$.

Observe that for high m the eigenfunctions are strongly localized around the plasma surface. This can be seen intuitively by noting that the eigenfunctions behave approximately like

$$\xi(r) \sim r^{m-1} \tag{11.224}$$

over the body of the plasma. A curve of $\xi(r) = \xi(a)(r/a)^{m-1}$ is illustrated in Fig. 11.40 for the case $m = 10$. The conclusion is that because of the localization, a conducting wall some distance away will not have any significant impact, thereby justifying the approximation of setting the wall parameter $\Lambda = 1$ in Eq. (11.222).

The consequence of this behavior is that the integral contribution to $\delta \hat{W}_2$ depends sensitively on the local behavior of $J(r)$ near $r = a$. In particular, as shown below, as $J(a)$ and $J'(a)$ become smaller the unstable regions diminish in size.

The high m *stability equation*

A quantitative analysis, which determines the stability boundaries in q_a space for large m has been given by Laval and Pellat (1973) and Laval *et al*. (1974). They investigated high m external kink mode stability in circular and non-circular tokamaks. For present purposes it suffices to outline their theory for the circular case.

The analysis begins by introducing a new dependent variable $\psi(r)$ into the equation for $\xi(r)$ contained in Eq. (11.222). The variable $\psi(r)$ is defined by

$$
\begin{aligned}
\psi &= K\xi \\
K(r) &= r^{3/2}\left(\frac{n}{m} - \frac{1}{q}\right)
\end{aligned}
\tag{11.225}
$$

Substituting into Eq. (11.222) yields

$$
\frac{d^2\psi}{dr^2} - \left(\frac{m^2 - 1}{r^2} + \frac{1}{K}\frac{d^2K}{dr^2}\right)\psi = 0
\tag{11.226}
$$

The next step is to expand Eq. (11.226) near the plasma surface assuming that $m \gg 1$. To do this, one writes

$$
\frac{r}{a} = 1 - \frac{x}{2m}
\tag{11.227}
$$

where $x > 0$ is the new independent variable. Localization of the mode requires that x be ordered as $x \sim 1$. Similarly if the resonant surface is just outside the edge of the plasma then its location must be ordered so that $1 - nq_a/m \sim 1/m$. Under these assumptions the function $K(r)$ can be expanded as

$$
K = K_1 + K_2 + \cdots
\tag{11.228}
$$

Here, $K_m \sim 1/m$ with

$$
\begin{aligned}
K_1 &= \frac{a^{3/2}}{2q_a m}\left[2(nq_a - m) - \frac{aq'_a}{q_a}x\right] \\
K_2 &= \frac{a^{3/2}}{8q_a m^2}\left[6(nq_a - m)x + \left(\frac{a^2 q''_a}{q_a} - 2\frac{a^2 q'^2_a}{q^2_a} + 3\frac{aq'_a}{q^2_a}\right)x^2\right]
\end{aligned}
\tag{11.229}
$$

and prime denoting d/dr. These complicated expressions can be simplified by rewriting them in terms of the edge current density J_a and its gradient J'_a. A short calculation yields

$$K_1 = \frac{a^{3/2}}{q_a m}\left[nq_a - m - \left(1 - \frac{J_a}{\overline{J}}\right)x\right]$$

$$K_2 = \frac{a^{3/2}}{4q_a m^2}\left[3(nq_a - m)x - \frac{aJ'_a}{\overline{J}}x^2\right] \tag{11.230}$$

The quantity $\overline{J}$ is the average current density defined by $\overline{J} = I/\pi a^2 = 2B_{\theta a}/\mu_0 a$.

Next, these expressions are substituted into the term K''/K. A short calculation leads to the desired equation for ψ valid in the limit of large m,

$$\frac{d^2\psi}{dx^2} - \left[\frac{1}{4} - \frac{\lambda}{m(x + x_0)}\right]\psi = 0$$

$$\lambda = -\frac{1}{2}\frac{aJ'_a}{\overline{J} - J_a} \tag{11.231}$$

$$x_0 = (m - nq_a)\frac{\overline{J}}{\overline{J} - J_a}$$

Both λ and x_0 are positive and of order unity which might lead one to believe that the $\lambda/m(x + x_0)$ term should be negligible in the limit of large m. This is sometimes true but as is shown shortly subtleties arise when $J_a = 0$.

Assume now that Eq. (11.231) can be solved for $\psi(x)$. Then, the last step in the formulation is to substitute this solution into the expression for $\delta\hat{W}_2$ given by Eq. (11.222). After a short calculation the resulting expression can be written, to lowest order in $1/m$, directly in terms of $\psi(x)$ as follows:

$$\delta\hat{W}_2 = \frac{1}{mq_a^2}(m - nq_a)\left[(m - nq_a)\left(1 - \frac{2}{\psi}\frac{d\psi}{dx}\right) - 2\frac{J_a}{\overline{J}}\right]a^2\xi_a^2 \tag{11.232}$$

where ψ and $d\psi/dx$ are evaluated at the plasma surface $x = 0$. Also, for an external mode $m - nq_a > 0$.

Stability for $J_a \neq 0$

The stability analysis separates into two cases depending on whether or not J_a vanishes. Consider first the case where $J(r)$ is a decreasing function of r which, however, still has a finite jump at $r = a$: $J_a \neq 0$. For such profiles it is only necessary to calculate the leading-order contribution to $\psi(x)$ from Eq. (11.231). In other words, the λ term can be neglected. The solution that
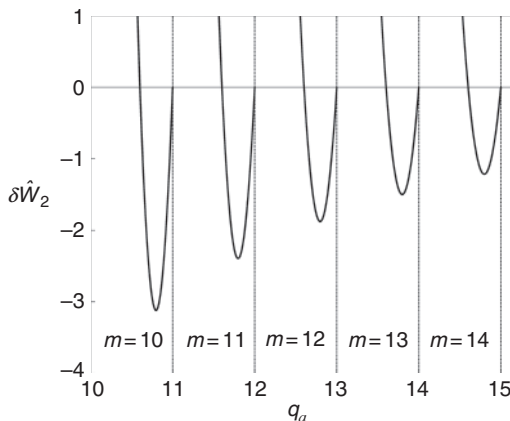
Figure 11.41 Plot of $\delta\hat{W}$ vs. q_a for high m and $n = 1$. Note the bands of instability, which are all of fixed width.

corresponds to a localized eigenfunction (i.e., the one that decays to zero as $x \to \infty$) is given by

$$\psi(x) = e^{-x/2}$$

$$\frac{d\psi(x)}{dx} = -\frac{1}{2}e^{-x/2} \tag{11.233}$$

$$\frac{1}{\psi}\frac{d\psi}{dx}\bigg|_0 = -\frac{1}{2}$$

Thus, the value of $\delta\hat{W}_2$ reduces to

$$\delta\hat{W}_2 = \frac{1}{mq_a^2}(m - nq_a)\left(m - \frac{J_a}{\overline{J}} - nq_a\right)a^2\xi_a^2 \tag{11.234}$$

Equation (11.234) predicts that high m external kink modes are unstable for q_a in the range

$$m - \frac{J_a}{\overline{J}} < nq_a < m \tag{11.235}$$

Any current profile with a finite jump at the plasma surface is unstable. The bands of instability are illustrated in Fig. 11.41. Note that their width remains constant as m increases. The most unstable case corresponds to a uniform current density, $J_a = \overline{J}$, in which case the neighboring bands touch and all q_a values are unstable. As the edge current density decreases the bands become narrower, forming windows of stability. Still, the overall conclusion is that, for a plasma with a finite $J(a)$, there is no minimum value of q_a above which the plasma is stable against high m external kink modes. As stated, stable plasmas do not want to have edge current density jumps.

Stability for $J_a = 0$

Equation (11.235) suggests that when the jump in edge current density vanishes (i.e., $J_a = 0$) the bands of instability shrink to zero and the plasma becomes stable. This is not quite the situation. As $J_a \to 0$ and $nq_a \to m$, the result is $\delta\hat{W}_2 \to 0$ corresponding to marginal stability. To determine the actual stability boundary requires the evaluation of the $1/m$ corrections to $\psi(x)$ resulting from the λ term. In fact, an examination of Eq. (11.232) indicates that these "corrections" must be finite for instabilities to exist. Specifically, one sees that when $J_a = 0$, $\delta\hat{W}_2$ reduces to

$$\delta\hat{W}_2 = \frac{1}{mq_a^2}(m - nq_a)^2\left(1 - \frac{2}{\psi}\frac{d\psi}{dx}\right)a^2\xi_a^2 \qquad (11.236)$$

implying that the condition determining the lower critical q_a for each band of instabilities is $\psi_x/\psi > 1/2$. The corrections to ψ must somehow change ψ_x/ψ a finite amount, from $-1/2$ to approximately $+1/2$.

The structure of Eq. (11.231) is such that a finite correction to ψ from the λ term is only possible if x_0 is even smaller than assumed; that is, one must alter the assumption $x_0 \sim 1$ to $x_0 \ll 1$. In this case the solution near $x = 0$ is strongly modified, possibly leading to a finite correction in ψ_x/ψ. Physically, the condition $x_0 \ll 1$ corresponds to the requirement that the resonant surface be extremely close to the plasma surface: the original ordering $1 - nq_a/m \sim 1/m$ must change to $1 - nq_a/m \ll 1/m$.

With this mathematical insight one can solve for $\psi(x)$ in Eq. (11.231) as follows. The solution for ψ including the λ term can be written in terms of Whittaker functions. As usual there are two independent solutions since Eq. (11.231) is a second-order ordinary differential equation. The localized solution (i.e., the one that decays to zero as $x \to \infty$) is given by (Gradshteyn and Ryzhik, 2000)

$$\psi(x) = W_{\lambda,\,1/2}(x + x_0) \qquad (11.237)$$

Now, to determine the stability boundary one needs to evaluate ψ_x/ψ at $x = 0$. Since the regime of interest corresponds to $x_0 \ll 1$ one can make use of the small argument expansion of the Whittaker function: $W_{\lambda,\,1/2}(x_0) \approx e^{-x_0/2}[1 - (\lambda/m)x_0 \ln x_0]$. A simple calculation then shows that the condition for instability can be written as

$$1 + \frac{\lambda}{m}\ln x_0 < 0 \qquad (11.238)$$

In terms of the standard notation, this leads to the following band of instabilities:

$$m - \exp\left(\frac{2m\overline{J}}{aJ_a'}\right) < nq_a < m \qquad (11.239)$$

After this rather complicated analysis one sees that instabilities can exist within exponentially narrow bands just below each rational surface. The calculation explicitly demonstrates the sensitivity of the stability boundaries to the behavior of the edge current density. The basic conclusion is that current density profiles which vanish at the plasma edge but have sharp edge gradients can be unstable to high m external kink modes. These modes serve as the peeling component of the peeling–ballooning modes responsible for ELMs. The ballooning component is described in the next chapter.

ELMs

The final topic of interest involves the impact of ELMs on experimental tokamak operation. As stated, ELMs appear in tokamaks operating in the favorable H-mode confinement regime, characterized by high edge pressure and current gradients. Experimentally, ELMS appear as short, periodic, bursts of particles and energy that are ejected from the plasma. In terms of overall performance ELMs are a mixed blessing in present day experiments but whose downside becomes much more serious in reactor scale devices. The issues are as follows.

On the positive side each ELM ejects impurities in addition to plasma particles. Preventing the build-up of impurities improves performance in present experiments and is crucial in reactor plasmas where they can dilute the basic D-T fuel. On the negative side the loss of plasma from too many ELMs reduces the time-averaged particle density and temperature, thereby degrading the overall high confinement properties of H-mode operation.

Equally importantly, while the divertor plates are designed to withstand the time-averaged heat loads resulting from thermal conduction losses, each ELM deposits a short, high-intensity, pulse of heat to the divertor plate. In other words, the heat deposition is not constant in time but has short, high-intensity pulses superimposed over the steady thermal conduction losses. Present experiments can withstand these bursts of heat but reactor scale devices would likely suffer irreversible damage to the divertor plate, clearly an unacceptable situation.

The situation is further complicated by the fact that there are different types of ELMs whose positive and negative contributions to tokamak operation vary in relative size. Type I ELMs are short in duration, well-spaced in time, but very intense in magnitude. These ELMs do not significantly degrade the H-mode confinement properties but would be unacceptable in reactor scale devices because of the high intensity of the pulses.

Type III ELMs lie on the other end of the spectrum. They occur frequently, almost continuously, and have low intensity. Consequently, they do not pose

much of a threat to the divertor plates. However, because of the nearly continuous ejection of particles and energy, Type III ELMs substantially degrade confinement performance, thus reducing the hoped-for benefits of H-mode operation.

Type II ELMs perhaps represent the best of both worlds. They are less intense than Type I ELMs but less frequent than Type III ELMs. As a result they do not significantly degrade performance, do not seriously threaten the divertor plates, and still help prevent impurity build-up in the plasma. The biggest difficulty with Type II ELMs is that they exist only over a relatively narrow range of parameters; that is, reliable accessibility to the Type II ELM regime of operation is not an easy task experimentally.

In terms of theory, the causes and properties of ELMs is an important and ongoing topic of research. Substantial progress has been made (Snyder *et al.*, 2005) but further research is still needed. One problem is that while the theory has made excellent progress in the understanding of ELMs, the theory does not in general offer sharply defined experimental techniques to control their behavior. The reason is that the theoretical understanding depends strongly on the properties of the edge region (e.g., turbulent transport, current, and edge gradients), which are difficult to measure and control experimentally.

One suggestion has been to apply resonant magnetic perturbations (RMPs) at the edge of the plasma to afford some level of external control over ELM behavior. This is still a work in progress. Another experimental regime of operation, noted as the I-mode (for "intermediate" mode), has been discovered (Whyte *et al.*, 2010) that is characterized by a high edge temperature gradient but without a high edge density gradient. In the I-mode regime energy confinement is very close to the desirable H-mode confinement, there is very little build-up of impurities, and operation is ELM free so there is no threat to the divertor plates. This appears to be a new and highly desirable regime of operation. Further research is needed to test the reliability and robustness of I-mode operation in different tokamaks operating over longer periods of time.

Clearly, ELMs represent an important operational limit on tokamaks. The straight tokamak model helps to shed some insight on the peeling component of the peeling–ballooning modes which are thought to be the basic driving instabilities for the generation of ELMs.

11.6.7 Summary of the straight tokamak

The straight tokamak model provides a simple but surprisingly reliable description of the basic MHD instabilities that can arise in a large aspect ratio, circular cross section, low-pressure tokamak. The model accurately describes instabilities that

arise from too much plasma current or too sharp an edge current density gradient. The tokamak ordering used to define the model leads to a description in which the pressure is negligible and in fact is entirely absent from the analysis. This is actually a benefit to the model in that when pressure effects are included in a straight model they are inaccurate in describing the actual situation. An accurate description of pressure effects requires a toroidal analysis which is presented in the next chapter.

In spite of its simplicity, the straight tokamak model describes MHD instabilities that are the important drives for many practical tokamak operational limits. These are summarized below:

- **Sawtooth oscillations:** The $m = 1$, $n = 1$ internal mode requires $q_0 > 1$ to avoid instability. When $q_0 < 1$ the internal relaxation instability known as the sawtooth oscillation is excited.

- **Current-driven disruptions:** When a plasma has too much current then external current-driven kinks can be excited which lead to major disruptions. The robust $m = 1$, $n = 1$ external Kruskal–Shafranov kink mode requires $q_a > 1$ for stability. Practically, depending on the steepness of the edge current density gradient, one finds that $q_a \sim 2-3$ is needed to avoid external kink instabilities and major disruptions.

- **Density-driven disruptions:** When the plasma density becomes too large a turbulent edge layer is formed, possibly driven by MHD instabilities. This layer effectively shrinks the size of the core plasma lowering the edge q. When the layer becomes wide enough the effective edge q becomes sufficiently small that a current-driven disruption is excited.

- **Resistive wall modes:** When a perfectly conducting wall is moved closer to the plasma surface the bands of unstable q_a values decrease. However, the minimum q_a for complete stability to current-driven modes remains unchanged and it is only the lower values of q_a, which defines the lower edge of the unstable bands, that are increased. Thus, resistive wall stabilization has no impact on the maximum allowable plasma current.

- **ELMs:** ELMs are believed to be caused by peeling–ballooning modes which are driven by a combination of high edge current and pressure gradients. The straight tokamak model provides a simple description of the peeling component of the mode driven by the edge current density gradient. The model shows that bands of instability exist for high $n \sim 10$ modes whose width depends sensitively on the edge current density jump and gradient. The ballooning effect requires a toroidal calculation.

Overall the straight tokamak model provides a good introduction to the basic MHD instabilities that affect the operation of tokamak experiments.

11.7 The reversed field pinch (RFP)

The cylindrical screw pinch analysis provides an accurate description of the MHD stability of the RFP configuration, including internal and external modes driven by the current and/or the pressure gradient. The reason for the good accuracy is that all basic equilibrium quantities in an RFP are of the same order: $B_\theta^2 \sim B_z^2 \sim \mu_0 p$. Thus, when a toroidal RFP is straightened into a cylindrical configuration all of the resulting errors are small, of order ε^2. This is in contrast to the high β tokamak where the ordering $\mu_0 p \sim \varepsilon B_z^2$ leads to finite and important modifications when transforming from a cylinder to a torus.

The basic goal of this section is to learn how much current and pressure can be stably confined in an RFP. The answer actually involves a two-part analysis that treats both ideal and resistive MHD modes. Qualitatively, the first part investigates ways to stabilize ideal modes which, if allowed to exist, would lead to strong turbulence and unacceptably poor performance. Once ideal stability is achieved a second part to the analysis is required that examines ways to minimize the remaining weaker resistive MHD turbulence. This weaker turbulence leads to improved transport compared to that generated by ideal modes. However, if left unchecked resistive MHD turbulence still results in poorer transport than a comparably sized tokamak. Since the present textbook is focused on ideal MHD the important problem of resistive MHD turbulence will not be covered here.

The general conclusions from the ideal MHD analysis are as follows. An RFP can be theoretically completely stable against all internal MHD modes at high values of pressure and current: $\beta \sim 0.2$ and $q_a \sim 0.2$. However, the low edge safety factor causes the plasma to be unstable to a substantial number of external ideal kink modes with typical unstable wave numbers ranging from $1 < |n| < 1/\varepsilon$. A close fitting conducting wall with wall radius/plasma radius ~ 1.5 can in principle stabilize these modes, but as discussed they then transform into resistive wall modes. From a practical point of view stable operation requires feedback, a task once thought by many to be unfeasible because of technological complexity, but which has, nevertheless, actually been successfully demonstrated on several RFP experiments.

The analysis required to demonstrate these points involves the evaluation of the cylindrical δW for ideal MHD modes by means of a combination of trial functions and simple numerical calculations. While the mathematics is not overly complex, obtaining a simple, global view of RFP stability is somewhat complicated because of the large number of parameters that enter the analysis. Specifically the parameters describing the RFP and its stability include q_0, q_a, B_{za}/B_{z0}, β, ε, n, m. The situation is made more complicated by the facts that B_{za}/B_{z0} reverses sign, implying that both positive and negative n values can become unstable.

Indeed, a main goal of the present section is to organize the material in such a way that an overall picture of RFP stability can be obtained. This is accomplished by the following steps:

1. A new set of dimensionless parameters is introduced that is closely tied to experimental operation. These are intuitively simpler to understand and replace the more mathematical parameters characterizing the RFP equilibrium model given in Chapter 5.
2. It is shown at the outset that an RFP with zero current density at the plasma edge and without a B_z reversal is always unstable to an $m = 1$ mode. This result motivates the remainder of the analysis which considers only RFPs with a B_z reversal.
3. Based on the discussion in Section 11.5.3 attention is next focused on the $m = 0$ mode in the limit $k \to 0$. It is shown that stability against this mode sets a limit on β which turns out to be sufficiently large that it does not represent an important operational limit.
4. The main ideal stability limitations arise from the $m = 1$ mode. The first and simplest stability limit is due to Suydam's criterion. High values of critical β are possible but achieving them imposes important constraints on the pressure profile. Stable profiles are flat near the origin and have flat gradients near the plasma edge.
5. Interestingly, when Suydam's criterion is satisfied, then over the usual RFP operating range, ideal internal modes are also shown to be stable. Theoretically, the implication is that RFPs can be completely stable to all internal modes at high values of β.
6. In contrast to these optimistic predictions experimental RFPs usually do not operate at such high values of β. A theory proposed by Taylor helps to explain why practical values of β are much lower. Taylor's theory also sheds insight into the time evolution of the magnetic field profiles.
7. From the ideal MHD point of view the most dangerous instabilities in an RFP are $m = 1$ external modes. These modes are analyzed and shown to be unstable over a wide range of n values, even at $\beta = 0$. A conducting wall is needed for stability and a calculation is presented showing how close the wall must be to stabilize external modes at zero and finite β.

The ambitious set of calculations outlined above proceeds as follows.

11.7.1 Physical parameters describing an RFP

The analysis begins by introducing new, physically intuitive, dimensionless parameters into the model RFP equilibrium discussed in Chapter 5. The model profiles are repeated here for convenience:

$$\frac{2\mu_0 p}{B_{z0}^2} = \frac{2\mu_0 p_{\max}}{B_{z0}^2}\left(1-\rho^6\right)^3 = \frac{140\alpha_p}{81}\left(1-\rho^6\right)^3$$

$$\frac{B_z}{B_{z0}} = 1 - 2\alpha_z\rho^2 + \alpha_z\rho^4$$

$$\frac{B_\theta^2}{B_{z0}^2} = \frac{\alpha_p}{9}\left(35\rho^6 - 40\rho^{12} + 14\rho^{18}\right) + \frac{\alpha_z}{15}\left[30\rho^2 - 20(2\alpha_z+1)\rho^4 + 45\alpha_z\rho^6 - 12\alpha_z\rho^8\right]$$

$$\frac{a\mu_0 J_\theta}{B_{z0}} = 4\alpha_z\rho\left(1-\rho^2\right)$$

$$\frac{a\mu_0 J_z}{B_{z0}} = \frac{140\alpha_p}{9}\left(\frac{\rho B_{z0}}{B_\theta}\right)\rho^4(1-\rho^6)^2 + 4\alpha_z\left(\frac{\rho B_{z0}}{B_\theta}\right)\left(1-\rho^2\right)\left(1-2\alpha_z\rho^2 + \alpha_z\rho^4\right)$$

$$(11.240)$$

where $\rho = r/a$ and $\langle p \rangle = (81/140)p_{\max}$. Observe that the equilibrium is characterized by two dimensionless parameters α_p, α_z and the scale factor B_{z0}.

Consider first the scale factor B_{z0}. In typical RFP operation, a small uniform B_z bias field initially fills the plasma chamber before the current ramp-up. After the current reaches its peak value the B_z profile has changed substantially and is far from uniform. Thus, the value B_{z0} is not one that is easy to set or measure experimentally. Instead, since the toroidal flux, ψ_t, is reasonably well conserved during the current rise, it makes sense to normalize $B_z(\rho)$ by this quantity. Specifically, one defines $\langle B_z \rangle = \psi_t/\pi a^2$ and normalizes all magnetic fields to $\langle B_z \rangle$. For the model $B_z(\rho)$ in Eq. (11.240) it follows that the relation between $\langle B_z \rangle$ and B_{z0} is given by

$$\langle B_z \rangle = B_{z0}\left(\frac{3-2\alpha_z}{3}\right) \tag{11.241}$$

Using this relation it is possible to define three basic dimensionless parameters that describe the physical operation and performance of an RFP. The first measures how much the B_z field reverses at the edge of the plasma. Its definition is $\mathsf{F} = B_{za}/\langle B_z \rangle$. The second parameter is a measure of the total toroidal current flowing in the plasma and is defined by $\boldsymbol{\theta} = (\mu_0 I/2\pi a)/\langle B_z \rangle = B_{\theta a}/\langle B_z \rangle$. Note the different font that distinguishes F, $\boldsymbol{\theta}$ from F, θ which already appear in the analysis. The third parameter measures the average plasma pressure. Since $\beta \approx \beta_p$ for typical RFP operation a good definition for this parameter is $\beta_p = 2\mu_0\langle p \rangle/B_{\theta a}^2$.

On the basis of this discussion, all of the stability results presented in this section are expressed in terms of the three basic RFP parameters F, $\boldsymbol{\theta}$, β_p. By

using the basic definitions $\alpha_z = B_{za}/B_{z0}$, $\alpha_p = 2\mu_0 \langle p \rangle / B_{z0}^2$ plus Eq. (11.241) one can show after a short calculation that the physical parameters F, θ, β_p, expressed in terms of the mathematical parameters α_z, α_p, are given by

$$F = \frac{B_{za}}{\langle B_z \rangle} = 3 \left(\frac{1 - \alpha_z}{3 - 2\alpha_z} \right)$$

$$\theta = \frac{B_{\theta a}}{\langle B_z \rangle} = \left(\frac{3}{3 - 2\alpha_z} \right) \left[\alpha_p + \alpha_z (10 - 7\alpha_z)/15 \right]^{1/2}$$

$$\beta_p = \frac{2\mu_0 \langle p \rangle}{B_{\theta a}^2} = \frac{\alpha_p}{\alpha_p + \alpha_z (10 - 7\alpha_z)/15} \tag{11.242}$$

The goal of the analysis is to determine the maximum values of θ and β_p, plus the corresponding values of F, that are MHD stable for an RFP.

The last quantity of interest is the expression for the ideal MHD δW written in a form suitable for the RFP. This form is obtained directly from Eq. (11.98) and is written as

$$\frac{\delta W}{2\pi^2 R_0/\mu_0} = \delta \hat{W} = \int_0^1 (f \xi'^2 + g \xi^2) \, d\rho$$

$$+ B_{\theta a}^2 \left[\frac{\Lambda}{m} (nq + m)^2 + \frac{1}{\kappa_0^2 \rho^2} (n^2 q^2 - m^2) \right]_a \xi_a^2$$

$$f(\rho) = \frac{B_\theta^2}{\rho \kappa_0^2} (nq + m)^2 \tag{11.243}$$

$$g(\rho) = 2\mu_0 \frac{\kappa^2}{\kappa_0^2} p' + \frac{\kappa_0^2 \rho^2 - 1}{\kappa_0^2 \rho^2} \frac{B_\theta^2}{\rho} (nq + m)^2 + 2 \frac{\kappa^2}{\kappa_0^4} \frac{B_\theta^2}{\rho^3} (n^2 q^2 - m^2)$$

$$= \frac{\kappa^2}{\kappa_0^2} \left[2\mu_0 p' + \frac{3 + \kappa^2 \rho^2}{1 + \kappa^2 \rho^2} \frac{B_\theta^2}{\rho} (nq + 1) \left(nq - \frac{1 - \kappa^2 \rho^2}{3 + \kappa^2 \rho^2} \right) \right]$$

Here, $\rho = r/a$, $q(\rho) = \varepsilon \rho B_z / B_\theta$, $\kappa = ka = n\varepsilon$, $\kappa_0^2(\rho) = k_0^2 a^2 = n^2 \varepsilon^2 + m^2/\rho^2$, and prime denotes $d/d\rho$. Note that the RFP community defines n with the opposite sign as the tokamak community. Also the second form of $g(\rho)$ corresponds to the important case of $m = 1$.

The stage has now been set to investigate the stability of the RFP.

11.7.2 Instability of an RFP without a B_z reversal

There is a good reason why a reversal in B_z is required for high-performance MHD behavior in an RFP. Without a reversal the RFP is always unstable to an ideal
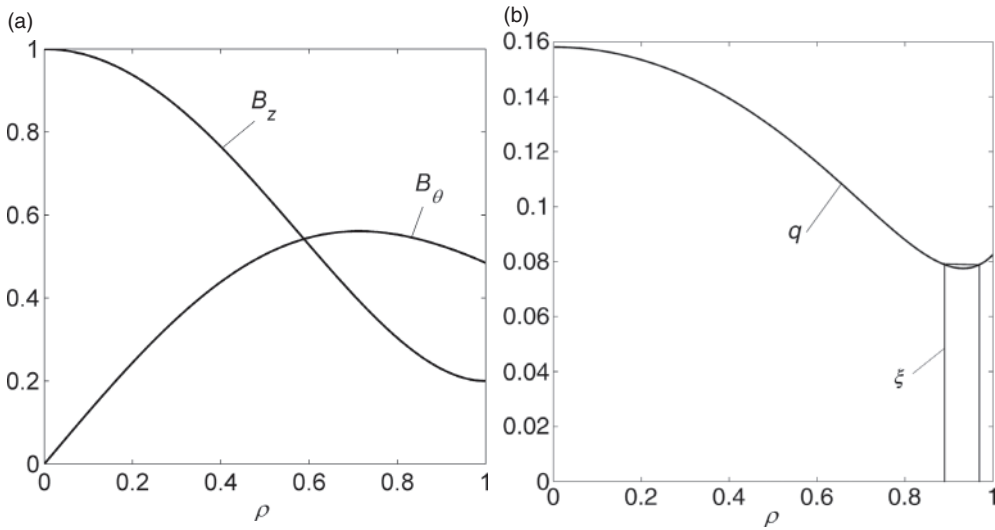
Figure 11.42   Profiles for an RFP without a B_z reversal: (a) $B_\theta(r)$ and $B_z(r)$; (b) $q(r)$ showing the existence of a minimum and the trial function leading to instability.

$m = 1$ instability near the outside of the plasma. The proof of this statement is presented below and is based on the generic shape of the $q(\rho)$ profile for a non-reversed RFP.

To determine the shape of the $q(\rho)$ profile assume that the current density and pressure gradient vanish at the edge of the plasma. The fields in this region are thus approximately vacuum fields (i.e., $B_z \approx B_{za} =$ constant and $B_\theta \approx B_{\theta a}/\rho$). This leads to a radially increasing safety factor profile $q \approx q_a \rho^2$. Now, near the axis of an RFP the $q(\rho)$ profile is a decreasing function of ρ. Without a reversal the only way these two constraints can be made compatible is for $q(\rho)$ to have a minimum as shown in Fig. 11.42.

Because of the minimum it is always possible to choose a trial function that makes $\delta W < 0$. This trial function is superimposed on the $q(\rho)$ profile, also shown in Fig. 11.42. The trial function corresponds to an $m = 1$ mode with n chosen so that $nq = -1$ at two neighboring points about the minimum in $q(\rho)$. Since $q \sim \varepsilon$ then $n \sim -1/\varepsilon$, a high value. Now, $f(\rho) = 0$ at the endpoints of the trial function where $\xi'(\rho) \to \infty$. Even so, the line bending contributions to $\delta \hat{W}$ vanish at both of these points in exact analogy with the sawtooth analysis of the tokamak (see Section 11.6.2). This trial function thus leads to an upper bound on $\delta \hat{W} = \delta \hat{W}_F$ given by

$$\delta \hat{W}_F = \xi_0^2 \int_{\rho_1}^{\rho_2} g(\rho) \, d\rho \qquad (11.244)$$

From the $m = 1$ expression for $g(\rho)$ given in Eq. (11.243) one sees that $p'(\rho) < 0$ and $-nq(\rho) < 1$ over the range $\rho_1 < \rho < \rho_2$. Similarly, one finds that

$$-nq + \frac{1 - \kappa^2\rho^2}{3 + \kappa^2\rho^2} = \frac{4}{3 + \kappa^2\rho^2} - nq - 1 \approx \frac{4}{3 + \kappa^2\rho^2} > 0 \qquad (11.245)$$

where the last approximation follows because of the smallness of $nq + 1$ near the minimum of $q(\rho)$.

The conclusion is that $g(\rho) < 0$ over the entire range of integration implying that $\delta\hat{W}_F < 0$; that is, a minimum in the $q(\rho)$ profile in an RFP leads to an $m = 1$ instability driven by both the pressure gradient and the current. This instability is not as "harmless" as the sawtooth instability in a tokamak. For the tokamak the instability redistributes energy and current near the center of the plasma. It does not lead to transport losses across the plasma boundary. However, the RFP instability is located near the edge of the plasma. Consequently, the redistribution of energy and current leads to transport losses across the plasma boundary to the wall, a very undesirable situation. Experimental observations indeed confirm this unfavorable prediction.

It is for this reason that good performance of an RFP requires a reversal in the $B_z(\rho)$ profile in order to eliminate the minimum in $q(\rho)$. The remainder of the analysis in this section focuses on profiles where $B_z(\rho)$ has a reversal. Such profiles motivate the name "reversed field pinch."

11.7.3 The m = 0 instability

An RFP can be unstable to an ideal $m = 0$ internal mode if β_p is too high. As shown below, however, the critical β_p is large and as such does not represent much of a constraint on RFP operation. A good estimate of the β_p limit can be obtained by the use of a simple trial function as illustrated in Fig. 11.43. The trial function ξ increases linearly with ρ near the origin as required by regularity. It continues to increase linearly until it drops abruptly to zero across a narrow layer at the radius ρ_0 where $B_z(\rho)$ reverses. Since $f(\rho_0) = 0$ for $m = 0$, the contribution to $\delta\hat{W}_F$ in the vicinity of $\rho = \rho_0$ from the $f\xi'^2$ term vanishes in analogy with the tokamak sawtooth analysis in Section 11.6.2.

The end result is that for the trial function $\xi = \xi_0(\rho/\rho_0)$ the value of $\delta\hat{W}_F$ reduces to

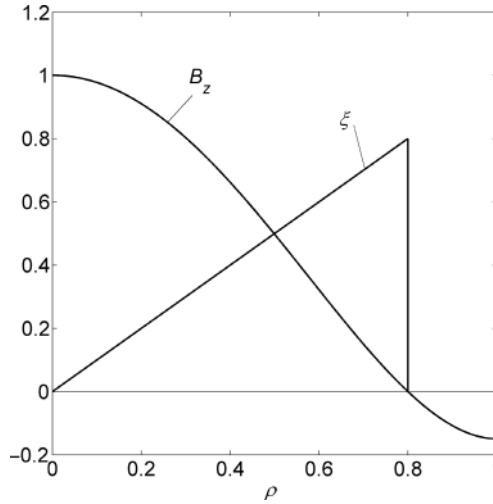$$\delta\hat{W}_F = \frac{\xi_0^2}{\rho_0^2} \int_0^{\rho_0} \left(f + \rho^2 g\right) d\rho \qquad (11.246)$$

Figure 11.43 Trial function for the $m = 0$ pressure-driven internal mode.

Now, as discussed in Section 11.5.3 the most unstable wave number for $m = 0$ corresponds to $n \propto k \to 0$. In this limit one sees from Eq. (11.243) that

$$f + \rho^2 g = 2\mu_0 \rho^2 p' + 2\rho B_z^2 \qquad (11.247)$$

Equation (11.247) is substituted into Eq. (11.246) which is then evaluated for the model RFP profile. The resulting $\delta \hat{W}_F$ is a function of ρ_0 and a numerical calculation shows that $\rho_0 \to 1$ is the most unstable case. In the $\rho_0 \to 1$ limit one finds that the stability boundary for the $m = 0$ mode in an RFP is given by

$$\beta_p < \frac{1}{2} \qquad (11.248)$$

Equation (11.248) is only a weak condition on RFP operation as most experiments operate considerably below this value. Physically, the stability limit is a consequence of the fact that there must be a sufficient B_z to "stiffen" the plasma against $m = 0$ sausage perturbations. As shown in Fig. 11.44 $m = 0$ perturbations compress both the plasma and the internal B_z field, each of which is a stabilizing effect against the unfavorable curvature. When B_z is too small, corresponding to $\beta_p > 1/2$, the RFP behaves similarly to a sausage-unstable Z-pinch.

11.7.4 Suydam's criterion

The next class of modes to examine corresponds to localized interchanges whose stability boundary is defined by Suydam's criterion. This involves a very easy-to-implement test, simply substituting the equilibrium profiles into Eq. (11.109) and
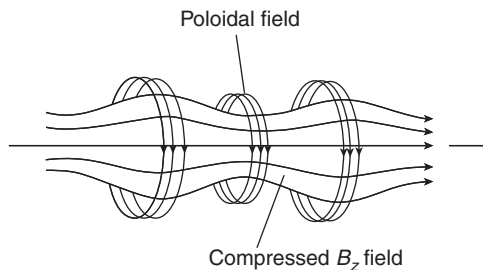
Figure 11.44 "Stiffening" of the plasma against $m = 0$ perturbations by an internal B_z field.

seeing whether or not the criterion is violated. An examination of the criterion shows that stability imposes two constraints on the shape of the pressure profile.

First, as previously discussed in Section 11.6.1, Suydam's stability criterion near the axis can be written for an RFP (in terms of normalized radius) as

$$\left(\frac{q_0''}{q_0}\right)^2 \rho^2 > -\frac{8\mu_0 p_0''}{B_{z0}^2} \tag{11.249}$$

Clearly, the criterion is violated near $\rho = 0$ unless $p_0'' \geq 0$. The implication is that the pressure profile must be very flat or hollow near the axis. Unlike the tokamak, toroidal effects do not improve the situation very much because of the small $q \sim \varepsilon$ in an RFP.

The second constraint involves the pressure gradient near the edge of the plasma for the realistic case where $p' = J_\theta = J_z = 0$ at $\rho = 1$. Suydam's criterion tends to be violated in this region for profiles where B_z is only slightly reversed. This can be seen explicitly by expanding Suydam's criterion about the edge. One sets $\rho = 1 - \delta$ with $\delta \ll 1$, uses the fact that $\rho q'/q = 2$ when $\mathbf{J} = 0$, and assumes that $B_{za}/B_{za}'' \sim \delta^2$. Suydam's criterion (for stability) reduces to

$$8\mu_0 p_a'' < B_{za}''^2 \frac{\left(\delta^2 + 2B_{za}/B_{za}''\right)^2}{\delta} \tag{11.250}$$

For typical RFP profiles, $B_{za} < 0$, $B_{za}'' > 0$, and $p_a'' > 0$. It thus follows that for such profiles the stability criterion is always violated at the radius corresponding to $\delta^2 = -2B_{za}/B_{za}''$. The way to avoid this instability is to require $p_a'' = 0$. In other words, the edge pressure gradient must be very flat.

The two constraints just discussed motivate the choice of pressure profile used in Eq. (11.240) to model an RFP. It is now a simple task to substitute the profiles into Suydam's criterion to determine the marginal stability boundary. A simple numerical evaluation leads to the marginal stability curve of β_p vs. θ as illustrated
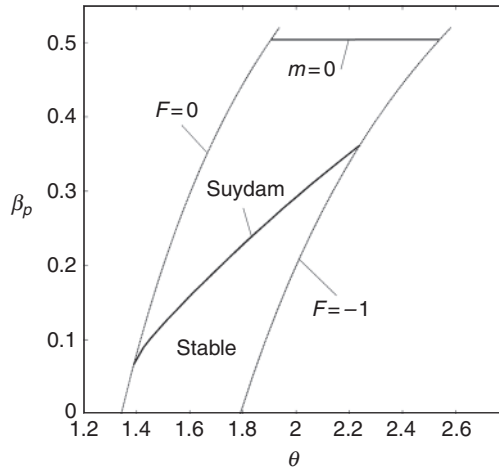
Figure 11.45   Marginal stability diagram of β_p vs. θ as determined by the Suydam criterion. The vertical boundaries correspond to the normal range of RFP operation $F = 0$ and $F = -1$. The regions below the heavier curves are stable.

in Fig. 11.45. In this figure the range of θ values corresponds to the usual RFP experimental operating regime $0 > F > -1$. The conclusion is that over the relevant range of θ the critical β_p can be substantial, ranging from 0.1 to 0.35. The Suydam limit for β_p is usually not the limiting factor in high-performance RFP operation.

11.7.5 Internal modes

Consider now the stability of an RFP against general ideal internal modes. Not much discussion is required. Stability is determined by numerically solving the minimizing equation for ξ given by

$$(f\xi')' - g\xi = 0 \qquad (11.251)$$

for the $m = 1$ mode using the model profiles. The numerical solutions are tested for stability against internal mode wave numbers that are resonant within the plasma either inside or outside the reversal radius. Following Newcomb's procedure the solutions between the origin and the resonant surface and between the plasma edge (where $\xi_a = 0$ for an internal mode) and the resonant surface are examined for the existence of a zero crossing. If such a crossing exists in either region the plasma is unstable.

   The results are quite simple. For the experimental range of F lying between $0 > F > -1$ the plasma is stable to all internal MHD modes up to the value of β_p

at which the Suydam criterion is violated. In other words the diagram given by Fig. 11.45 represents the complete stability of an RFP against all internal ideal MHD modes and includes the $m = 0$ mode, Suydam's criterion, and global internal modes. It is worth noting that global internal modes can be driven unstable at higher values of current where the plasma is more like a Z-pinch than an RFP. However, these larger currents lie outside the normal operating range of an RFP.

11.7.6 Taylor's theory

The analysis thus far presented has shown that high β RFP profiles exist that are MHD stable to all internal modes. These profiles are characterized by (1) a flat $p(r)$ profile near the origin and the plasma edge and (2) a $B_z(r)$ profile that reverses near the edge of the plasma. One can ask how such profiles were discovered and whether they are generated naturally or require sophisticated external field programming.

Historically, it was observed on the Zeta experiment (Bodin and Newton, 1980) that RFP-like profiles were formed by the natural evolution of ohmically heated discharges. These plasmas, however, were characterized by a high level of turbulence and, most importantly, did not have a $B_z(r)$ reversal. The MHD instabilities inherent in a non-reversed RFP, as discussed in Section 11.7.2, presumably played an important role in producing this poor behavior.

Even so, towards the end of Zeta's experimental operation, it was discovered that under certain conditions, after a turbulent initial phase, the plasma remarkably evolved to a stable quiescent state that included a spontaneous self-reversal of the $B_z(r)$ field. The reduction of turbulence in the quiescent state is illustrated in Fig. 11.46 for a later RFP, HBTX-1A at Culham Laboratory.

The reversal in $B_z(r)$ is quite interesting since no special field programming was utilized. Furthermore, as shown in the analysis below, reversed $B_z(r)$ profiles cannot be generated from a pure ohmically heated evolution. Instead, reversal requires the generation of a dynamo, driven by a relatively low level of turbulence (as compared to the non-reversed state). The low turbulence level helps to explain the improved transport but still causes the β value to be considerably lower than the maximum ideal MHD internal mode limit. An elegant theory explaining the evolution of RFP discharges and the conditions under which self-reversal occurs has been given by Taylor (1974) and is the main topic of this subsection.

The basic idea put forth by Taylor is as follows. Assume the existence of a slightly dissipative plasma surrounded by a perfectly conducting shell which is initially not in a state of stable equilibrium. As the plasma turbulently evolves from its initial state, perhaps violently, it dissipates energy through thermal and particle
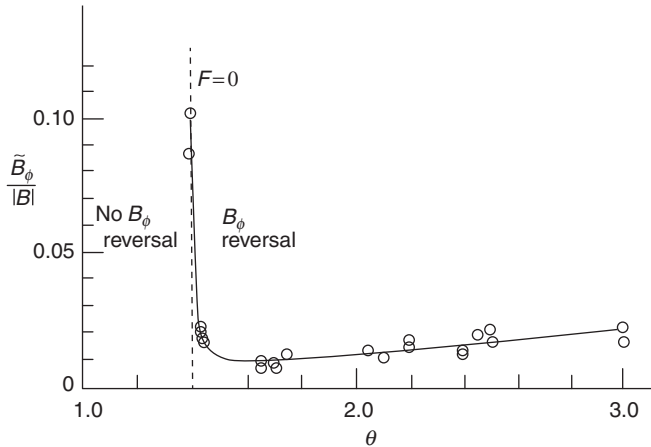
Figure 11.46 Experimental observations of B_θ fluctuations vs. $\theta \propto I$ in the HBTX-1A RFP at Culham Laboratory, UK. Experimentally, field reversal occurs at $\theta = 1.4$. Observe the low-fluctuation, quiescent operation for $\theta > 1.4$. Courtesy of I. Hutchinson.

losses to the wall. It continues to do so until it reaches a state of minimum energy after which it is incapable of further motion. The properties of the final state are determined by the constraints governing the evolution. Clearly the crucial physics issue, resolved by Taylor, is the determination of the appropriate constraints. Once the constraints are known it is relatively straightforward to obtain the final profiles. The presence of dissipation is critical as it allows accessibility to a much wider range of states than those that are accessible under the topological restrictions of ideal MHD.

Taylor's theory requires several steps which are described below after it is demonstrated that reversal cannot occur in a pure ohmically heated discharge.

Impossibility of $B_z(r)$ reversal in a pure ohmic discharge

A pure ohmic discharge is defined as a plasma that maintains exact 1-D cylindrical symmetry during its entire evolution. No instabilities are allowed that can generate multidimensional turbulence. The equations describing the 1-D evolution are given by the standard cylindrical MHD model, the only modification being in the parallel Ohm's law, which changes from $E_\parallel = 0$ to $E_\parallel = \eta J_\parallel$. Even though the resistivity is small and can be neglected in the perpendicular components of Ohm's law it must be kept in the parallel component since $E_\parallel$ is being compared to "zero."

The calculation begins by noting that Ampere's law combined with the definition $J_\parallel = \mathbf{J} \cdot \mathbf{B}/B$ leads to the relation

$$\mu_0 J_{\parallel}(r) = \frac{1}{B}\left[B_z \frac{(rB_\theta)'}{r} - B_\theta B_z'\right] \tag{11.252}$$

Now, assume that the profile is evolving on the slow (compared to ideal MHD) transport time scale implying that the plasma, at any instant of time, satisfies the steady state MHD equations; that is, the plasma is passing through a series of quasistatic equilibria. During this slow evolution it follows that $\nabla \times \mathbf{E} = -\partial\mathbf{B}/\partial t \approx 0$. The solution which is regular at the origin is given by $\mathbf{E} = E_0\mathbf{e}_z$. Here, $E_0(r, t) \approx E_0(t)$ is the toroidal electric field induced by the transformer. The parallel Ohm's law then yields a relation between $J_{\parallel}$ and E_0 given by

$$J_{\parallel}(r) = \frac{E_0}{\eta}\frac{B_z}{B} \tag{11.253}$$

Equation (11.253) is substituted into Eq. (11.252) and combined with the radial pressure balance relation. A short calculation yields

$$B_z' = -\frac{\mu_0}{B^2}\left(\frac{E_0 B_\theta}{\eta} + p'\right)B_z \tag{11.254}$$

This equation can be formally integrated leading to

$$B_z(r) = B_{z0}\exp\left[-\int_0^r \frac{\mu_0}{B^2}\left(\frac{E_0 B_\theta}{\eta} + p'\right)dr\right] \tag{11.255}$$

Clearly, the exponential behavior shows that a 1-D ohmic evolution can never lead to a reversal in $B_z(r)$.

Taylor's minimum energy formulation

Taylor suggested that as an RFP evolves in the presence of fine scale resistive turbulence, the plasma would naturally seek its lowest energy state. Mathematically, this is equivalent to the statement that the profiles must adjust themselves so as to minimize the total potential energy whose exact formula (see Eq. (3.24) with $v = 0$ corresponding to slow evolution) is given by

$$W = \int\left(\frac{B^2}{2\mu_0} + \frac{p}{\gamma - 1}\right)d\mathbf{r} \tag{11.256}$$

As stated, the key point in the analysis is to determine the appropriate constraints under which the minimization is to be carried out. Within the ideal MHD model it is shown below that there are an infinite number of constraints that can be applied. Taylor recognized that almost all of these constraints do not actually apply to a dissipative plasma. This recognition led him to suggest a much more plausible set

of constraints. The reasoning behind the final constraints is described below by first focusing on an ideal MHD plasma and then considering the consequences of dissipation.

The ideal MHD helicity constraints

The ideal MHD constraints start with the requirement that any physically acceptable magnetic field must obviously satisfy $\nabla \cdot \mathbf{B} = 0$. Most importantly, if the magnetic field is embedded in a perfectly conducting ideal MHD plasma then any evolution of $\mathbf{B}$ away from its initial state must be consistent with Faraday's law

$$\frac{\partial \mathbf{B}}{\partial t} = \nabla \times (\mathbf{v} \times \mathbf{B}) \tag{11.257}$$

In other words, magnetic field variations must result from physically allowable plasma displacements that exactly preserve the field line topology.

It has been shown (Woltjer, 1958) that the local constraint given by Eq. (11.257) can be replaced by an infinite set of integral constraints involving the helicity H which is defined as

$$H(\psi, t) = \int_\psi \mathbf{A} \cdot \mathbf{B} d\mathbf{r} \tag{11.258}$$

where $\mathbf{A}$ is the vector potential and the integration is carried out over the volume enclosed by an arbitrary flux surface ψ. This intuitive equivalence (i.e., one local constraint = infinite number of integral constraints) follows from the fact that in an ideal MHD plasma

$$\frac{dH}{dt} = 0 \tag{11.259}$$

on every flux surface. The conservation of helicity can be easily derived by noting that on any flux surface, which is allowed to move with a velocity $\mathbf{v}$ as time evolves,

$$\frac{dH}{dt} = \int_\psi \left(\mathbf{A} \cdot \frac{\partial \mathbf{B}}{\partial t} + \mathbf{B} \cdot \frac{\partial \mathbf{A}}{\partial t} \right) d\mathbf{r} + \int_{S_\psi} (\mathbf{A} \cdot \mathbf{B})(\mathbf{n} \cdot \mathbf{v}) dS \tag{11.260}$$

This expression is simplified by substituting $\partial \mathbf{B}/\partial t = -\nabla \times \mathbf{E}$ and $\partial \mathbf{A}/\partial t = -\mathbf{E} - \nabla \phi$. The $\nabla \phi$ term integrates to zero and the remaining terms can be written as

$$\frac{dH}{dt} = -\int_\psi [2\mathbf{E} \cdot \mathbf{B} + \nabla \cdot (\mathbf{E} \times \mathbf{A})] d\mathbf{r} + \int_{S_\psi} (\mathbf{A} \cdot \mathbf{B})(\mathbf{n} \cdot \mathbf{v}) dS \tag{11.261}$$

The divergence theorem is now applied to the $\mathbf{E} \times \mathbf{A}$ term. A short calculation yields

$$\frac{dH}{dt} = -2 \int_{\psi} \mathbf{E} \cdot \mathbf{B} \, d\mathbf{r} + \int_{S_{\psi}} (\mathbf{n} \times \mathbf{A}) \cdot (\mathbf{E} + \mathbf{v} \times \mathbf{B}) dS = 0 \qquad (11.262)$$

Clearly, helicity is conserved on every flux surface for a plasma that satisfies the ideal MHD Ohm's law.

Although the energy W can be minimized subject to conservation of H on every flux surface, the result, as pointed out by Taylor, is unrealistic for a plasma with dissipation. The presence of resistivity relaxes the ideal MHD requirement that field line topology be exactly conserved as the plasma evolves thereby providing access to a much wider class of lower energy states. This insight led Taylor to propose a much simpler set of constraints that govern the evolution of RFP plasmas. These are the next topic for discussion.

Taylor's constraints for a dissipative plasma

Since field line topology is not conserved in a dissipative plasma, Taylor reasoned that H would not be conserved on every flux surface. The continual tearing and reconnection of field lines in the presence of fine scale resistive MHD turbulence would destroy the identity of virtually all flux surfaces. He then made the crucial assumption that the only flux surface that would maintain its identity and corresponding helicity is the plasma boundary since it is assumed to be rigid and perfectly conducting; that is, if ψ_a is the total toroidal flux contained within the plasma then $H_a = H(\psi_a)$ is the only helicity that is conserved. Furthermore, because the boundary is perfectly conducting the toroidal flux

$$\psi_a = \int_0^{2\pi} d\theta \int_0^a B_z r dr \qquad (11.263)$$

is itself conserved.

To summarize, Taylor considered the evolution of an RFP plasma and postulated that the profiles at any instant of time would be determined by minimizing the potential energy subject to the constraints of fixed total helicity and fixed total toroidal flux. Mathematically, this is equivalent to minimizing W subject to the constraints of fixed H_a and fixed ψ_a. Implicit in the formulation are the assumptions that the evolution takes place on a time scale slow compared to the ideal MHD time but rapid compared to the time during which the plasma current changes. The plasma thus evolves through a sequence of minimum energy states each one characterized by a different value of the slowly changing current.

The minimum energy equations

The task now is to derive the governing equations obtained by minimizing W subject to the H_a and ψ_a constraints. The procedure is as follows. First, since the flux constraint involves a surface rather than a volume integral it is easily satisfied by a simple normalization procedure as demonstrated shortly. Second, the helicity constraint, which involves a volume integral, can be taken into account by a standard application of the method of Lagrange multipliers. Specifically, the minimum energy state is obtained by setting the variation of

$$W = \frac{1}{2\mu_0} \left[\int_P \left(B^2 + \frac{2\mu_0 p}{\gamma - 1} - \mu \mathbf{A} \cdot \mathbf{B} \right) d\mathbf{r} + \mu H_a \right] \tag{11.264}$$

to zero where μ is the Lagrange multiplier. In carrying out this step the variation of W with respect to $\mathbf{B}$, p and μ must each be set to zero.

As expected, the variation with respect to μ yields the original helicity constraint:

$$(\Delta W)_\mu = \frac{\delta \mu}{2\mu_0} \left(H_a - \int_P \mathbf{A} \cdot \mathbf{B} \, d\mathbf{r} \right) = 0 \tag{11.265}$$

The variation with respect to $\mathbf{B}$ and p can be written as

$$(\Delta W)_{\mathbf{B},p} = \frac{1}{2\mu_0} \int_P \left(2\mathbf{B} \cdot \delta \mathbf{B} + \frac{2\mu_0 \delta p}{\gamma - 1} - \mu \delta \mathbf{A} \cdot \mathbf{B} - \mu \mathbf{A} \cdot \delta \mathbf{B} \right) d\mathbf{r} = 0 \tag{11.266}$$

Two steps are required to reduce this expression to a useful simplified form. First, Taylor argues that the term involving δp can be set to zero independent of the variation in $\mathbf{B}$. The reasoning is that the continual tearing and reconnecting of field lines, coupled with an enormous parallel heat conductivity, allows the plasma pressure to redistribute and equalize itself so that $\nabla p = 0$ regardless of the variations in $\mathbf{B}$. This is obviously a pessimistic conclusion but is often closer than not to the realistic experimental situation. In practice the plasma pressure is non-zero since it is being driven by ohmic power. Even so, because of turbulent resistive MHD transport, the resulting ohmic pressure is considerably below the ideal MHD stability limit, the latter corresponding to a tight coupling between δp and $\delta \mathbf{B}$ through the adiabatic equation of state. For simplicity ohmic heating is neglected allowing one to apply Taylor's reasoning and set $\delta p \approx 0$.

Second, the remaining terms in the integral are simplified by noting that $\delta \mathbf{B} = \nabla \times \delta \mathbf{A}$. A short calculation leads to

$$(\Delta W)_{\mathbf{B},p} = \frac{1}{\mu_0} \int_P \delta \mathbf{A} \cdot (\nabla \times \mathbf{B} - \mu \mathbf{B}) \, d\mathbf{r} + \frac{1}{2\mu_0} \int_P \nabla \cdot [\delta \mathbf{A} \times (2\mathbf{B} - \mu \mathbf{A})] \, d\mathbf{r} = 0 \tag{11.267}$$

The divergence term is converted into a surface integral which then vanishes since $\mathbf{n} \times \delta\mathbf{A} = 0$ on the plasma surface. For the remaining integral to vanish for arbitrary $\delta\mathbf{A}$ requires that at each point in the plasma

$$\nabla \times \mathbf{B} = \mu\mathbf{B} \tag{11.268}$$

Equation (11.268) with μ a constant, is the desired relation that describes each minimum energy state during the evolution of the RFP plasma.

Mathematical solution for the cylindrically symmetric minimum energy state

The next step in the analysis is to solve for $\mathbf{B}$ and $\mathbf{A}$ assuming that μ is a constant. In general, multiple solutions exist to Eq. (11.268), each satisfying the same boundary conditions – the solution is not unique. For each solution the resulting $\mathbf{B}$ and $\mathbf{A}$ are used to evaluate $H_a(\mu)$ which when inverted determines $\mu = \mu(H_a)$. Substituting this value of μ into the expression for the potential energy allows one to calculate $W(H_a)$ for each solution. Taylor conjectures that the plasma should evolve to that particular state which has the lowest absolute value of W.

Presented below are the mathematical solutions to the minimum energy equation followed by a discussion of their application to experiment. In terms of the mathematics Taylor (1974) and Reiman (1980) have shown that only two of the many non-unique solutions can possibly have an absolute minimum in W. Of these two the one that produces the absolute minimum depends upon the actual value of H_a.

Qualitatively, the two possible minimum energy solutions correspond to (1) an $m = 0$ cylindrically symmetric state and (2) an $m = 0, 1$ mixed helical state. Consider first the $m = 0$ solution which is easily found by eliminating $B_\theta(r)$ from the θ component of Eq. (11.268) and substituting into the z component. The result is a differential equation for $B_z(r)$ given by

$$\frac{1}{r}\frac{d}{dr}\left(r\frac{dB_z}{dr}\right) + \mu^2 B_z = 0 \tag{11.269}$$

The solution for the fields can then be written as

$$\begin{aligned} B_z(r) &= B_{z0}J_0(\mu r) \\ B_\theta(r) &= B_{z0}J_1(\mu r) \end{aligned} \tag{11.270}$$

Here, J_0, J_1 are Bessel functions and B_{z0} is the toroidal field on axis. The quantity B_{z0} is directly related to the toroidal flux constraint. Specifically, in accordance with previous notation, B_{z0} is related to the normalized toroidal flux $\langle B_z \rangle \equiv \psi_a/\pi a^2$ by

$$\langle B_z \rangle = \frac{2}{a^2}\int_0^a B_z r\,dr = \left[\frac{2J_1(x)}{x}\right]B_{z0} \tag{11.271}$$

where $x = \mu a$. Note that B_z has a reversal when $x > 2.4$.

Using the fields given by Eq. (11.270) one can evaluate the potential energy from Eq. (11.256) after invoking the $p \approx 0$ approximation. After a straightforward calculation that makes use of various Bessel function identities (Gradshteyn and Ryzhik, 2000) one obtains

$$
\frac{W}{\overline{W}} \equiv W_0(x) = \frac{x^2}{J_1^2} \left(J_0^2 + J_1^2 - \frac{J_0 J_1}{x} \right)
$$
$$
\overline{W} = \frac{\pi^2 R_0 a^2}{2\mu_0} \langle B_z \rangle^2
$$
(11.272)

where the argument of the Bessel functions is x.

The next quantity to calculate is the helicity H_a. To do this requires an expression for $\mathbf{A}$. Since $\nabla \times \mathbf{B} = \mu \mathbf{B} = \mu \nabla \times \mathbf{A}$ it follows that $\mathbf{B} = \mu \mathbf{A} + \nabla \chi$ where χ is a free function. The gauge condition is chosen by the usual relation $\nabla \cdot \mathbf{A} = 0$ implying that $\nabla^2 \chi = 0$. It is important to determine χ since its value impacts the calculation of H_a.

The determination of χ is slightly subtle. A convenient procedure is to assume that the plasma evolves on a slowly varying time scale which then leads to a determination of χ by application of the condition $\mathbf{n} \times \mathbf{E} = 0$ on the perfectly conducting plasma boundary. The electric field can be expressed as

$$
\mathbf{E} = -\frac{\partial \mathbf{A}}{\partial t} - \nabla \phi = -\frac{\partial \mathbf{A}}{\partial t}
$$
(11.273)

The formulation now has two potential functions, χ and φ in addition to $\mathbf{A}$. Without loss in generality, one potential function can always be absorbed into $\mathbf{A}$. For present purposes it is convenient to absorb φ into $\mathbf{A}$, which is accomplished by introducing a scalar $U(\mathbf{r}, t)$ defined by $\partial U / \partial t = -\varphi$. One then sets $\mathbf{A} = \mathbf{A}' + \nabla U$ and $\chi = \chi' - \mu U$. After supressimg the primes, $\mathbf{B}$ has the same form as initially assumed and $\mathbf{E}$ reduces to the second form in Eq. (11.273).

In general the solutions for $\mathbf{E}$, $\mathbf{B}$, $\mathbf{A}$ consist of two contributions, one with cylindrical symmetry $\left(\text{e.g.,} \ \overline{\mathbf{E}}(r, t) \right)$ and the other with helical symmetry that averages to zero over θ or z $\left(\text{e.g.,} \ \tilde{\mathbf{E}}(r, \theta + kz, t) \right)$. The corresponding solutions for χ satisfying $\nabla^2 \chi = 0$ are thus of the form $\chi = c_1(t) \, \theta + c_2(t) \, z + \tilde{\chi}(r, \theta + kz, t)$. The non-single valued contributions (i.e., the c_1, c_2 terms) generate cylindrically symmetric contribution to the fields.

A straightforward calculation that makes use of the boundary conditions $\tilde{B}_r = \tilde{E}_\theta = \tilde{E}_z = 0$ on the plasma boundary leads to a solution for $\tilde{\chi}$. The details are unimportant since application of the divergence theorem shows that the resulting $\tilde{\chi}$ makes no contribution to the value of H_a. Hereafter $\tilde{\chi}$ is ignored in the analysis.

What remains are the values of c_1, c_2. Consider first c_1. The poloidal magnetic field is given by $B_\theta = \mu A_\theta + c_1 / r$. Clearly $c_1 = 0$ for regularity at the origin.

Next, note that $\dot{E}_z = -\dot{A}_z = -(\dot{B}_z - \dot{C}_2/\mu)$. Consequently, for $\overline{E}_z$ to vanish on the plasma boundary requires that

$$\overline{E}_z\Big|_a = -\frac{\partial A_z}{\partial t}\Big|_a = -\frac{\partial}{\partial t}\left[\frac{1}{\mu}\left(\overline{B}_z - c_2\right)\right]_a = 0 \tag{11.274}$$

This implies that

$$c_2 = \overline{B}_z(a, t) \tag{11.275}$$

The conclusion from this discussion is that the vector potential can finally be written as

$$\mathbf{A} = \mu[\mathbf{B} - B_{z0}J_0(\mu a)\,\mathbf{e}_z] \tag{11.276}$$

and is valid for both the cylindrically symmetric and mixed helical states. The helicity is evaluated by substituting Eq. (11.276) into Eq. (11.258) leading to

$$\frac{H_a}{\overline{H}} \equiv H_0(x) = \frac{x}{J_1^2}\left(J_0^2 + J_1^2 - \frac{2J_0J_1}{x}\right) \tag{11.277}$$
$$\overline{H} = \pi^2 R_0 a^3 \langle B_z\rangle^2$$

Observe that the normalizing factors $\overline{W}$, $\overline{H}$ are functions of $\langle B_z\rangle$ which is a constant during the plasma evolution because of the toroidal flux constraint. This is the reason that these constants are written in terms of $\langle B_z\rangle$ rather than B_{z0}.

Equations (11.272) and (11.277) are two parametric relations in x for $W = W(x)$ and $H_a = H_a(x)$. Eliminating x (numerically) yields the desired relation between energy and helicity: $W = W(H_a)$. This function is plotted shortly after the mixed helicity state is calculated.

Mathematical solution for the mixed helical minimum energy state

The basic equation describing the $m = 0$, 1 mixed helicity state is obtained by operating on Eq. (11.268) with $\mathbf{e}_z \cdot \nabla \times$ and using the relation $\nabla \cdot \mathbf{B} = 0$. The result is a single second-order partial differential equation for B_z given by

$$\nabla^2 B_z + \mu^2 B_z = 0 \tag{11.278}$$

The solution for the $m = 0$, 1 mixed helicity state is easily calculated and has the form

$$\frac{B_z(r)}{B_{z0}} = J_0(\mu r) + C J_1(\alpha r) \cos(\theta + kz)$$

$$\frac{B_\theta(r)}{B_{z0}} = J_1(\mu r) - \frac{C}{\alpha}\left[\mu J_1'(\alpha r) + \frac{k}{\alpha r}J_1(\alpha r)\right]\cos(\theta + kz) \qquad (11.279)$$

$$\frac{B_r(r)}{B_{z0}} = -\frac{C}{\alpha}\left[kJ'_1(\alpha r) + \frac{\mu}{\alpha r}J_1(\alpha r)\right]\sin(\theta + kz)$$

Here, prime denotes differentiation with respect to the argument, k is the helical wave number, $\alpha = (\mu^2 - k^2)^{1/2}$, and C is the helical amplitude. At this point both k and C are arbitrary. Their values are determined shortly by the analysis of the minimum energy state.

The next step is to calculate W and H for the mixed helicity state. The calculation is straightforward but slightly tedious. The results are given by

$$\frac{W}{\overline{W}} = W_0(x) + C^2 W_1(x)$$

$$\frac{H_a}{\overline{H}} = \frac{1}{x}\left[W_0(x) + C^2 W_1(x) - \frac{xJ_0(x)}{J_1(x)}\right] \qquad (11.280)$$

where

$$W_1 = \frac{x^2}{2y^2 J_1^2(x)}\left\{x^2\left[J_0^2(y) + J_1^2(y)\right] - yJ_0(y)J_1(y) - \frac{(x-\kappa)^2}{y^2}J_1^2(y)\right\} \qquad (11.281)$$

and $\kappa = ka$, $y = \alpha a = (\mu^2 - k^2)^{1/2}\,a = (x^2 - \kappa^2)^{1/2}$.

These admittedly complicated looking expressions are subject to an additional constraint resulting from the boundary condition at the plasma edge which, when applied, greatly simplifies the analysis. Specifically, if the plasma is surrounded by a perfectly conducting wall then $B_r(a, \theta, z) = 0$. This condition is trivially satisfied for the $m = 0$ cylindrical state. However, for the $m = 0, 1$ state one sees after a simple calculation that Eq. (11.279) requires that

$$\kappa y J_0(y) + (x - \kappa)\, J_1(y) = 0 \qquad (11.282)$$

Equation (11.282) is a transcendental relation which, when solved, determines $x = x(\kappa)$. Now, it can be shown (numerically) that the energy is an increasing function of x in the regime of interest. It thus follows that the lowest energy mixed helicity state is produced by the value of κ that minimizes x. A numerically obtained plot of x vs. κ is illustrated in Fig. 11.47 which shows that the minimum occurs at $\kappa = \kappa_0 \approx 1.2$ corresponding to $x = x_0 \approx 3.11$.
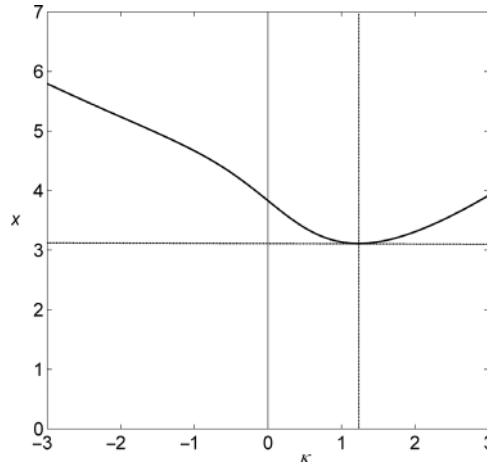
Figure 11.47   Plot of x vs. κ determined from the radial boundary condition. Note the minimum which occurs at $\kappa = \kappa_0 \approx 1.2$ corresponding to $x = x_0 \approx 3.11$.

Observe that all mixed $m = 0, 1$ helical states are characterized by the same value of $x = x_0$. Consequently the values of W and H can change only because the helical amplitude C varies. This is in contrast to the cylindrical state where W and H change because of variations in x. Recognition of this fact allows one to easily calculate the relation between W and H for the $m = 0, 1$ mixed helical state by simply eliminating C in Eq. (11.280). The result is

$$\frac{W}{\overline{W}} = x_0 \left[\frac{H_a}{\overline{H}} + \frac{J_0(x_0)}{J_1(x_0)} \right] \tag{11.283}$$

This is the desired relation.

The minimum energy state

It is now a straightforward matter to determine whether the cylindrical or the $m = 0, 1$ mixed helical state corresponds to the absolute minimum energy. One superimposes plots of $W/\overline{W}$ vs. $H_a/\overline{H}$ for the cylindrical state (Eqs. (11.272) and (11.277)) and the $m = 0, 1$ helical state (Eq. (11.283)) as illustrated in Fig. 11.48. There are several points to be made:

- For low values of H_a only the $m = 0$ solution can exist. Therefore, in this regime the plasma is cylindrical.
- At higher values of H_a both the $m = 0$ and $m = 0, 1$ states can exist simultaneously. The $m = 0, 1$ state has the lowest energy and in this regime the plasma transforms from a cylinder to a helix.
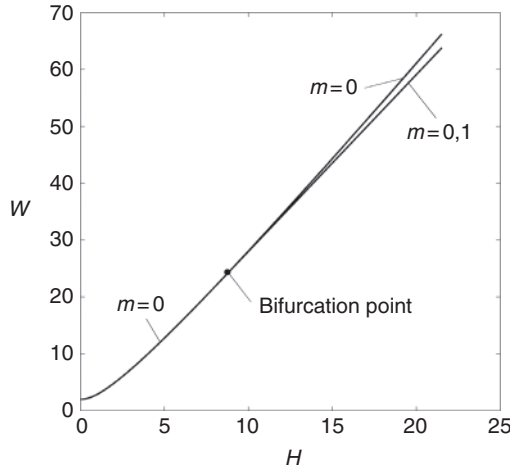
Figure 11.48 Energy vs. helicity for the $m = 0$ cylindrical state and the $m = 0, 1$ mixed helical state.

- The helical state cannot exist for low H_a because the radial boundary condition given by Eq. (11.282) cannot be satisfied for $x \leq x_0 = 3.11$. The condition $x \leq x_0$ corresponds to a minimum allowable value of H_a. This can be seen by considering an $m = 0$ state and an $m = 0, 1$ state, which because of conservation of helicity, have the same H_a. Equating the expressions for H_a given by Eqs. (11.277) and (11.280), with the latter evaluated at $x = x_0$, yields an expression for C^2 given by

$$C^2 = \left[\frac{W_0(x)}{x} - \frac{W_0(x_0)}{x_0} - \frac{J_0(x)}{J_1(x)} + \frac{J_0(x_0)}{J_1(x_0)} \right] \frac{x_0}{W_1(x_0)} \tag{11.284}$$

  For $x \leq x_0$ or equivalently $H_a(x) \leq H_a(x_0)$, one can easily verify (numerically) that $C^2 < 0$, which is unphysical.
- The transition from the $m = 0$ to the $m = 0, 1$ state occurs at the bifurcation point $H_a/\overline{H} \approx 8.21$.
- Recall that B_z reverses when $x \approx 2.4$ in the cylindrical state, which corresponds to $H_a/\overline{H} \approx 2.4$. Therefore, an RFP that evolves from an initial state with zero current to a final state whose helicity lies in the range $2.4 < H_a/\overline{H} < 8.21$ should have the form of a cylindrical plasma with a reversed B_z field.
- The last point concerns the minimizing wave number $ka \approx 1.2$ which is obviously positive. Since the condition for an $m = 1$ resonant surface within the plasma is given by $k = -B_\theta/rB_z$ the implication is that the helix rotation direction aligns with the magnetic lines exterior to the B_z reversal surface (i.e., $B_z < 0$ corresponds to $k > 0$). Furthermore, for $x_0 = 3.11$ the range of resonant k values between the reversal surface and the plasma edge is given by

$-J_1(x_0)/J_0(x_0) = 1.01 < ka < \infty$. This range includes $ka \approx 1.2$. The conclusion is that the wave number of the Taylor helical state corresponds to a resonant ka located between the reversal surface and the plasma edge (reversal occurs at $r/a \approx 0.77$ while resonance occurs at $r/a \approx 0.88$).

This completes the mathematical description of Taylor relaxation theory. The next step is to see how well the theory applies to RFP experiments.

Application to experiment

There are several important applications of Taylor's theory to actual experimental situations. One involves the need for a B_z reversal. The other involves the predicted evolution of an RFP plasma as the current is increased. These are discussed below.

Consider first the importance of the B_z reversal. Strictly speaking Taylor's theory does not suggest that an RFP with a non-reversed B_z should have poorer performance than one with a reversed B_z. In both cases the plasma has relaxed to a minimum energy state. However, actual experiments do exhibit a strong change in performance when reversal occurs and it is interesting to understand the reason.

The answer lies in the fact that a Taylor state is characterized by a current profile with $J_z(a) \neq 0$. In contrast actual experiments almost always have $J_z(a) \approx 0$ because of plasma contact with the cold surrounding wall. This experimental reality is not included in Taylor's theory. The consequence is that the minimum energy profiles must be modified near $r \approx a$ to insure that $J_z(a) \approx 0$. Over the large remaining core of the plasma the Taylor profiles are quite reasonable.

Recall now the discussion in Section 11.7.2 which shows that RFP profiles with $J_z(a) \approx 0$ have a minimum in $q(r)$ when B_z is not reversed. Such profiles are always ideal MHD unstable, being driven by both the parallel current and the pressure gradient. This fact helps to explain the poor performance without a B_z reversal. On the other hand, when B_z has a reversal, the $q(r)$ profile no longer has a minimum and the ideal MHD instabilities are no longer excited. The result is a much improved experimental performance. The conclusion is that the condition for the onset of a B_z reversal as predicted by Taylor's theory plays a far more important role in RFP operation than one might have originally anticipated.

The second application of Taylor's theory concerns the evolution of an RFP plasma as the current is increased. To address this issue from an experimental point of view assume that initially a uniform bias B_z field is produced in the vacuum chamber. This sets the initial the value of the toroidal flux which is then conserved during the plasma evolution. Next, the toroidal current is increased slowly towards its final value. The initially cold plasma begins to heat due to the ohmic power. Ideally one would like to compare the theoretical and experimental magnetic field profiles as the current $I(t)$ increases. However, these are difficult experimental
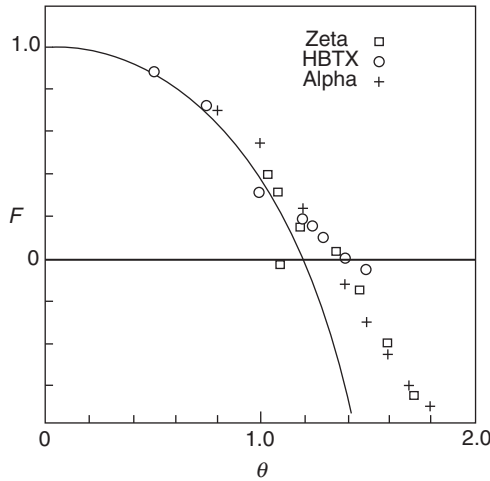
Figure 11.49   Diagram of F vs. θ comparing theoretical and experimental data from several RFP experiments (from Taylor, 1986). Reproduced with permission.

measurements. A simpler test is to compare the theoretical prediction of $B_z(a,t)$ with the easy-to-measure experimental value. If the current rise time is slow (as it is for most RFP plasmas) then Taylor's theory predicts that the RFP should evolve through a sequence of minimum energy states. The desired relation between $B_z(a, t)$ and $I(t)$ can be illustrated in a convenient normalized form by plotting an $F(t)$ vs. $\theta(t)$ diagram. The normalization is useful because it allows a comparison between different experiments on the same diagram.

For the Taylor minimum energy cylindrical profiles, F and θ are related parametrically through x as follows:

$$
\begin{aligned}
F(t) &\equiv \frac{B_z(a,t)}{\langle B_z \rangle} = \frac{x J_0(x)}{2 J_1(x)} \\
\theta(t) &\equiv \frac{B_\theta(a,t)}{\langle B_z \rangle} = \frac{x}{2}
\end{aligned}
\tag{11.285}
$$

A plot of $F(t)$ vs. $\theta(t)$ is illustrated in Fig. 11.49 (Taylor, 1986). Here, one can view increasing θ as equivalent to increasing time during the plasma evolution. Note that field reversal occurs at $\theta \approx 1.2$ and the $m = 0, 1$ helical bifurcation point corresponds to $\theta \approx 1.56$. Also shown in the diagram is a sequence of data points from early RFP experiments. Observe that there is quite good agreement between theory and experiment. The agreement using the model profiles, although not illustrated, is even further improved because of the more realistic treatment of the edge. However, it must be emphasized that without Taylor's theory there is no justification for believing that the plasma should evolve along the $F(t)$ vs. $\theta(t)$ curve.

To summarize, Taylor's theory provides a simple but elegant explanation of the evolution of ohmically heated RFP plasmas. The theory captures the magnetic field and current density profiles except right near the edge. It predicts zero pressure while in practice the pressure is finite because of ohmic heating. Even so the experimentally measured β_p values are usually small compared to the ideal MHD stability limits. Experimentally, good performance requires raising the current to a sufficiently high value, $\theta > 1.2$, so that B_z reverses.

11.7.7 *Ideal external modes*

From the point of view of ideal MHD the analysis thus far presented has shown that an RFP can be stable against all internal current-driven and pressure-driven modes at high values of $\beta_p \sim 0.2$. This subsection focuses on ideal external modes, setting aside temporarily Taylor's prediction of $\beta_p \to 0$ which involves resistive MHD. Note that when the plasma is bounded by a perfectly conducting wall the internal mode analysis constitutes a complete description of ideal MHD stability. In this section it is shown that the presence of a conducting wall is crucial. Without such a wall an RFP is always unstable to external modes, even at $\beta_p = 0$. A comprehensive study of ideal and resistive MHD stability for the case $\beta_p = 0$ has been carried out by Antoni *et al.* (1986). The results presented here are consistent with Antoni *et al.* in the appropriate regions of overlap.

Before proceeding, however, a discussion is warranted regarding the way in which external modes can be excited in an RFP. The reason for the discussion is that in practice, RFP plasmas exist out to the wall – there is no well-defined vacuum region separating plasma from wall. Why then worry about external modes? The answer is associated with the fact that the edge of the plasma is cold because of its contact with the wall, or perhaps a limiter, and thus is highly resistive. Since $\eta \propto 1/T^{3/2}$ it follows that the cold edge of an ohmically heated plasma can be treated as a current-free resistive layer. As discussed in Section 8.10, such a layer leads to the same MHD stability boundaries as a vacuum, although with lower growth rates when unstable.

Now, in practice the transition from a high β_p ideal plasma region to a cold current-free resistive plasma region is gradual. Even so, to keep the physics simple but crisp, the analysis presented below adds a narrow resistive plasma layer to the outside of the ideal plasma. The layer is located between $a < r < b$ and can be treated as a vacuum region for the purpose of calculating the marginal stability boundaries. In carrying out these calculations the wall at $r = b$ is assumed to be perfectly conducting.

Here again difficulties arise because in practice the wall is resistive. Thus, modes which are wall stabilized when b/a is sufficiently close to the plasma but

are unstable with a wall at infinity become resistive wall modes. Some form of feedback or rotational stabilization is required.

To summarize, the analysis focuses on calculating the marginal stability boundaries against all external modes in an RFP whose core is separated from a perfectly conducting wall by a narrow current-free resistive plasma region. The specific goals are to first determine which k (or n) values are unstable with the wall at infinity and to then determine how close the wall must be (i.e., calculate the critical b/a) to stabilize all such modes. This information is critical to assess the ease or difficulty in providing feedback stabilization. The information is then used to discuss experimental results aimed at avoiding external mode instabilities in an RFP.

Theoretical/computational analysis

The theoretical/computational analysis of external mode stability requires a straightforward numerical calculation. The most dangerous external modes correspond to $m = 1$ and almost always have a resonant surface in the vacuum region. The corresponding values of wave number to be tested are then defined as those values of k for which $F(r) \neq 0$ in the plasma. For RFPs with a field reversal this range of k is given by

$$-\frac{B'_\theta(0)}{B_z(0)} < k < -\frac{B_\theta(a)}{aB_z(a)}$$

$$-\left[\frac{6(1-F)}{3-2F}\right]^{1/2} < n\varepsilon < -\frac{\theta}{F} \tag{11.286}$$

where the second form corresponds to the model profiles and $ka = n\varepsilon$.

The stability boundaries are determined by solving

$$\frac{d}{dr}\left(f\frac{d\xi}{dr}\right) - g\xi = 0 \qquad \xi(0) = 1 \qquad \xi'(0) = 0 \tag{11.287}$$

for $0 < r < a$ and then evaluating $\xi'(a)/\xi(a)$. This quantity is substituted into Eq. (11.118) or equivalently Eq. (11.148), leading to the desired value of $\hat{W} = \hat{W}(n\varepsilon)$. The numerical solution to Eq. (11.287) is easy to obtain since $F(r) \neq 0$ in the plasma implying that there are no singularities in the equation. The procedure just described has been carried out for various values of β_p assuming that $b/a = \infty$, $F = -0.2$, $\theta = 1.45$, and $\varepsilon = 1/5$. Also, for numerical convenience n is treated as a continuous variable but obviously should only be allowed to have integer values when applied to actual experiments. The results are illustrated for two values of β_p (i.e., $\beta_p = 0$ and $\beta_p = 0.1$) in Fig. 11.50, which illustrates $\hat{W}$ vs. n.
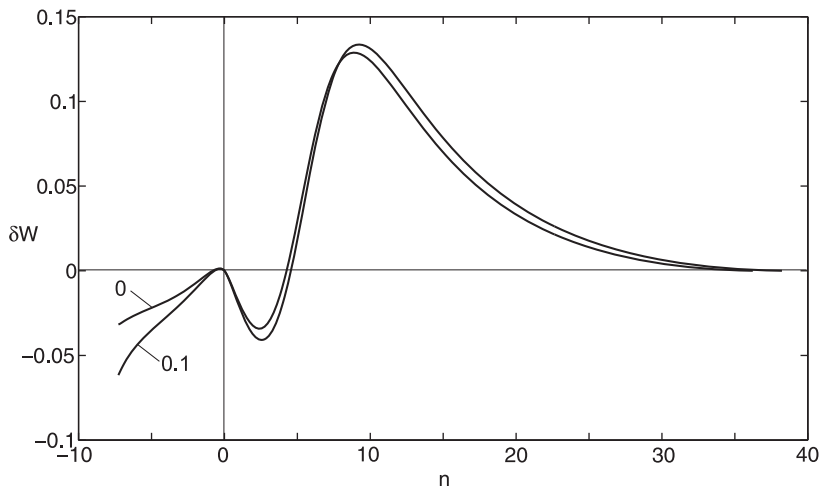
Figure 11.50   Stability diagram of δW vs. n for external mode stability in an RFP with the wall at infinity. The parameters correspond to $F = -0.2$, $\theta = 1.45$. The two curves correspond to $\beta_p = 0$ and $\beta_p = 0.1$.

Observe that the plasma is unstable for both positive and negative n. For $\beta_p = 0$ the unstable positive n values correspond to $1 \leq n \leq 4$. For these modes the helicity has the same sense as the fields outside the reversal surface. The unstable negative n values lie in the range $1 \leq -n \leq 7$. Here, the helicity aligns with the field inside the reversal surface. Note that the curves end abruptly at about $n \approx -7.5$. For more negative values the resonant surface moves into the plasma from the origin. The mode becomes an internal mode which is quickly stablized. All told, the plasma is unstable to 11 external modes, even at $\beta_p = 0$. As expected, finite β_p makes the situation more unstable but only by a small amount. It is not a dominant effect.

It is clear from these results that for the RFP to be a viable fusion concept it is necessary to wall stabilize the external kink modes. The key issue is to determine how close to the plasma must one place a perfectly conducting wall to stabilize all external kink modes. A similar set of numerical calculations as described above has been carried out to answer this question. For this study all the parameters are the same as for Fig. 11.50 except that b/a is allowed to vary. The mode number n is again treated as a continuous variable. The results are given in Fig. 11.51, which illustrates curves of $\hat{W}$ vs. n for various b/a assuming that $\beta_p = 0$.

The main results are as follows. As intuition suggests, moving the wall closer to the plasma raises the curves, producing an increasingly positive value of $\hat{W}$; that is, the plasma is becoming more stable. For the curves shown, corresponding to $\theta = 1.45$, one sees that all external kink modes are stabilized for $b/a < 1.7$. The last mode that is stabilized has a toroidal mode number $n = -7$.
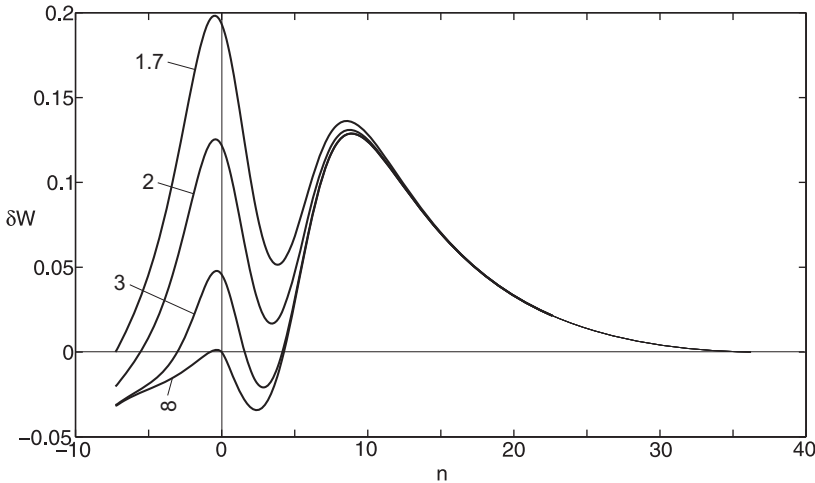
Figure 11.51 Stability diagram of δW vs. n for external mode stability in an RFP for various b/a. The parameters correspond to $F = -0.2$, $\theta = 1.45$, and $\beta_p = 0$. Observe wall stabilization as b/a decreases.

A similar set of curves can be generated for different values of θ. The results are qualitatively similar with one exception. As the current (θ) increases, the modes with positive n become relatively more unstable than the modes with negative n. Eventually, above a critical $\theta = 1.5$, the last mode to become stabilized switches from negative n to positive n. In other words, the helical sense of the most unstable mode switches from being aligned with the field inside the reversal radius to the field on the outside. This point is illustrated in Fig. 11.52, which illustrates the critical b/a vs. θ for the most unstable mode. Also shown are the corresponding values of n for the last mode to be stabilized. The switch from an inside to an outside mode is clearly exhibited at $\theta = 1.5$. The process has been repeated for several values of β_p, also illustrated in Fig. 11.52.

The last point of interest concerns the dependence of stability on the current profiles. The model profiles are fairly broad, approximating the Taylor profiles everywhere except at the edge. More peaked profiles, which are often observed experimentally, effectively reduce the size of the plasma radius to a value denoted by $a_{eff} < a$. Since the unstable toroidal mode numbers scale as $n \sim 1/\varepsilon \to R_0/a_{eff}$, the implication is that peaked current profiles will be unstable to a wider range of unstable n values than broad profiles. Numerical calculations, not presented here, indeed confirm this intuition.

Experimental stabilization of external kink modes

The above analysis has shown that an RFP will always be unstable to multiple external kink modes, even at $\beta_p = 0$, with the wall at infinity. These modes can be
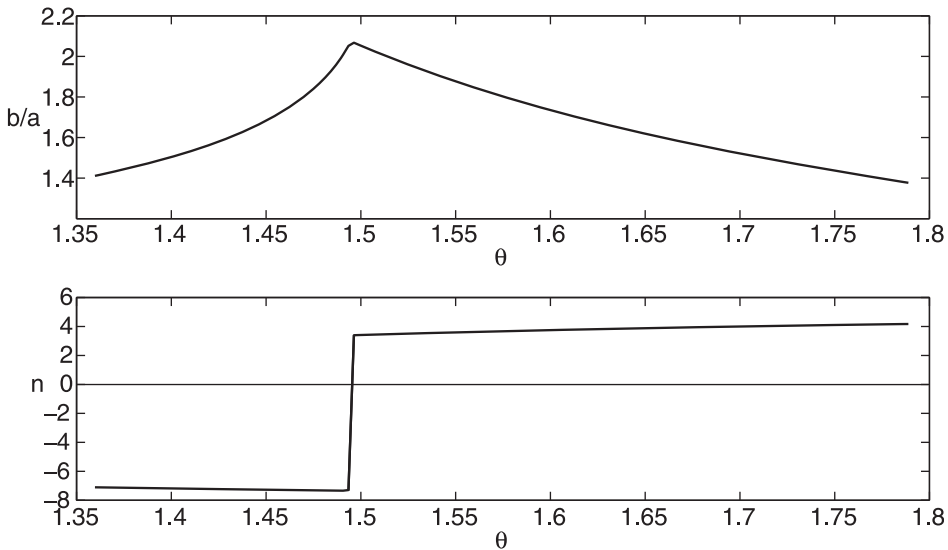
Figure 11.52   Critical *b/a*, and corresponding *n*, vs. *θ* for the most unstable external kink mode. Note the switch from an inside to an outside mode at $\theta = 1.5$ for $\beta_p = 0$. Curves are also illustrated for $\beta_p = 0.05$ and $\beta_p = 0.1$.

stabilized by a close-fitting conducting shell. Of course the stabilized modes are then transformed into resistive wall modes. For the RFP to move forward as a fusion concept it must be possible to simultaneously stabilize all resistive wall modes, at least ten in number.

Many researchers believed it would be *theoretically* possible to simultaneously feedback stabilize all the resistive wall modes. However, these same researchers (the author included) also believed it would be not possible to *experimentally* achieve this goal because of engineering complexity. This is one situation where the author is pleased to admit being wrong. Experiments on two European RFP experiments, EXTRAP T2R (Brunsell *et el.*, 2004) in Sweden and RFX-mod (Paccagnella *et al.*, 2006) in Italy, demonstrated that sophisticated feedback systems could be constructed that would simultaneously stabilize all external kink modes.

For example, the RFX-mod experiment has 192 feedback saddle coils, each one independently controllable. This sophisticated feedback system has been operated experimentally and shown to stabilize all resistive wall modes. A striking example of this stabilization is illustrated in Fig. 11.53. Shown here are experimental traces of plasma current versus time for various progressive states of the feedback control system. The lifetime of the discharge has been extended substantially. The final decay of the plasma is not due to a loss of feedback control, but is the result of having utilized all the volt-seconds available from the transformer.
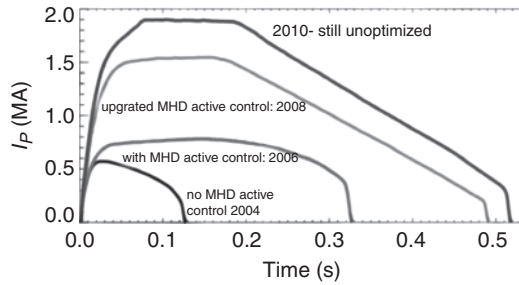
Figure 11.53   RFX experimental traces of plasma current vs. time for progressing states of the feedback control system. Note the extended lifetime with the feedback activated. From Martin et al, 2011. Reproduced with permission.

The conclusion is that feedback control has been able to stabilize all external kink modes in an RFP, a very favorable result. Also internal modes are ideally stable to quite high values of β_p. Still, experimental values of β_p, even in feedback stabilized discharges, are considerably lower than the ideal MHD internal limits, primarily because of anomalous resistive MHD turbulence causing enhanced transport. The resulting energy confinement times are noticeably poorer than those in a tokamak with comparable current. It is this poor confinement, and not MHD, that suggests that for the standard RFP to move forward the transport must be improved. This then is one major goal of RFP research – improve transport. A second major goal is to discover an efficient way to non-inductively drive a large amount of current.

Two innovative methods have been suggested to achieve the transport goal – profile control and single helicity states. These topics involve detailed studies of resistive MHD stability and are thus beyond the scope of the present textbook. Several relevant references are listed at the end of the chapter.

11.7.8 Overview of the RFP

The RFP is an axisymmetric toroidal configuration with $B_\theta^2 \sim B_z^2 \sim \mu_0 p$. It achieves ideal MHD stability with an optimally efficient use of the magnetic field profiles. Specifically, the B_z field has a reversal near the outside of the profile and is much smaller in magnitude than the toroidal field in a tokamak with the same toroidal current. This is a major technological advantage of the RFP.

Good MHD stability at high β is possible against all internal ideal MHD modes. However, external modes with a wall at infinity are potentially very unstable because the value of $q_a \sim \varepsilon$ is small at the plasma edge. A large number of modes, on the order of 10–20, would be simultaneously unstable as resistive wall modes unless they are feedback stabilized. For many years researchers thought this would

be too difficult technologically. However, experiments in Sweden and Italy have shown that sophisticated feedback systems could be developed that provide stabilization against all external ideal MHD modes.

The result is longer lived RFP plasmas, whose lifetime is limited by external power supply constraints. This favorable result is somewhat tempered by the fact that transport in these long lived states is still substantially below that in a tokamak of comparable size and current. The reason is the presence of resistive MHD turbulence. There remains a clear need to improve transport and this is one of the major areas of current and future RFP research. A second major area of research requires the development of efficient methods of non-inductive current drive. Some effort has been devoted to this problem but most of RFP research has focused on improved transport.

11.8 Summary

In Chapter 11 the Energy Principle and the eigenvalue formulation of MHD have been used to investigate the stability of 1-D, cylindrically symmetric, equilibria. A summary of these results is given below.

The θ-pinch

The straight θ-pinch is shown to be stable to all m, k modes for arbitrary values of β. The potential energy δW is either positive or approaches zero when $k \to 0$. This favorable result is a consequence of the fact that a θ-pinch has neither parallel currents nor field line curvature to drive instabilities. Unfortunately the θ-pinch cannot be bent into a torus unless additional fields are added to provide toroidal force balance and it is these fields that ultimately determine stability.

The Z-pinch

The straight Z-pinch is unstable to two potentially dangerous instabilities, each driven by a combination of the pressure gradient and unfavorable curvature. The first instability is the short wavelength $m = 1$ mode while the second corresponds to the $m = 0$ sausage instability. Both of these modes can lead to very undesirable, if not catastrophic behavior of the plasma. Thus, even though a Z-pinch can easily be bent into a torus, its unsatisfactory MHD stability properties make it a poor candidate for fusion energy applications.

Adding a hard-core current-carrying conductor along the axis greatly improves the situation. With sufficient current the $m = 1$ mode is stabilized. Equally importantly, when the pressure gradient decays sufficiently weakly the sausage instability is also stabilized. The toroidal version of the hard-core pinch is known as a levitated dipole. The same favorable stability properties exist although the

need to levitate the superconducting hard core is a clear technological disadvantage. In addition, D-D is required as the fuel in order to prevent neutron heating and quenching of the superconductors.

The general screw pinch

The Energy Principle for the general screw pinch reduces to a 1-D quadratic integral in terms of the single unknown ξ, which is the radial component of the plasma displacement. An analysis of the energy integral leads to several general results:

- Suydam's criterion provides a simple necessary condition for stability against localized interchange modes. The criterion requires only a simple substitution of equilibrium profiles to test stability which quantifies the balance between shear and unfavorable profiles.
- Newcomb's analysis demonstrates how the minimizing differential equation associated with the variation of δW can be used to determine necessary and sufficient conditions for stability of arbitrary profiles. Application of Newcomb's procedure requires the (numerical) solution of a 1-D differential equation in r.
- The Goedbloed–Sakanaka oscillation theorem, valid for the general screw pinch, proves that the most unstable (i.e., fastest growing) MHD perturbation always has the structure of a macroscopic zero-node mode. This theorem shows why it is important to satisfy Suydam's criterion – the existence of not very worrisome, highly localized interchange modes always implies the existence of a large-scale macroscopic mode.
- For a screw pinch external modes can be unstable. They can, however, be stabilized by the presence of a perfectly conducting wall sufficiently close to the plasma. Realistically, the wall has a finite resistivity, in which case the mode again becomes unstable although as a resistive wall mode. The stability boundary is the same as when the wall is at infinity, although the growth rates are much slower, comparable to the wall diffusion time, allowing for the possibility of feedback stabilization.

The straight tokamak

The straight tokamak provides reliable information about current-driven kink modes in a circular cross section plasma. It provides unreliable information for pressure-driven modes since these are strongly affected by toroidal curvature which is obviously not included in a straight model. The main conclusions and connections with experiments are as follows:

- With respect to internal modes only the $m = 1$, $n = 1$ internal kink can become unstable. The ideal MHD version is the initial drive for sawtooth oscillations although a full non-linear toroidal calculation, including finite pressure and resistivity, is required to at least partially explain the data. The main consequence of sawtooth oscillations is to clamp the value of safety factor on axis to approximately $q_0 \approx 1$ or slightly lower. This limits the current density, and hence the ohmic heating on axis.

- The $m = 1$, $n = 1$ external kink mode sets a limit on the total current that can flow in the plasma. The corresponding stability limit $q_a > 1$ is known as the Kruskal–Shafranov limit. In practice, external kink modes with slightly higher values of m can also become unstable and these set stricter limits on q_a. The exact limit depends on profiles but typically $q_a \sim 2.5-3$ is needed to avoid an instability. When the external kink mode criterion is violated the result is most likely to be a major disruption in which both the pressure and current quench in a very short time corresponding to a catastrophic termination of the plasma. Too much current, or alternatively too much edge density (which shrinks the size of the plasma lowering the effective q_a), lead to major disruptions.

- Higher m external kinks can also become unstable if the edge current and current gradient are not sufficiently small. High edge gradients often appear in H-mode operation of a tokamak. When higher m external kink modes are excited the usual results are ELMs, periodic bursts of plasma energy and particles. If strong enough, ELMs can produce irreversible damage to the divertor plate. ELMs are thought to be driven by ballooning-kink modes with the kink component of the perturbation being reasonably well treated conceptually by the straight tokamak analysis.

Overall, the straight tokamak analysis suggests that successful operation requires a sufficiently small current with a sufficiently small edge gradient. Small current is readily controllable experimentally. In contrast, control of the edge gradient is a much more difficult task experimentally.

The reversed field pinch

The ideal MHD properties of an RFP are accurately described by the 1-D cylindrical model. There are a variety of modes that can become unstable. A useful way to organize the stability results and develop some intuition is summarized below:

- To begin, as its name implies, an RFP must have a reversal in the B_z field. If not, an internal $m = 1$ is excited localized around the minimum in $q(r)$. This leads to poor transport because of strong MHD turbulence. Therefore, high-performance RFPs always have a field reversal to avoid the problem of very poor transport.

- An RFP always has a limit on β due to the $m = 0$ mode. There must be sufficient toroidal field to prevent the analog of sausage instabilities. The β limit is approximately $\beta < 0.5$, which is a weak requirement in terms of normal experimental operation.
- Suydam's criterion leads to stricter limits on β. To avoid the resulting localized interchange instabilities the pressure profile must be very flat near the origin and have a very small edge gradient. When such profiles are generated, the β limits typically lie in the range $0.1 < \beta < 0.35$, the exact value depending on the amount of B_z reversal.
- Assuming that Suydam's criterion is satisfied, one then finds that all macroscopic internal modes are also stable for the typical operating range of RFP experiments, $0 > F > -1$. This conclusion is valid up until the value of β predicted by Suydam's criterion and is a very favorable conclusion.
- Focusing on internal perturbations, Taylor has provided a theory that explains the typical time evolution of an RFP plasma. His analysis assumes that there is always a background level of resistive MHD turbulence. The theory suggests that an RFP plasma always evolves to a minimum energy state subject to the constraint of conservation of total helicity. The resulting profiles have flat current density profiles out to the wall and zero β. The zero β result does not take into account that an RFP plasma is always driven by ohmic current which keeps the pressure finite. Taylor's theory qualitatively explains the evolution of the magnetic fields in an RFP but clearly underestimates the achievable values of β.
- Next consider external modes. Because of the low value of q_a, an RFP is always unstable to a large number of $m = 1$ modes with the wall at infinity, even when $\beta_p = 0$. Typically 10–20 different n modes can be simultaneously unstable, depending upon profile. While these modes could be theoretically stabilized as resistive wall modes with a sufficiently close wall, many researchers believed this would be an impossibly difficult technological problem. Undeterred by this pessimism, experimentalists in Sweden and Italy developed highly sophisticated feedback systems that demonstrated complete stability against all ideal external modes. This favorable result opens up the opportunity to improve transport in an RFP. However, even after wall stabilization, transport still remains poorer than in a comparable tokamak because of resistive MHD turbulence. Improving transport is a major area of RFP research.

Overall, the RFP has had a more difficult path to follow than the tokamak in terms of plasma physics performance because of its inherently low q. Still, performance has steadily progressed by some very clever innovations but it still remains to be seen if the RFP can overtake the tokamak in terms of performance. If so, the low toroidal field would be a major technological advantage.

References

Antoni, V., Merlin, D., Ortolani, S., and Paccagnella, R. (1986). *Nucl. Fusion* **26**, 1711.

Bodin, H. A. B. and Newton, A. A. (1980). *Nucl. Fusion* **20**, 1255.

Brunsell, P. R., Yadikin, D., Gregoratto, D., *et al*. (2004). *Phys. Rev. Lett*. **93**, 225001.

Goedbloed, J. P., Pfirsch, D., and Tasso, H. (1972). *Nucl. Fusion* **12**, 649.

Goedbloed, J. P. and Sakanaka, P. H. (1974). *Phys. Fluids* **17**, 908.

Goedbloed, J. P. and Poedts, S. (2004). *Principles of Magnetohydrodynamics*. Cambridge: Cambridge University Press.

Gradshteyn, L. S. and Ryzhik, I. M. (2000). *Table of Integrals, Series, and Products*, 6th edn. San Diego, CA: Academic Press.

Greenwald, M., Terry, J. L., Wolfe, S. M. *et al*. (1988). *Nucl. Fusion* **28**, 2199.

Greenwald, M. (2002). *Plasma Phy. Controlled Fusion* **44**, R27.

Hain, K. and Lust, R. (1958). *Z. Naturforsch. Teil A* **13**, 936.

Hughes, J. W., Snyder, P. B., Walk, J. R., *et al*. (2013). *Nucl. Fusion* **53**, 043016.

Kadomtsev, B. B. (1966). In *Reviews of Plasma Physics*, Vol. 2, ed. M. A. Leontovich. New York: Consultants Bureaus.

Kikuchi, M., Lackner, K., and Tran, M. Q., eds. (2012). *Fusion Physics*. Vienna: International Atomic Energy Agency.

Kruskal, M. D. and Schwarzschild, M. (1954). *Proc. R. Soc. London, Ser. A* **223**, 348.

Landau, L. D. (1946). *J. Phys. (USSR)* **10**, 25

Laval, G. and Pellat, R. (1973). In *Controlled Fusion and Plasma Physics*, Proceedings of the Sixth European Conference, Moscow, Vol. II, p. 640.

Laval, G., Pellat, R., and Soule, J. L. (1974). *Phys. Fluids* **17**, 835.

LDX Group (1998). *Innovative Confinement Concepts Workshop*. Princeton, NJ: Princeton Plasma Physics Laboratory.

Martin, P., Adamek, J., Agostinetti, P., Agostini, M. et al. (2011). *Nucl. Fusion* **51** 094023.

Newcomb, W. A. (1960). *Ann. Phys. (NY)* **10**, 232.

Paccagnella, R., Ortolani, S., Zanca, P. *et al*. (2006). *Phys. Rev. Lett*. **97**, 075001.

Reiman, A. (1980). *Phys. Fluids* **23**, 230.

Rosenbluth, M. N., Dagazian, R. Y., and Rutherford, P. H. (1973). *Phys. Fluids* **11**, 1984.

Shafranov, V. D. (1956). *At. Energy* **5**, 38.

Shafranov, V. D. (1970). *Sov. Phys.-Tech*. **15**, 175.

Snyder, P. B., Wilson, H. R., and Xu, X. Q. (2005). *Phys. Plasmas* **12**, 056115.

Suydam, B. R. (1958). In *Proceedings of the Second United Nations International Conference on the Peaceful Uses of Atomic Energy*. Geneva: United Nations, **31**, p. 157.

Tataronis, J. A. and Grossmann, W. (1973). *Z. Physik* **261**, 203.

Taylor, J. B. (1974). *Phys. Rev. Lett*. **33**, 1139.

Taylor, J. B. (1986). *Rev. Modern Phys*. **3**, 741

Wesson, J. A. (2011). *Tokamaks*, 4th edn. Oxford: Oxford University Press.

Whyte, D. G., Hubbard, A. E., Hughes, J. W. *et al*. (2010). *Nucl. Fusion* **50**, 105005.

Woltjer, J. (1958). *Proc. Nat. Acad. Sci. (USA)* **44**, 489.

Yamada, M., Levinton, F. M., Pomphrey, N. *et al*. (1994). *Phys. Plasmas* **1**, 3269.

Further reading

General screw pinch stability theory

Goedbloed, J. P. and Poedts, S. (2004). *Principles of Magnetohydrodynamics*. Cambridge: Cambridge University Press.

The reversed field pinch

Bodin, H. A. B. and Newton, A. A. (1980). *Nucl. Fusion* **20**, 1255.
Cooper, W. A., Graves, J. P., Sauter, O. *et al.* (2011). *Plasma Phys. Controlled Fusion* **53**, 084001.
Escande, D. F., Martin, P., Ortolani, S. *et al.* (2000). *Phys. Rev. Lett.* **85**, 1662.
Kikuchi, M., Lackner, K. and Tran, M. Q., eds. (2012). *Fusion Physics.* Vienna: International Atomic Energy Agency.
Martin, P., Adamek, J., Agostinetti, P. *et al.* (2011). *Nucl. Fusion* **51**, 094023.
Robinson, D. C. (1971). *Plasma Phys.* **13**, 439.
Sarff, J. S., Hokin, S. A., Ji, H. *et al.* (1994). *Phys. Rev. Lett.* **72**, 3670.
Sovinec, C. and Prager, S. C. (1999). *Nucl. Fusion* **39**, 777.

Tokamaks

Bateman, G. (1978). *MHD Instabilities.* Cambridge, MA: MIT Press.
Furth, H. P. (1975). *Nucl. Fusion* **15**, 133.
Furth, H. P. (1985). *Phys. Fluids* **28**, 1595.
Mukhovatov, V. S. and Shafranov, V. D. (1971). *Nucl. Fusion* **11**, 605.
Kikuchi, M., Lackner, K., and Tran, M. Q., eds. (2012). *Fusion Physics.* Vienna: International Atomic Energy Agency.
Wesson, J. A. (1978). *Nucl. Fusion* **18**, 87.
Wesson, J. A. (2011). *Tokamaks*, 4th edn. Oxford: Oxford University Press.
White, R. B. (1986). *Rev. Mod. Phys.* **58**, 183.
White, R. B. (2006). *Theory of Toroidally Confined Plasmas*, 2th edn. London: Imperial College Press.

Problems

11.1 Consider the marginal stability equation for the general screw pinch, given by

$$\mathbf{F}(\boldsymbol{\xi}) = 0$$

By direct reduction of this equation (i.e., do not use a variational minimization procedure) derive the one-dimensional radial equation for the eigenfunction $\xi = \xi_r(r)$. Show that this equation can be written as

$$(f\xi')' - g\xi = 0$$

where $f(r)$ and $g(r)$ are given by Eq. (11.90).

11.2 One term in δW that is always stabilizing for an arbitrary cylindrical screw pinch is given by

$$\delta W_a = \int f\xi'^2 dr$$

where $f = r^3 (kB_z + mB_\theta/r)^2/(k^2 r^2 + m^2)$. Show that for an $m = 1$ mode, $\delta W_a \to 0$ as $\Delta \to 0$ for the trial function illustrated in Fig. 11.54. Assume the pinch
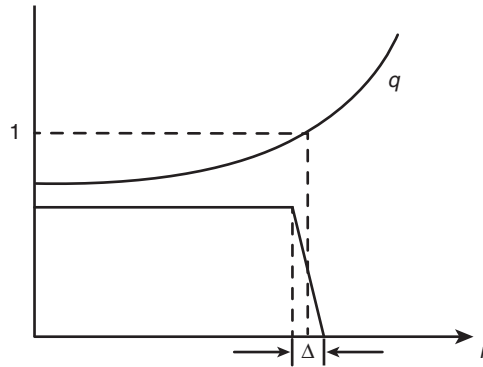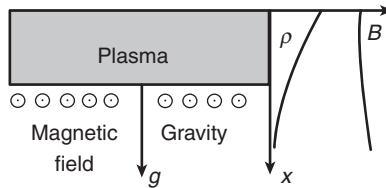
Figure 11.54   Diagram for Problem 11.2.

Figure 11.55   Diagram for Problem 11.3.

represents an equivalent torus of length $2\pi R_0$, implying that $k = -n/R_0$. Note that for $\delta W_a \to 0$ there must be a surface in the plasma where $nq(r_s) = 1$

11.3 Consider a slab model of a plasma supported in equilibrium against gravity by a uniform magnetic field $\mathbf{B} = B\mathbf{e}_z$ as shown in Fig. 11.55.

(a) Calculate the one-dimensional radial pressure-balance relation describing the equilibrium.
(b) Derive the one-dimensional eigenvalue equation describing linear stability. Assume the perturbations vary as $\xi = \xi(x)\exp(-i\omega t + ik_y y + ik_z z)$. For simplicity assume incompressible displacements.
(c) Form an Energy Principle from the eigenvalue equation and show that $k_z^2 \to 0$ is the most unstable mode.
(d) Assume that $\rho(x) = \rho_0 \exp(-x/a)$ and show that

$$\omega^2 = -g/a$$

This is the Raleigh–Taylor instability.

11.4 Consider a slab model of a plasma with a constant external gravitational force. Assume a one-dimensional equilibrium with $p(x)$, $B_y(x)$, $B_z(x)$ and $g = $ constant.
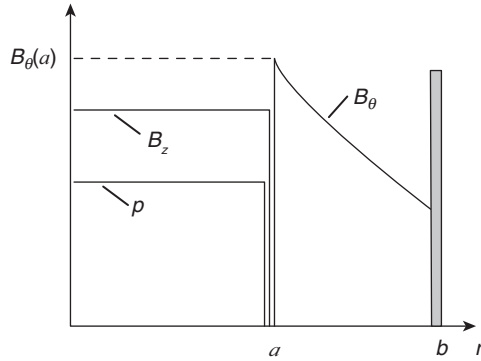
Figure 11.56   Diagram for Problem 11.5.

(a) Show that the Energy Principle for this system reduces to

$$\frac{\delta W}{L_y L_z} = \frac{1}{2} \int dx \left[\frac{F^2}{k^2} |\xi'|^2 + \left(F^2 + g\rho' \right) |\xi|^2 \right]$$

where $\mathbf{k} = k_y \mathbf{e}_y + k_z \mathbf{e}_z$, $F(x) = k_y B_y + k_z B_z$ and $\xi(x) = \xi_x$.

(b) Derive the equivalent Suydam's criterion for this system. (The final criterion should be a function only of equilibrium quantities.)

(c) By comparing the slab and cylindrical versions of Suydam's criterion, show how gravity can be used to "mock up" field line curvature.

11.5 A standard RFP is always unstable to external modes if the conducting wall is moved to infinity. The purpose of this problem is to estimate how close the conducting wall must be moved in order to obtain stability against all external kinks. Consider the surface current model of an RFP illustrated in Fig. 11.56. Note that all currents flow only on the plasma surface.

(a) Write the equilibrium pressure balance relation across the plasma surface: $\left[\!\left[p + B^2/2\mu_0 \right]\!\right] = 0$.

(b) Evaluate δW_F, δW_S, and δW_V. Show that

$$\frac{\delta W}{2\pi R_0} = \frac{\pi B_\theta^2(a) \xi_a^2}{\mu_0} \left[(1 - \beta) \frac{kaI_a}{I_a'} - 1 - \frac{m^2 K_a}{kaK_a'} \Lambda \right]$$

where $\beta = 2\mu_0 p / B_\theta^2(a)$ and

$$\Lambda = \frac{1 - I_a K_b' / K_a I_b'}{I - I_a' K_b' / I_b' K_a'}$$

Also, $I_x \equiv I_m(kx)$, $K_x \equiv K_m(kx)$ are modified Bessel functions. The notation K_x', I_x' denotes differentiation with respect to the argument. When evaluating

δW_F treat $\mathbf{Q}$ rather than $\boldsymbol{\xi}$ as the quantity to vary. Check that the $\boldsymbol{\xi}$ that results from minimizing $\mathbf{Q}$ is well behaved.

(c) Show that the most unstable mode for $m = 0$ corresponds to $k \to 0$ and requires $\beta < 1/2$ for stability.

(d) Simplify Λ by assuming $kb \ll 1$. (This is only a marginally acceptable approximation, made for mathematical simplicity.)

(e) For $m = 1$ approximate

$$\frac{zI_1(z)}{I'_1(z)} \approx \frac{z^2}{c_1 + c_2 z}$$

$$-\frac{K_1(z)}{zK'_1(z)} \approx \frac{1}{b_1 + b_2 z}$$

Determine c_1, c_2, b_1, b_2 so that each function assumes the correct limiting values as $z \to 0$ and $z \to \infty$.

(f) Calculate the most unstable wave number and the corresponding farthest wall position that leads to stability against $m = 1$ external kinks for (1) $\beta = 0$ and (2) $\beta = 1/2$.

11.6 Show that δW for a general sharp-boundary screw pinch is given by

$$\frac{\delta W}{2\pi R_0} = \frac{\pi \xi_a^2}{\mu_0} \left[\left(B_0^2 + B_\theta^2 - 2\mu_0 p \right) \frac{kaI_a}{I'_a} - B_\theta^2 - \Lambda (kaB_0 + mB_\theta)^2 \frac{K_a}{kaK'_a} \right]$$

where B_0 is the external B_z field, $B_\theta = B_\theta(a)$ and Λ, K_a, I_a are defined in Problem 11.5.

11.7 Consider an arbitrary diffuse screw pinch. Prove that when $J_z(r)$ reverses sign at some value $r = r_0$, then Suydam's criterion is automatically satisfied for $r > r_0$ as long as B_θ itself does not reverse. Hint: Assume $rJ_z/B_\theta < 0$ for $r_0 < r < a$ and eliminate p' from Suydam's criterion using the equilibrium pressure balance relation.

11.8 Starting from the resistive MHD equations (i.e., $\mathbf{E} + \mathbf{v} \times \mathbf{B} = \eta \mathbf{J}$) derive a formula for dK/dt where the helicity K is given by

$$K = \int_V \mathbf{A} \cdot \mathbf{B} d\mathbf{r}$$

and the integration volume corresponds to the volume enclosed by a flux surface.

11.9 Estimate the growth rate for the $m = 1$, $n = 1$ internal kink mode in a low β large aspect ratio tokamak as follows. Start with the variational formulation of MHD given by
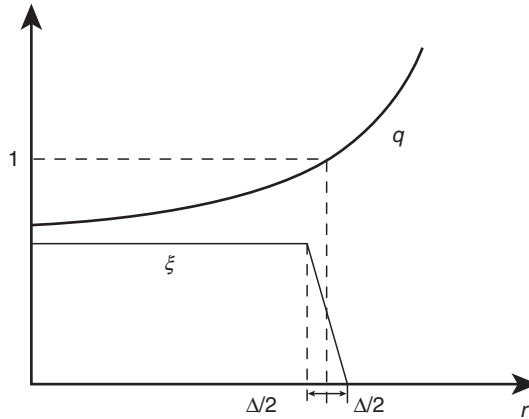
Figure 11.57 Diagram for Problem 11.9.

$$\omega^2 = \frac{\delta W}{K}$$

Use the ohmically heated tokamak expansion and write $\delta W = \delta W_2 + \delta W_4$. Substitute the trial function illustrated in Fig. 11.57 and treat Δ as a variational parameter. Note that for the $m = 1$, $n = 1$ mode, $\delta W_2 \to 0$ as $\Delta \to 0$. Assume Δ is ordered so that $\delta W_2 \sim \delta W_4$ as $\Delta \to 0$ and for simplicity treat $\rho(r) \approx \rho_0 = $ const out to the $q = 1$ surface. Show that for the minimizing Δ

$$\omega^2 \approx -\frac{3V_a^2}{R_0^2}\left[\frac{W_4^2}{r_s^2 q'^2(r_s)}\right]$$

where $V_a^2 = B_0^2/\mu_0\rho_0$, r_s is the radius of the $q = 1$ surface and

$$W_4 = -\frac{1}{r_s^2}\int_0^{r_s} r\,dr\left[r\beta' + \frac{r^2}{R_0^2}\left(1 - \frac{1}{q}\right)\left(3 + \frac{1}{q}\right)\right]$$

11.10 The Kruskal–Shafranov condition for an $m = 1$, $n = 1$ external kink instability in a low β large aspect ratio tokamak is given by

$$q_a \leq 1$$

This condition is independent of the current profile. Show here that the condition is also independent of the conducting wall position as long as the wall is not on the plasma.

11.11 (Due to R. R. Parker.) This problem examines the stability of a large aspect ratio, low β tokamak against external kink modes. Recall that in the uniform current density model, instability exists for values of q_a in the range

$m - 1 < nq_a < m$ for a given m, n mode with the wall at infinity. To simplify the analysis, attention is focused on the $m = 4$, $n = 1$ mode. The q profile is assumed to be

$$q(r) = \frac{4}{1 + 6J_1(\alpha r)/\alpha r}$$

where J_1 is a Bessel function and α is a parameter.

(a) Sketch the $q(r)$ and $J_\phi(r)$ profiles for several values of αa in the range $0 \leq \alpha a \leq \alpha_0 a$. Here, $\alpha_0 a$ is the value of α for which $J_\phi(a) = 0$. Calculate the value of $\alpha_0 a$ and the corresponding value of q_a.

(b) Find the perturbation which minimizes the plasma contribution to δW. Hint: Make the substitution $b = r^{3/2} \Delta \xi$ where $\Delta(r) = n/m - 1/q(r)$.

(c) Using the solution for ξ found in (b), substitute into δW. Note that the range of unstable q_a values can be written as $q_1 \leq q_a \leq 4$ where $q_1 = q(\alpha a)$. Sketch q_1 for $0 < \alpha a < \alpha_0 a$. Show that as $\alpha a \to \alpha_0 a$ (corresponding to zero current density at the plasma edge) the range of unstable wave numbers shrinks to zero for the $m = 4$, $n = 1$ mode.

11.12 This problem demonstrates the powerful stabilizing effect that arises for external kink modes when the vacuum region is replaced by an ideal force-free plasma. Consider external kink modes in a low β, large aspect ratio ohmically heated tokamak.

(a) Show that for the external kink mode, the general screw pinch δW reduces to

$$\frac{\delta W}{W_0} = \int_0^a r\,dr \left(\frac{n}{m} - \frac{1}{q}\right)^2 \left[r^2 \xi'^2 + (m^2 - 1)\xi^2\right] + BT$$

where $W_0 = 2\pi^2 B_0^2/\mu_0 R_0$,

$$BT = a^2 \xi_a^2 \left(\frac{n}{m} - \frac{1}{q_a}\right) \left[\frac{n}{m} + \frac{1}{q_0} + m\left(\frac{n}{m} - \frac{1}{q_0}\right)\Lambda\right]$$

and

$$\Lambda \approx \frac{1 + (a/b)^{2m}}{1 - (a/b)^{2m}}$$

For simplicity assume $m > 0$ and $nb/R \ll 1$ in the expansion of Λ.

(b) Assume now that the vacuum region is replaced by an ideal force-free plasma. In order for ξ to remain bounded, B_{1r}, must equal zero at the resonant surface in the exterior region, rather than at the location of the conducting wall; that is,

since $\xi = -iB_{1r}/F$, then $B_{1r}(r = r_s) = 0$ at the radius where $F(r_s) = 0$. This implies that the value of a/b appearing in Λ should correspond to a/r_s. Show that

$$\frac{a^2}{b^2} \rightarrow \frac{a^2}{r_s^2} = \frac{nq_a}{m}$$

(c) Using this relation show that the boundary term is always positive. All external kinks have been stabilized for arbitrary current profiles in the plasma.